FLOW CHARACTERIZATION ON A THIN FILM SPINNING APPARATUS

A THESIS
SUBMITTED TO THE FACULTY OF
UNIVERSITY OF MINNESOTA
BY

Alonso A. Alvarado

IN PARTIAL FULFILLMENT OF THE REQUIREMENTS
FOR THE DEGREE OF
MASTER OF SCIENCE

Ellen K. Longmire, Adviser

September, 2014

Acknowledgements

That a conclusion reached in one environment (say the laboratory) will apply in a different environment (say the full-scale process) is based not on statistical reasoning, but on what Deming called "a leap of faith". Good data and subject matter knowledge can narrow the chasm but not eliminate it. – Statistics for experimenters, 2005.

The work shown in this report reflects the help and support of many remarkable individuals, whom willfully gave me precious and sometimes courageous advice to approach this interesting problem. I am above all grateful to Dr. Ellen Longmire, her patience and thorough guidance showed me a path not known before. I will hopefully put in good use her methods toward my career.

I am beholden and thankful to the late Dr. Gustavo Nunez, without him I would not have followed with this research. His insightful advice, memorable stories and various teachings are cherished without a timestamp. I want to thank the collaboration and intangible support by the people at Nano Dispersions Technology, for always being cheerful and responsive to my various questions. Specially, the ever standing help of Dr. Maria Briceno, Suyin Torres and Jesus Palacios, that provided me with unfathomable support allowing me to continue with this research.

I had the privilege to share and learn from this colorful experience at the side of fantastic lab mates at the Turbulent Shear Flow Laboratory. I want to acknowledge the present and previous lab members who help me through the research process by sharing valuable knowledge and ideas: Dr. Deepak Adhikari, Dr. Zheng Zhong Sun, Ankur Bordoloi, Erik Haugen, Daniel Krizan, Yan Ming Tan, Kyle Winters and Shaokai Zheng.

Without the technical help of: Dr. Matthew Stegmeir (TSI, Inc.), Dr. Steve Anderson (LaVision, Inc.), Kale Hedstrom, Jason McConnell, Daniel McPeak, Mostafa Toloui and specially Dave Hultman, building my experimental rig would have been a daunting task.

Funding for this project was obtained through the support of Nano Dispersions Technology, Inc. and the IFARHU-SENACYT scholarship for professional excellence from Panama, Republic of Panama.

Dedication

To my family and many friends, for their love and support through the rough seas.

Abstract

In industrial milling operations that use comminution and wet-comminution techniques, the reduction of the particle size is usually achieved through crushing the sample with a material harder than the product. These methods are convenient when the required median particle size is above 400 μm. However, to obtain post-milling particle distributions with 85% sub-micron particles (in number) is both energy intensive, and time consuming. For conventional milling machines, to have the required output in several ton/hr of a product, having a large number of particles in the micron or sub-micron sizes at an affordable rate is cumbersome.

Here, a wet-comminution machine that has shown to achieve the aforementioned milestones in the laboratory scale is studied. However, when the machine is scaled to industrial processes, it was recorded that some of the product variables are difficult to scale. In these studies, we attempt to understand the mechanisms by which this machine operates in order to achieve successful scaling.

The apparatus operates completely on fluid mechanics principles, it consists of two concentric cylinders, the inner cylinder that has a smaller radius than the outer, rotates while the larger is held stationary. The inner cylinder is also shorter in length than outer, hollow in the inside and has transversal holes where the shaft attaches to the apparatus. The apparatus can operate in batch condition, where the liquid volume is much less than the volume of the apparatus, typically $0.3V_T$, $0.42V_T$ and $0.54V_T$. In addition, the apparatus can operate with throughflow, which the upper plate covering the apparatus is reduced in radius.

Two component Laser Doppler Velocimetry (LDV) was used to obtain even-time averaged statistics of the azimuthal and axial velocities, in the gap and underneath the impeller. Also, Flow Visualization using Kalliroscopic particles was performed as means of observing large scale structures in the gap. Moreover, single plane Particle Image Velocimetry (PIV) was used to acquire statistics of the axial and radial velocities in the gap, and both underneath as well as above the inner cylinder.

It was found that at both throughflow conditions, the topology of the apparatus creates a free spinning boundary both at the bottom and above the inner cylinder. Near the bottom, the thickness of the boundary was found to decrease with Reynolds number to a limiting value, where Re_θ is based on gap thickness and inner cylinder tip speed. For Re > 2546, the liquid/air interface thickness is constant for a given holding volume. In the regions above and underneath the inner cylinder, corner vortices were detected; if viewing the left-hand-side, the lower one rotating counter clockwise, while the upper rotates clockwise. The thickness of these vortices was found to be constant for various axial flows at Re_θ = 1110 and 2230. The radial length scale of the stationary vortices was found to be ~2.5δ.

The flow generated inside of the gap was characterized to have Taylor vortex signatures. It was found that the length scale of the Taylor vortices in the gap is rather insensitive to Reynolds number or holding volume ratio. The average vortex pair wavelength λ was found to be 3.6δ. Average flow statistics in batch condition indicate that in the gap, at Re_θ= 1110 and 2230, the azimuthal velocity is $0.5U_\theta$ over much of the length. Similarly, it was found that the net axial flow through the gap is close to zero.

Table of Contents

List of Tables

List of Figures

Nomenclature

Used as reference to the units in nomenclature

Symbols for SI base units	Dimension
L	Length
m	Mass
t	Time

Roman Symbols	Description	Units (SI)
d	Diameter of transversal holes or inlet port.	L
F	Frame rate.	-
f_s	Thickness of the upper plate thickness.	L
f_L	Focal length of optical lens.	L
$f_{Ta\ vortex}$	Frequency of Taylor vortices	1/s
g	Gravitational force.	L/t^2
H	Length of impeller or inner cylinder.	L
h_L	Gap-space between the bottom surface of the outer cylinder to the lowest (bottom) side of the inner cylinder (impeller).	L
h_T	Gap-space between the upper plate to the impeller.	L
$\varkappa$	LDV beam angle.	-
L_T	Length of outer cylinder.	L
M_o	Magnification in the camera	pixel/L
M	Molarity (mol-solute/volume of solvent).	n/L^3
N	Approximate statistical number of particles, media contacts or instances that occur or are used in a closed system for wet-comminution.	-
N_{cell}	Number of Taylor vortex pairs in the column of liquid with thickness δ.	
N_{frames}	Number of frames used for averaging the vortex translation distance in single plane PIV.	-
n	Rotation rate of machinery.	rad/t

$Ne=\frac{P}{n^3 d^5 \varrho}$	Newton number.	-
$\mathbf{P}$	Mechanical power delivered to the fluid by the mixing motor.	mL^2s^{-3}
P_s	Probability of particles stressed over the required breakup threshold.	-
$\dot{m}$	Mass flow rate.	m/t
$\dot{Q}$	Volumetric flow rate.	L^3/t
$\mathbf{q}=\frac{\pi d_p}{\lambda}$	Normalized diameter, Lorenz-Mie scattering regime.	L/L
$Re_d=\frac{\varrho U_\theta d}{\mu}$	Reynolds number based on cylinder diameter for agitation theory.	-
$Re_\theta=\frac{\omega r_i \delta}{\nu}$	Rotational Reynolds number.	-
r_i	Inner cylinder (impeller) radius.	L
r_o	Outer cylinder radius.	L
$SI_{GM}=d_{GM}^3 \varrho_{GM} U_\theta^2$	Stress intensity for comminution based on grinding media.	$mL^2 2t^{-2}$
$t_g=\frac{\bar{H}}{W_g}$	Mean residence time in the gap.	t
$t_r=\frac{V_A}{\dot{Q}}$	Nominal residence time on the spinning film apparatus.	t
Ta_{cr}	Critical Taylor number above which Taylor type structures vortices appear.	-
$Ta=\frac{2\eta^2}{1-\eta^2}\frac{\omega^2\delta^4}{\nu^4}$	Taylor number	-
U_θ	Velocity in the azimuthal plane of reference.	L/t
$U_\theta^*=\frac{U_\theta^{mean}}{U_\theta}$	Normalized azimuthal velocity.	-
U_θ^i	Measured instantaneous azimuthal velocity by LDV.	L/t
$U_\theta^{mean}=\frac{1}{n}\sum_{i=1}^{n} U_\theta^i$	Arithmetic mean of the instantaneous measurements of the azimuthal velocity at a single position.	L/t
W	Measured axial velocity by PIV.	L/t
W_g	Mean axial velocity in the gap.	L/t

W_i	Interrogation window size – PIV.	L
$W_i^* = \frac{W_i^{mean}}{U_\theta}$	Mean normalized axial velocity.	-
W_i^{gap}	Measured instantaneous axial velocity by LDV.	L/t
$W_i^{mean} = \frac{1}{n}\sum_{i=1}^{n} W_i^{gap}$	Arithmetic mean of the instantaneous measurements of the axial velocity at a single position.	L/t
W_V	Measured axial velocity of Taylor vortex rings by flow visualization.	L/t
V_A	Calculated volume of annulus or cylinder.	L^3
V_L	Volume of fluid within SFA during experiments.	L^3
$V_T = \pi L_T r_o^2$	Total vessel volume.	L^3

Greek symbols	Description	Units (SI)
$\Gamma = \frac{L}{\delta}$	Geometrical aspect ratio for the spinning film apparatus.	-
Δt	Time interval between two laser pulses.	t
δ	Thickness of the gap between the inner and outer cylinders. Formally defined as r_i-r_o.	L
λ	Average wavelength of two counter rotating Taylor vortices directly measured from flow visualization.	L
λ_{Bottom}	Thickness of the development zone before Taylor vortices are observed at the bottom of the impeller.	L
$\lambda_E = \lambda_{Bottom} + \lambda_{Top}$	Total thickness of the development zones within the SFA at a specific condition.	L
$\lambda_{fi} = \frac{H}{N\delta}$	Average wavelength of two counter rotating Taylor vortices based on finite column approximation.	L
λ_{Top}	Thickness of the development zone in the upper edge of the impeller.	L
μ	Dynamic viscosity.	$mL^{-1}s^{-1}$
$\xi = \frac{f_s}{\delta}$	scale-up ratio.	-
$\eta = \frac{r_i}{r_o}$	Geometrical radius ratio.	-
ν	Kinematic viscosity.	L^2/t
ρ	Density.	m/L^3

$\sigma_{\Delta r}$	Uncertainty in the displacement of particles, r direction	L
$\tau_P = \frac{\varrho_P d_P^2}{18 \nu_f \varrho_f}$	Particle inertial time response constant.	t
ω	Rotation rate of the inner cylinder.	rad/t

Subscripts	Description
c	Contacts instances between grinding media in wet-comminution.
f	For values based on the film thickness.
i	Inner cylinder (impeller).
Ip	Inlet port.
o	Outer cylinder.
P	Referent to particles in suspension or grinding media.

Chapter 1.

Introduction

1.1 Motivation

The reduction in particle size of powder-like materials is a necessity in secondary sectors of any macro-economy. Milling of particulates is ubiquitous in mining operations, chemical and other engineering industries. The rate of volume of materials processed, and their final particle size distribution diverges between each application, and within a specific industry. However, the mining and chemical sectors are recognized to be hungry for larger volumes of processed materials. In one example 39% of the world electric power generated in coal fired boilers uses the pulverized form of this mineral (Hook, Kjell 2009).

The action of pulverizing coal and other minerals for commercial use in large quantities is accompanied by numerous tradeoffs. For instance, the energy expenditure per volume of processed material relative to the product particle size is a limiting constraint in these operations. Moreover, in processes where the mean particle size is below the airborne threshold for the material, environmental considerations become necessary. There are other operational perils that come into sight as a consequence from fine dusts; since airborne particles that are <75 μm in size are considered an occupational hazard (Calvert 1990). In milling operations where energy requirements, machinery wear and other process variables limit the throughput of certain apparatuses, a technique to circumvent these limitations is found using a wet-comminution apparatus. The comminution particles in suspensions are ground into the sub-micron scale by what is thought to be particle-particle interactions.

The apparatus used to obtain the data shown in this manuscript is hereby defined as a Spinning Film Apparatus (SFA), and it has operational similarities to the canonical Taylor Couette Flow (TCF) experiment. Similar to TCF, the SFA consists of two concentric cylinders, where the inner one rotates. Yet, various geometrical differences arise between both set-ups and thus, they are discussed in the following sections.

Field tests of the industrial SFA design show that scaling from bench-top to industrial production is non-linear. Moreover, the energy consumption per unit mass of processed material is lower than other wet-comminution devices. However, elemental insight on fluid flow characteristics is nonexistent for this device; therein the strong interest to shed light on the governing dynamics behind the operation.

1.1.1 Current challenges in milling operations

For industrial pulverizers commonly used to reduce mineral beads or ore into finer particles, the energy consumption per unit mass of material is a milestone hard to overcome. For example, in ball milling operations, hard spherical (steel) balls tumble inside a rotating drum crushing ore or mineral beads, the transmission of grinding energy from the steel balls to the particles is limited by input material size, its load on the apparatus and hardness. For the case of wet slurries, the particle concentration plays an unavoidable role in the dispersion viscosity.

Pulverizers and other milling equipment operations account for up to 50% of the total mineral pulverizing costs. Moreover, the cost in kWh/ton of operation to achieve a mean particle size <75 μm for ball mills, varies with the loading volume of the drum. Hence, to achieve large throughputs in a ball-mill system with particle sizes on average less than 75 μm, the optimal volume of the mill is around 30% filling as seen in Figure 1.1 (Clermont, De Hass et al. 2008).

Other milling devices and configurations in the comminution and pulverizing sectors may have different power consumption trends in their curve depending on loading, final particle size and type of operation. Moreover, the milling effect depends on the product

type and throughput rate. Example articles with energy consumption information include (Weit 1987, Cleary 1998).

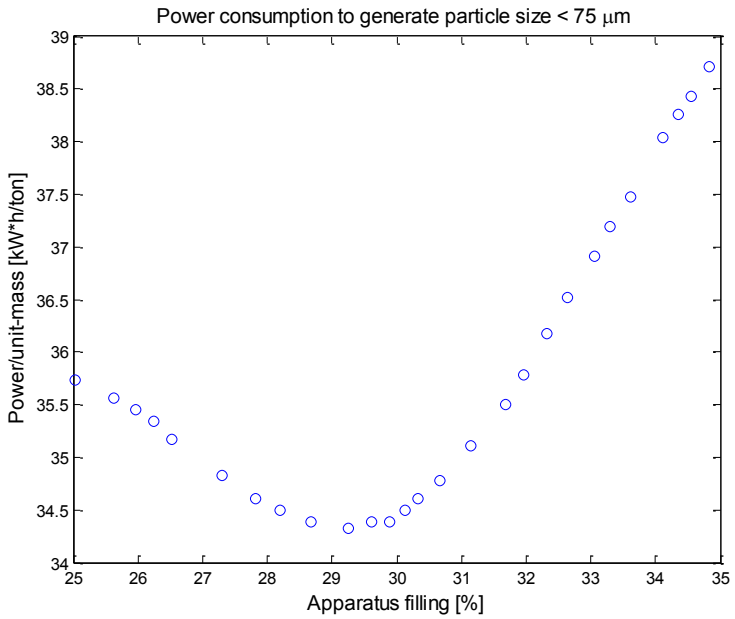

Figure 1.1. Power consumption for a 4.5 m diameter ball mill apparatus (Clermont, De Hass et al. 2008)

In addition to significant energy costs related to the actual pulverization and milling of powders, additional expenses are due to wear on the apparatus as a result from the transfer of stresses through the operation. In time these operational costs are non-negligible due to repairs and associated issues as a result of the nature of the process.

1.1.2 Unit operation scaling

Beyond challenges in the operation and efficiency of current milling machines there is the issue of scale-up from bench top experiments into industrial scale. Many constraints arise when production is moved from *g/s* into *ton/h*. To address the basic needs for scaling, a handful of scaling factors are currently used to generate ballpark approximations in terms of energy requirements and flow characteristics.

For scaling of mixing processes, studies show the specific energy input to the material to be the most comprehensive parameter with regard to comminution results. This input is

based on empirical models deriving from a disk or cylindrical stirrer in a liquid filled flask (Schlichting and Gersten, 2000).

The agitation theory is based on the act of carrying mechanical power to the liquid by the cylinder or disk surface. The energy transferred and thus the power consumed by the liquid (without suspended particles) can be calculated using shear stress methods derived from boundary layer theory in Schlichting and Gersten, 2000. In short, agitation theory seeks to match the shear leaving a mixer blade at various length scales.

Commonly the Newton number and the Reynolds number are used to characterize stirred disk/cylinder systems. The Newton number is analogous to the drag coefficient and therefore it can be a function of the input Reynolds number. The basic forms of these dimensionless numbers are:

$$\text{Reynolds number} \quad Re_d = \frac{\rho U_\theta d}{\mu}$$

$$\text{Newton number} \quad Ne = \frac{P}{n^3 d^5 \rho}$$

For Reynolds number, ρ is density of the fluid, U_θ cylinder tip speed, d cylinder diameter and μ the dynamic viscosity of the fluid. In the Newton number, P is the power input to the fluid and n the rotation rate of the cylinder in revolutions per second.

The Newton number also known in industry as the Power number parameter can be used as a basic criterion for scale-up of mixing processes (Clermont, De Hass et al. 2008, Weit 1987). Previously we mentioned that agitation theory derives from empirical models, implying the need for corrections for flow regimes and types of fluids.

In regards to industrial mixing in general, the operation is performed with various types of mixers, for example ribbon mixers, boat-like propellers, etc. For these types of mixers, to relate the energy input to the fluid by shear-scaling is common practice. Additional empirical correlations are used for various types of mixers as means to relate spinning disk theory.

By contrast, in wet-comminution theory, where the relative viscosity changes as the particle size distribution of the dispersion is altered, the power number approach is used to account for the number of particles that are in contact with each other inducing the comminution event; instead of using the method in the estimation of energy consumed by the material. In that matter, the basic approach for scaling comminution processes is to consider the number of stress-events that occur for each product particle.

A product particle is defined as the material that is milled and reduced in particle size. The approach consists of probability estimations regarding the number of particles in the system. To estimate the number of possible stresses, one can estimate the probability of a particle stressed over breakup threshold P_s, the number of particles in the system N_P, and the number of media contacts within the apparatus N_C. A media contact is thought to be a point where the product-particle interaction with other particles or milling media causes breakup of product particles (Kwade 1999).

$$\text{Number of contact stresses} = \frac{N_C P_S}{N_P}$$

The estimation of the number of contact stresses is adapted to various types of comminution devices. These values are then used to estimate the energy adsorbed by the process in order to break up particles. Scaling is then achieved by accounting for both geometrical aspects of the machinery and the estimated energy delivered to the particles.

In the case of stirred media mills and similar machinery, the stress intensity (SI_{GM}) of these events as well as material holding volume is of direct influence in the subsequent particle size distribution. According to Bunge, Pietzsch et al. 1992, the stress intensity in media mills is the quotient of the torque of the apparatus and the product mass within the mill. A more physical consideration of the mechanism for the comminution process in media mills is thought to occur due to high velocity gradients within the stationary wall and the stirrer. Based on this knowledge the term SI_{GM} refers to the energy applied to a particle of grinding media or product during the comminution process (Blecher, Kwade et al. 1996), and is defined in the following way:

$$SI_{GM}=d_{GM}^3 \varrho_{GM} U_0^2$$

Where d_{GM} corresponds to the diameter of a grinding media particle, ρ_{GM} is the density of a grinding media particle and U_θ is the azimuthal (tangential) speed of the stirrer shaft. Ideally, the stress intensity is constant during comminution, since grinding media size, density, as well as impeller speed and particle concentration are held constant during the process (Jankovic 2001). However, for the process of wet comminution used in the SFA, where the grinding media is also the product particle which is changing in size distribution throughout the length of the value of SI_{GM} is not constant.

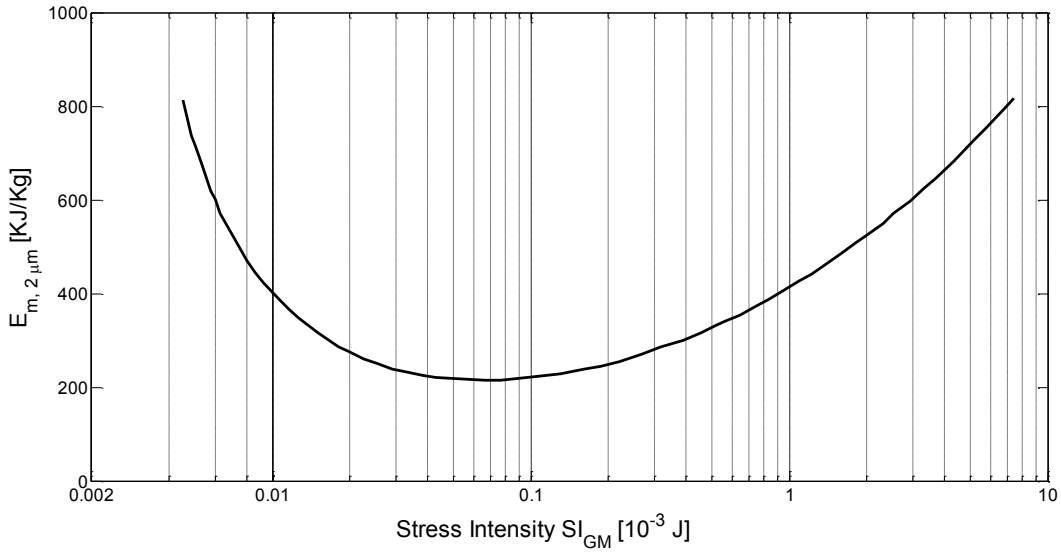

Figure 1.2. Influence of stress intensity on the specific energy required to reduce particle size to a final median particle size of 2µm. Data extracted from (Kwade 1999).

For each milling material there is a specific relationship between the stress number (number of events where a particle is subjected to contact with the grinding media) and the stress-intensity as well as the final particle size desired. The relationship is expanded in Kwade, who suggests that certain stress-intensities at specific particle sizes can be achieved by varying the stress number. To illustrate this concept an extracted data set from Kwade is shown in Figure 1.2, where the trend is akin to descriptions in (Bunge, Pietzsch et al. 1992) for comminution of limestone.

From Figure 1.2, we observe the existence of a local minimum for the specific energy required for comminution of limestone. This trend is similar for other crystalline materials, in which the stress intensity parameter is used to account for the required energy to obtain certain particle sizes in the product material. Therefore, to achieve proper scaling in these types of systems, careful consideration is needed to keep the stress-intensity constant at various process scales. Various examples of the energy requirements to obtain specific particle sizes according to stress intensity are seen in (Jankovic 2001, Kwade 1999, Kwade 2002, Becker 1999).

1.2 Previous work

1.2.1 Wet comminution machines

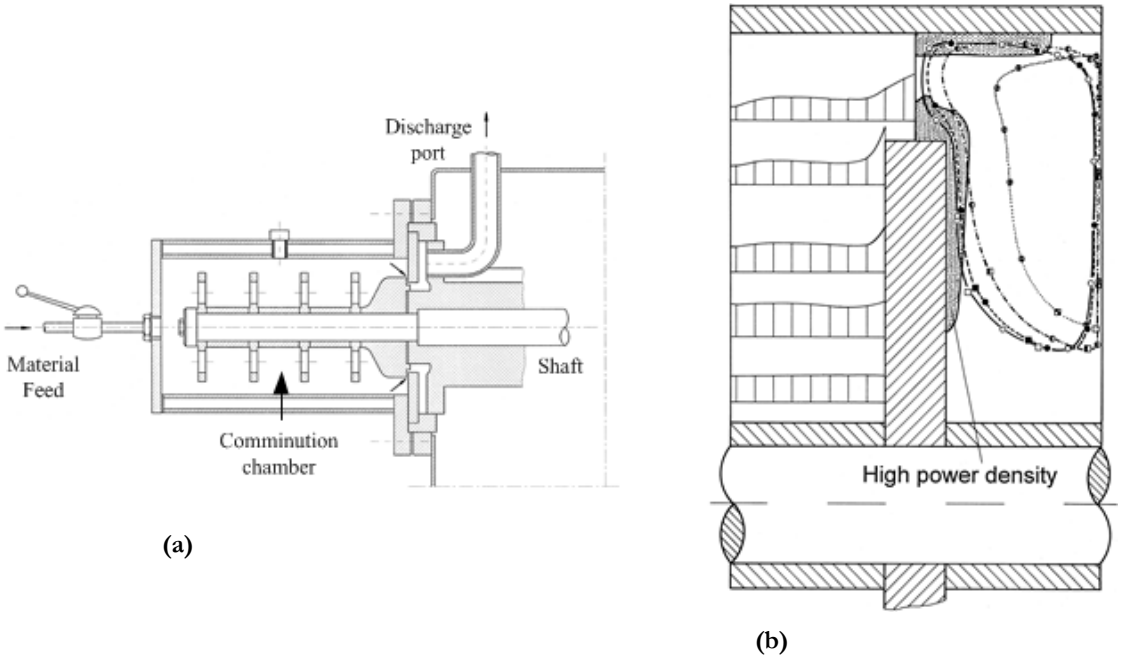

Figure 1.3. (a) Cross section of stirred media mill (Becker 1999) (b) Numerical simulation of the flow field left within a stirred media mill. Left side: tangential velocity on, right side: power density (Blecher, Kwade et al. 1996)

In Figure 1.3b the azimuthal velocity profile within the comminution chamber is shown at the left of the drawing. Blecher et al. 1996, used the velocity field results to compute

the power density distribution seen at the right side of Figure 1.3b. They calculated that the ratio of the input power to the system to the local mean specific power corresponds to predicting comminution results; they call this ratio the power density. The shaded regions in Figure 1.3 correspond to the locations where the power density is greater than one.

A variety of comminution machines are used to mill minerals and organic pellets in wet conditions and use loose grinding media to break dispersed particles. The complete mechanisms for breakup in these machines are not yet understood, although generalizations of energy transfer are made as previously described.

Nevertheless, simulations of laminar flow using Newtonian fluids show that steep gradients in velocity occur close to the grinding chamber walls as seen in Figure 1.3b. It is theorized these gradients are responsible to induce breakup by transferring mechanical energy within particles (Becker 1999, Kwade 1999).

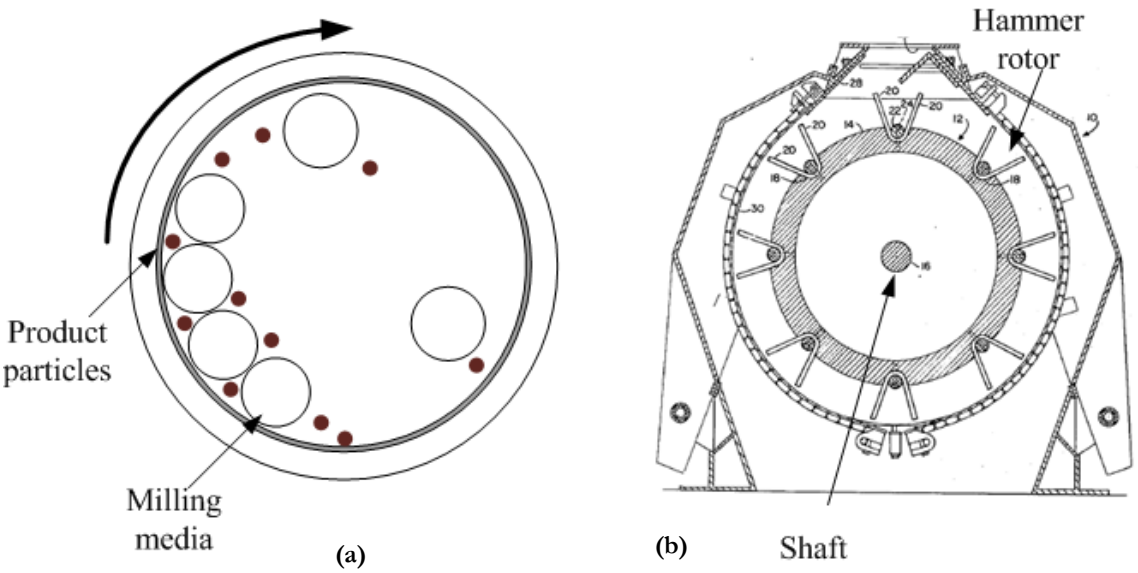

Figure 1.4. a) Ball mill cross section sketch. b) Hammer mill cross sectional view (Vargo 1982).

Ball mills, roller mills and hammer mills function with similar principles, in which a grinding media is placed with the product material in a hollow cylinder with added baffles

to generate gradients in velocity within the apparatus. The principle within a ball mill is to spin at various rotational speeds while both the grinding media and product start to cascade inside the mill. The cascading action within the mill drives the stress events that break up particles.

1.2.2 Current industrial apparatus and operation

From previous descriptions we now know that scaling comminution processes are empirical and poorly understood. The SFA was developed with the mindset of solving scale up issues in the milling and mixing industries. As an example, one goal is to obtain large throughputs of treated material without increasing the footprint of the apparatus. Moreover, for milling purposes one objective is to replicate the conditions that allow for manufacturing high quality products in the laboratory and scale those parameters seamlessly. This apparatus is thought to reduce such scale-up problems by using specific geometrical and dynamical parameters along multiple length scales.

The basic description of the SFA consists of two concentric cylinders in which the inner one rotates about the axial center. The inner cylinder is smaller in length than the outer and hollow inside up to the connection to the shaft. At the location were the cylinder is attached to the shaft, a connecting plate is perforated with several transversal holes. The upper part of the apparatus is closed with a fixed non-rotating plate. The plate extends inward over a distance f_s and is not in contact with the shaft.

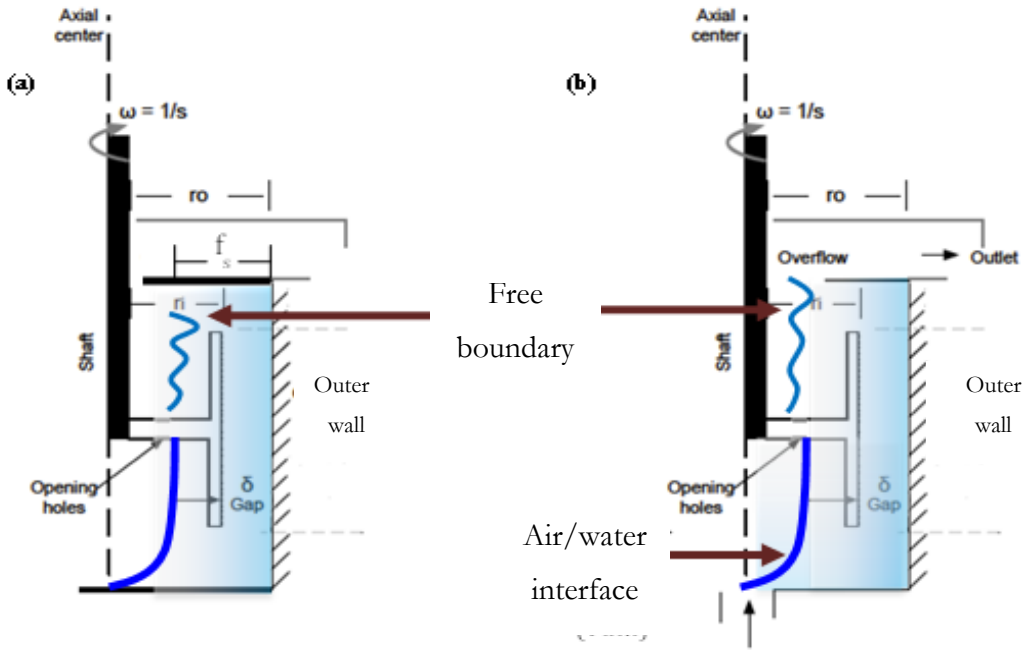

Figure 1.5. Sketches of the SFA and the free boundary at both (a) batch and (b) continuous conditions. The fading shade of blue that extends from the outer wall to the opening hole represents the fluid filling that area.

The apparatus geometry encounters minor modification when switched into a through flow condition as seen in Figure 1.5. The inlet port is located at the bottom axial center and the upper fixed plate is replaced with an annular plate that varies in width (f_s).

One of the main areas of use for the SFA is in milling processes. In these types of applications the material is mixed as slurry before being processed. The comminution process heats the slurry through the repetitive contact between the milling mechanism and the solid substrate. In many applications temperature changes of a few degrees Celsius are unfavorable. The SFA does not avoid classic mechanics and therefore its normal operation also generates heat, therefore the apparatus has a cooling jacket that removes excess thermal energy.

Through results obtained from industrial partners milling bituminous coal, calcium carbonate and petroleum coke, it was found that gap thickness upper plate width,

rotational speed and volumetric flow rate are the most important independent variables for an otherwise fixed SFA geometry.

At steady state operation, either in batch or continuous mode the dynamic balance between inertial and gravitational forces pushes the liquid-solid material to the wall of the outer cylinder. A liquid/air interface results which is termed the *spinning film*. The thickness of the film can be varied according to the initial volume fraction in the vessel, by changing the thickness of the upper plate. The inner cylinder with radius r_i rotates about the z-axis until the desired rotational speed is reached. The actual thickness of the film varies with z location. This film extends from the bottom of the apparatus to the joint of impeller/shaft as seen in Figure 1.5a. At this position, the film is discontinued. Later, above the joint the film is re-constituted reaching the top of the SFA where the upper plate is located (in batch). In continuous flow mode the film extends above the upper plate and reaches the section where the overflow port is placed.

The SFA was designed to match the film thickness in batch and continuous mode. In the through flow case, the film thickness is hypothesized to match the width of the upper plate f_s, which equates to the thickness in the batch condition at a specific volume fraction. By doing so, it is thought that the apparatus matches various dynamic conditions in both cases, therefore it is thought that transitioning between operating conditions is effortless.

1.2.2.1 Industrial background on continuous operation

Historically, to correlate operating conditions, the spinning film apparatus was treated as a stirred tank reactor, implying that specific conditions could be matched in terms of overall performance variables, those being nominal residence time, processing volumes, and other outcome variables that are analogous to reaction rates.

Through the variation of the nominal residence time, upper plate width, and other process variables, industrialists determined the most favorable processing operating conditions. Table 1.1 shows the settings that historically provide products with the highest quality such that the particle size distributions are shifted toward smaller sizes.

Table 1.1. Experimental results for power consumption of the spinning film apparatus.

r_o [mm]	$P/\dot{m}\ \left[\frac{\text{KWh}}{\text{ton}}\right]$	Re_θ
80	26.9	15900
156	4.8	8491
252	1.1	5258

The rotational Reynolds number (Re_θ) is defined in the following way:

$$Re_\theta = \frac{\omega r_i \delta}{\nu}$$

Where ω is the rotational speed of the impeller (inner cylinder) in units of $\frac{\text{rad}}{\text{s}}$, r_i is the radius of the impeller and δ the gap thickness; ν is the kinematic viscosity of the fluid.

The operating conditions chosen for study were based on the data obtained in Figure 1.6 which depicts size distributions at two Re_θ and two mass flow rates. For larger Re_θ and $\dot{m}$ the results originate from an industrial SFA with the same dimensions as our experimental set-up. In the figure the data resulting from varying both the flow rate and rotational speed are slightly intuitive. The results show an increment in the population of

particles bellow 2 µm proportional to lower flow rates, implying a high nominal residence time in the apparatus.

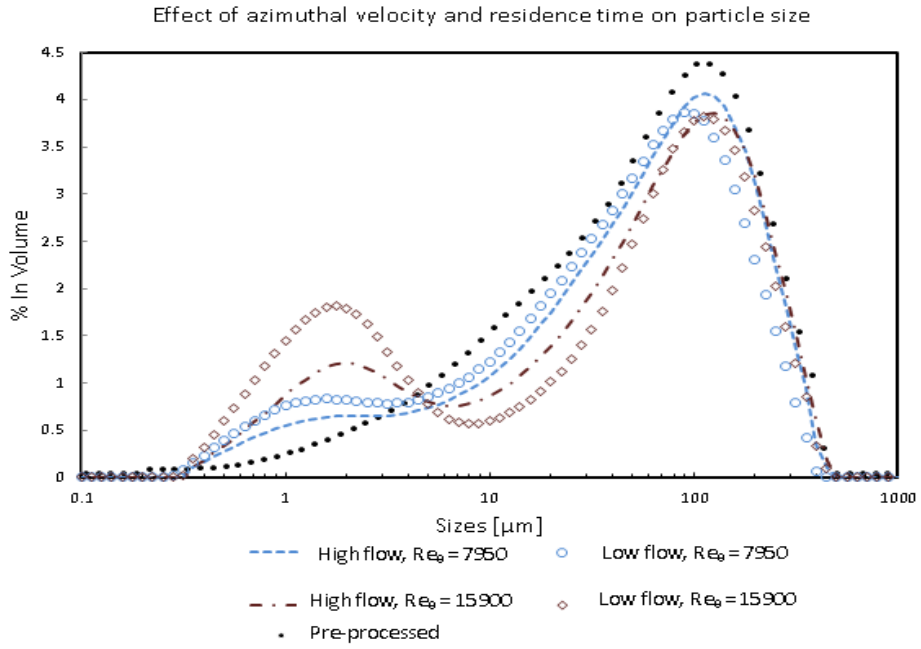

Figure 1.6. Comparative plot on various process conditions resulting in particle comminution of petroleum-coke. Here a laboratory scale SFA was used with equal geometrical proportions to the apparatus used for experiments in this manuscript. The volumetric flow rates shown at low flow and high flow condition are 0.62 L/min and 1.8 L/min respectively.

In traditional milling processes an increase in delivered power results in smaller particle sizes (Mende, F et al. 2004, Weit 1987, Bunge, Pietzsch et al. 1992, Kwade 1999, Blecher, Kwade et al. 1996). It is not yet known to the extent that the SFA follows classic comminution theory. Yet, in Figure 1.6 it is observed that at high Reynolds number (therefore increased gradients within the gap) the comminution step is more effective. However, while using the SFA for milling purposes, we find that power consumption per-unit mass does not increases with mass flow rate, as shown in Figure 1.7.

In Figure 1.7 the experimental points are obtained from milling a slurry of 60% $\frac{w}{w}$ pet-coke using the SFA. The upper plate width is scaled linearly with the outer radius, as well as the nominal residence time which was kept constant for all industrial tests.

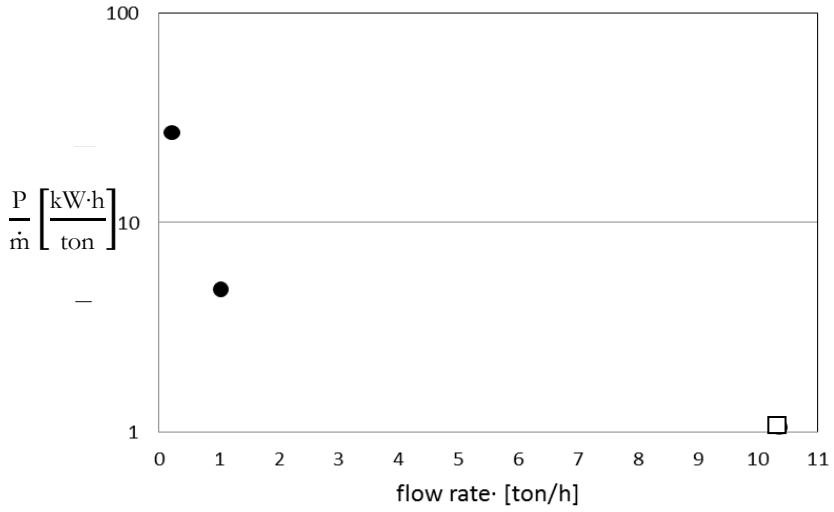

Figure 1.7. Experimental results on power consumption per mass of processed material for the SFA. Filled markers are experimental data entries, the hollow square marker is a theoretical data source; this value is estimated from subtracting the known drivetrain cost to an estimated milling energy cost.

The mean final particle size distribution is similar to Figure 1.6 with small flow and high Reynolds number. The power consumption of the milling operation was obtained by subtracting the power input by the dry drivetrain to the Amperage consumed by the motor while milling.

Figure 1.7 opens the idea that in the spinning film, high through flow can be achieved at low operating costs. The largest power used for milling is seen in a 0.3 $\frac{ton}{hr}$ apparatus of the size of the bench experimental set-up. Then, as the holdup volume increases so do the available through flow, but in the case of the SFA the used energy per volume is shown to decrease rapidly as shown in Figure 1.7. Properly, the argument that scaling is non-linear is seen in the aforementioned plot. This is observed specifically on the divergence between bench-results to industrial scales, as they differ largely in energy consumed per unit volume.

These results are somehow counter intuitive due to preconceptions about conventional ball-mill and other comminution machines. In such operations the power intake of the

system generally increases with flow rate and overall size, but in the SFA the truth is the opposite; where larger production lowers operational cost.

The results in the plot are attributed to scaling similarity from the upper plate width. By which the milling energy per unit volume is thought to be matched in all system scales. Therefore, the energy needed to mill materials is focused mostly to the particle break up mechanism itself rather than driving the machine bearings. This is therefore the logic for the immense interest to understand the location and behavior of such film in the system.

The parameters that separate the SFA from conventional Taylor Couette experiments are based on its geometry and dynamics. These parameters are observed in Table 1.2, which encompasses the foremost variables that affect the flow regime on the SFA. To be specific, it is thought that the thickness of the upper plate defines the thickness of the film in continuous mode, and the nominal residence time controls the overall comminution period that particles undergo on the apparatus.

Table 1.2. Dynamic and geometric variables expected to have either positive or negative impact on wet-comminution results using the SFA at a constant particle concentration.

Geometric parameters		Dynamic parameters	
Name	Symbol	Name	Symbol
Gap thickness	δ	Gap residence time	t_g
Upper plate thickness	f_s	Nominal residence time	t_r
Space between impeller and bottom of SFA	h_L	Azimuthal velocity	U_θ
Scape between impeller ant upper plate of SFA	h_T	Holding volume	V_T
Transversal holes	d	Axial velocity through the gap.	W_g

On the dynamic aspects, although Re_θ can be matched with the canonical experiments; there is limited documentation on the impact of an imposed axial flow on the characteristic modes (WVF & Turbulent Taylor vortices) of the main flow. However, as it is described in section 1.2.5 the transition between regimes is delayed when there is axial flow; it is therefore expected to occur on the SFA.

In section 1.2.2 it was described that the SFA by design seeks to recreate the spinning film in the continuous flow mode. To achieve this, the SFA needs to match the main film characteristics in the batch condition. To do so, the upper plate (f_s) was introduced as means for achieving that goal. Since at steady operating conditions, the tangential speed pushes the flow upward; the only physical wall to prevent the fluid from overflowing the restricted boundary applied by the upper plate. Therefore forcing the flow to have a certain radial thickness (presumably) that is of similar order as the upper plate thickness. Due to this uncertainty, it is important to give the underlying background on the relationship between the batch condition and continuous flow using the upper plate thickness as a scaling parameter.

To understand the principal parameters that affect the comminution efficiency of the SFA, industrial tests were performed in devices similar to apparatus described in this manuscript. For these tests normalized at a constant initial volume fraction of comminution particles in the inlet fluid, the parameters in Table 1.2 had the largest impact on the ratio of mean particle size below 2 μm in the comminuted material, to mean particle size in the pre-mixed fluid. Moreover, the basic dynamics of the system have not been characterized beyond conjectures that the flow field is akin to Taylor Couette Flow. For example, visualization of the free boundary in an apparatus similar to the SFA or a more canonical example is non-existent in literature.

Table 1.3. Operational ranges for optimum wet-comminution results on industrial tests.

Optimal parameters
$20\ s > t_r \geq 1\ s$
$U_\theta \geq 40 \frac{m}{s}$
$0.3 \leq V_T \leq 0.7$
$0.92 \leq \eta \leq 0.975$
$18.3 \leq \Gamma \leq 55$

The values shown in Table 1.3 are remarkably useful when used as the path to improve wet-comminution using the SFA. As explained before, these variables are (from top to

bottom) nominal residence time, azimuthal velocity and holding volume (of the film). The remaining two are derived variables such as radius ratio and aspect ratio. Interestingly, if all conditions are held constant, increasing nominal residence time does not have a significant impact on the final particle size distribution. These observations suggest that asymptotic behavior on the comminution efficiency within SFA is expected. Furthermore, it implies that the necessary number of larger particles necessary to crush smaller ones and themselves is reduced beyond the minimum concentration required for comminution to take place.

Moreover, one of the most relevant independent variables shown in Table 1.2-$\boldsymbol{f_s}$ was purposely left out of Table 1.3, since the effect of upper plate f_s and δ is not yet understood. However, a possible range of f_s could be inferred from V_T if one assumes that the film thickness equals f_s.

The nominal residence time t_r is based on this assumption, this assumes all liquid travels at a uniform axial velocity over the width of f_s. But, does it means an infinitesimal unit of slurry is truly comminuted for a period $\mathbf{t_r}$? A generalist type of answer could be "no", since it is unlikely that the above assumption holds. If instead, we assume that all fluid passes through the narrow gap, then, an alternative residence time to characterize milling is $\mathbf{t_g}$, writes as equation:

$$t_g = \frac{H}{W_g} = \frac{H\pi(r_o^2 - r_i^2)}{\dot{Q}}$$

Understanding the relevance of this temporal variable and the outcome of the interaction with f_s and Re_θ could lighten the path to comprehend the basic operation of the SFA. Moreover, as seen in Figure 1.5, the inner cylinder has eight perforations that span across the joint with the axis. The cross sectional area of these holes is larger than the cross section of the gap and the effect they have on the flow pattern both in batch and in continuous cases is unknown. To this point, there is not knowledge whether the flow pattern is truly affected by such holes, or whether fluid is going through them.

1.2.3 Taylor Couette Flow

The Taylor Couette flow is one of the most characterized and studied stability problems in fluid mechanics beginning with Couette 1890, Mallock 1888 & 1896. Further experiments conducted by Taylor in his groundbreaking paper showed that for two infinitely long concentric cylinders, there exists a cut-off rotational speed above which instabilities arise (Taylor 1923). For the case with outer cylinder stationary the speed of rotation for the inner cylinder at which this phenomenon occurs is known to be associated with a critical Taylor number (*Ta_c*). The critical number for $\frac{r_i}{r_o} \to 1$ was solved theoretically by Taylor, 1923 to yield a Ta_{cr}=1695.

The solution of the axisymmetric problem of Couette flow with finite length and outer cylinder stationary was initially solved P.H Roberts in the appendix section of (Donnelly, Schwarz 1965), the derivation of Ta_C originates from the aforementioned work by Taylor. The variable *Ta* corresponds to a modified Taylor number used to derive the critical value.

$$Ta = \frac{2\eta^2}{1-\eta^2}\frac{\omega^2\delta^4}{\nu^4}$$

In the equation, ω is the angular velocity of the inner cylinder and η is the radius ratio of the inner to outer cylinder, ν is the kinematic viscosity of the fluid and δ is gap width. The approximation of the critical Taylor number is reached for the smallest value of *Ta* for a given *axial wave number* and *growth rate of the instabilities*. The solution of the system of equations for η=0.95 (similar to the SFA in this manuscript) was solved by P.H Roberts and experimentally measured by Donnelly and Schwarz, 1965. Therein, the critical Taylor number value used within this manuscript is **Ta_{cr} = 1755**.

The nature of the Taylor Couette Flow instability is known to be highly dependent on the initial conditions of the system, other factors such as geometrical parameters like the radius-ratio $\left(\eta = \frac{r_i}{r_o}\right)$, aspect ratio $\left(\Gamma = \frac{L}{\delta}\right)$ and cylinder end-construction have also a direct impact on the nature of the types of instability present in a system.

It has been shown that the most dominant parameters in TCF are the rotational speed of the inner or outer cylinder respectively and their direction of rotation. Andereck mapped flow regimes from various rotation rates as seen in Figure 1.8.

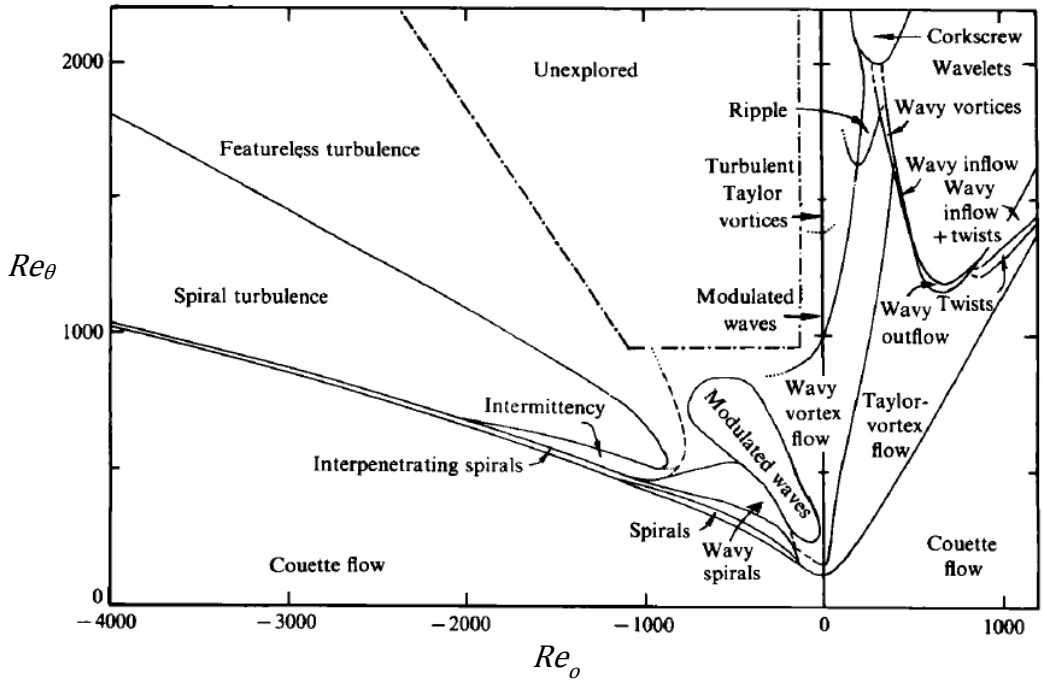

Figure 1.8. Regimes observed for Taylor Couette type instabilities at various Reynolds number. Dashed lines indicate transitions zones. Re_o: Outer cylinder Reynolds number; Re_θ: Inner cylinder Re-value. (Andereck 1986)

As is seen in Andereck's phase diagram, many regimes exist beyond the first instability which results in pairs of counter rotating vortices that surround the inner cylinder and exhibit certain characteristic frequencies as shown by (Koschmieder 1979, Ohmura 1997, She 2001, Wereley, Lueptow 1999, Chandrasekhar 1962), etc. Therefore, the flow regimes above the initial instability are often referred as Taylor Vortex Flow (TVF).

1.2.4 Taylor Vortex Flow and Wavy Vortex Flow

The instabilities that arise from Reynolds numbers above the critical value, resulting in the so called Taylor Vortices and their relation to rotation speed was thoroughly explained by Taylor through linear stability analysis on the flows with narrow gap, $\eta \approx 1$.

In Taylor Vortex Flow (TVF) the pairs of counter rotating vortices and their regimes are thoroughly discussed by (Di Prima, Swinney 1981) for cases with non-rotating end caps. Their work shows that for most radius ratios the vortex size approximates the gap size; moreover the system adapts to generate vortex pairs of heights larger/smaller than the gap in order to have an integer number of vortex cells (Wereley 1992).

Previous work has shown that in the narrow gap limit ($\Gamma>20$) (for the SFA $\Gamma= 27.5$), the end boundaries do not play a significant role (Taylor 1923, Di Prima, Swinney 1981, Chandrasekhar 1962). However, for systems with smaller ratios ($\Gamma<10$), the end-effects caused by stationary end plates are observable. Taylor Couette cells have a characteristic counter rotating nature, except when the length of the cylinder is short as shown by (Koga, E L Koschmieder 1989). They observed that, for a small aspect ratio $\Gamma<4$, the effects of the end boundaries affect the direction of rotation of the outer cells. For example, there could be a secondary toroid like rotation in both upper and lower boundaries. The mechanism for the generation of the secondary flow is due to imposed no-slip condition at the end plates and the outer cylinder wall. There, the pressure gradient due to the azimuthal velocity drives a radially inward flow around the end plates as explained by (Burin, Schartman et al. 2010). This secondary flow has a characteristic circulation akin to Ekman cells and is observed to spiral inwardly.

The Ekman cells generated in small aspect ratio TCF devices redistribute angular momentum within the system, which is seen as a problem in industrial devices such as spinning disk drives. A way to retard the generation of these cells it to rotate the end-boundaries at the same velocity as the inner cylinder. It was noted by (Burin, Ji et al. 2006) that rotating the end boundaries creates a velocity profile similar to Couette flow, by reducing the effect of Ekman circulation cells.

In Figure 1.8 as we move upward in Re_θ, (with $Re_{\theta_0} = 0$) the flow becomes particularly complex as shown in DNS simulations performed by Dong, 2007 ranging from Re_θ 1000-8000 with η=0.5. In these simulations as well as other experimental work, including that performed by Coles in 1965, shows that azimuthal waves originate in the system. This behavior, noted by (Di Prima, Swinney 1981, Wereley, Lueptow 1998, Barcilon, Brindley

1984, Akonour, Lueptow 2003), is dependent not only on the rotational speed of the inner cylinder, but also on the approach to the final rotational value. These observations are referred by (Wereley 1992) and elsewhere *as non-uniqueness* of the flow. This type of flow, is referred as Wavy Vortex Flow (WVF), is subject to the hysteresis effects.

A schematic representation of WVF is seen in Figure 1.9, where for the waves to travel around the annulus, transport of azimuthal momentum within the vortices should occur in the direction of rotation. The wavy vortex structures that rise were initially analyzed by (Barcilon, Brindley et al. 1979) and first observed by Pai in 1943. Barcilon et al. noted that at $1.92Ta_c$ wavy disturbances start to become visible at the wall.

At higher Taylor numbers, they also noted features smaller than the Taylor vortices with a highly ordered motion, these structures are thought to originate from centrifugal instabilities due to the curvature of the cylinders akin to the ones observed in Görtler vortices. The Görtler vortices orient themselves in the stream wise direction having a strong radial velocity component. If visualized, these structures appear as small wavy patterns on the each vortex for counter rotating cells. Barcilon et al. 1979 documented these structures at values of ~400 Ta_c.

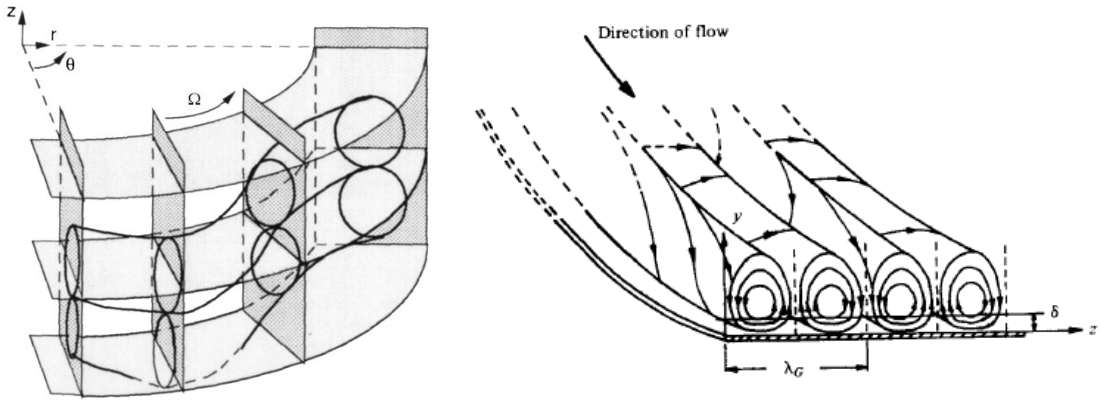

a. **b.**

Figure 1.9. a) Sample pattern of WVF for a vortex pair. Results obtained from a system with η=0.81; Γ=47.8 (Akonour, Lueptow 2003) b) Representation of the instability of Görtler vortices originating near the outer cylinder (Barcilon, Brindley et al. 1979)

These wavy motions were successfully simulated by (Dong 2007). In his results, it is shown that the tilting angle of the Görtler vortices increases as Re_θ is increased and thus matching results from (Barcilon, Brindley et al. 1979); since at sufficiently low Re_θ the Görtler instability cannot be sustained. These structures look similar to herring-bone patterns and appear as streaks in visualization images. Moreover, it was observed in the simulation that as Reynolds number is decreased to values near $\sim Re_\theta = 1000$ (for $\eta = 0.5$) the streaks disappear and therefore the instability cannot be sustained. On the other hand, at elevated Reynolds values, the coherence of the streaks starts to vanish as they become finer, closely packed and scattered. In regards to the mechanics of motion, Barcilon et al. 1979 proposed that the small scale motions observed by the herringbone pattern and the large scale seen as Taylor vortices interacts on a way that "each of them is a marginally unstable disturbance to the flow on the boundary-layer scale".

Furthermore, at Reynolds numbers higher than $Re_\theta = 1000$ ($\eta = 0.5$) other instabilities occur, as seen in Figure 1.8. In Modulated Waves Vortex Flow the instabilities have both smaller amplitude and frequency as explained by Wereley, 1992. It is seen that this flow regime is quasi-periodic and is symmetrical in rotation as WVF. Above these regimes, lies a region less understood than the aforementioned TVF, WVF, etc. The region of Turbulent Taylor Vortices contains packets of turbulent structures that arise as Reynolds is increased until the flow is characterized by featureless turbulence.

Moreover a masterful characterization of flow regimes has been recently completed by (Tokgoz, Elsinga et al. 2012) where flow structures were characterized using tomographic PIV. They were able to obtain instantaneous 3D flow structures for TVF and turbulent regimes allowing for computation of various statistical averages. Their set-up differs from our SFA, where there is no free boundary and the outer cylinder co-rotates in the same direction as the inner cylinder. However, they have catalogued the mechanism of formation of new Taylor vortices while in steady state. In the TVF case they noted that the initial mechanism of formation starts with the leading edges of a pair of counter-rotating vertical structures appear in the outflow region of an already established pair of Taylor cells (counter-rotating as well). The cells emerge in the region closer to the inner cylinder and later are displaced azimuthally. Tokgoz, Elsinga et al. point out that as the

new cells traverse azimuthally they expand and move toward the center of the gap, therefore displacing already established larger vortices axially. They noted that the reverse mechanism occurs for the disappearance of the vortices. Both cycles referring to the creation and elimination of the vortices appeared randomly both in space and time.

1.2.5 TCF with imposed axial flow

The foremost contribution of axial flow on TCF is the stabilization of the transition into Circular Couette Flow. The imposed flow delays the transition into TVF to higher Reynolds values. These observations by Min, Lueptow 1994, show that helical vortices may occur as a result of the axial flow, which move in the direction of the axial flow. In comparison to flows without axial flow at similar Rotating Reynolds number, the vortices appear to be stationary.

1.3 Objectives

In canonical Taylor Couette Flow, specific parameters and their relationship to the characteristics of the flow field are well documented (Di Prima, Swinney 1981, Taylor 1935, Andereck 1986), etc. Some of the known variables that play relevant roles in the flow regimes aside from Ta or Re_θ, are the radius ratio of the inner to outer cylinder, and the aspect ratio of the gap width to length of the apparatus. These parameters also play a role on the SFA, yet since the apparatus hereby studied deviates from standard Taylor Couette flow; additional features emerge that would otherwise not be present in standard devices (e.g. stationary vortices at the bottom and top of the apparatus). Moreover, the temporal and spatial characteristics of the vortices at similar Re_θ, η and Γ to other TCF type of experiments may as well be affected.

One could say there is a query to justify the operation of the SFA in order to explain not only its basic operation but also the scaling from laboratory into the industrial size. To scale-up the spinning film apparatus, a broader understanding of the interactions among upper plate width, flow rate and gap thickness is necessary. The interaction within these variables is non-trivial. Therefore, the main objective of this investigation is to quantify

the underlying dynamics of the free boundary both at the bottom and the top of the apparatus, the flow field in the gap and the overall response of the system to an imposed axial flow in which $W_g>0$.

In this document the behavior and existence of flow features that arise as a consequence of varying the aforementioned flow parameters is unveiled. The following are the main topics covered in this manuscript.

1. Perform measurements for various Re_0, W_g and f_s to document the location of the film surface, and the effect the top plate has on the radial location of the boundary at the bottom of the apparatus. The data is collected through visualization and interface probing with a point measurement technique.
2. Study the effect on the flow statistics generated by the transversal holes located in the inner cylinder. Specifically, to understand if there is a large scale circulation within the apparatus caused by the presence of these holes, which together have a larger surface area than the gap.
3. Study and characterize Taylor Couette like vortices in the gap and the effect of imposed axial flow on these structures. The main wavelengths of the vortices are obtained by flow visualization techniques.

   Moreover, the flow profile of the vortices is mapped in the gap. The flow statistics are recorded by applying point measurement techniques and single plane Particle Image Velocimetry (PIV).

4. Characterize the flow zones below and above the impeller and determine the effect of the upper plate and W_g. In these zones, flow statistics are obtained by using point measurements and single plane PIV.

Chapter 2

Experimental Facilities & Methodologies

2.1 Experimental Setup: Spinning Film Apparatus

2.1.1 Spinning Film Apparatus

The experiments in this study were performed on a replica of the SFA manufactured at the University of Minnesota on a laboratory scale.

The commercial apparatus is made of stainless steel both the inner and outer cylinders. The machine has an external jacket where chilling water or other liquids could be used to regulate the temperature within the SFA. The amperage consumption of the motor and rotation speed are controlled via firmware. The acquisition system collects data on amperage consumption and temperature variations. To obtain other product or flow variables one must analyze and compare input vs output specific characteristics. This set-up largely limits the ability to obtain flow data directly from operation. Therefore, to understand the flow characteristics one must modify the industrial apparatus in order to observe and quantify the underlying factors that allow the SFA to have a high milling efficiency when compared to other comminution devices.

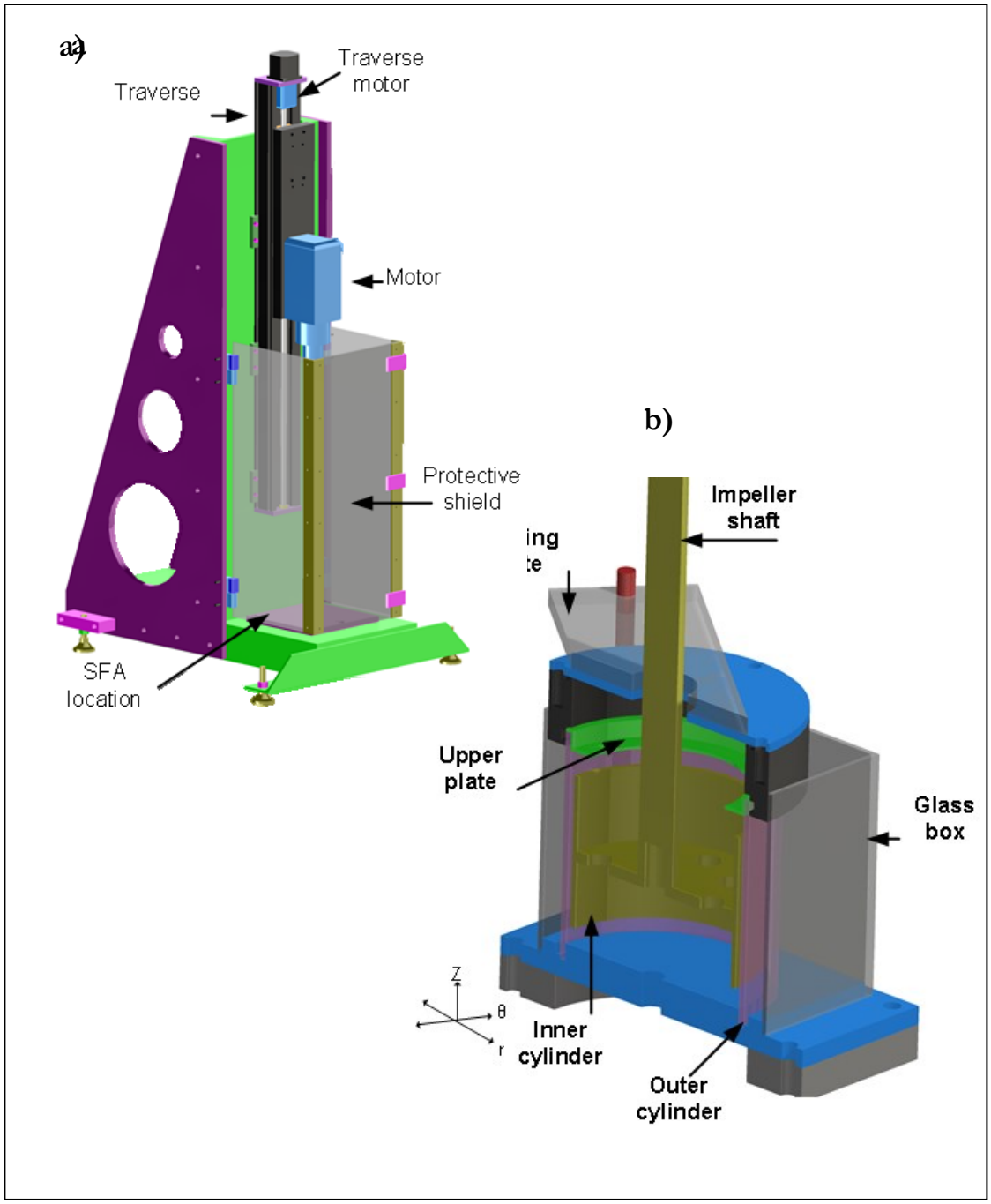

Figure 2.1. CAD drawings of the Spinning Film Apparatus. a) Side view of the impeller traversing mechanism and visualization box. b) Cross section view of the SFA for continuous operation, f_s= 9mm. Mechanical assembly and drawings by Dave Hultman.

The University of Minnesota apparatus was partially manufactured at the Mechanical Engineering machine shop and by Dave Hultman Design, LLC. The design focused to allow for optical access and to minimize optical aberrations produced by the curvature of the outer cylinder. In that matter the inner cylinder is made of anodized aluminum to minimize reflections. The outer cylinder is made from clear borosilicate glass and the bottom is casted from polymethyl methacrylate (Plexiglas®). The cylinders are enclosed in a clear glass box (therein known as the optical box) that allows optical access around the cylinder.

The upper part of the SFA has various exchangeable annular rings that are changed according to the type of experiment (batch or continuous); see Figure 1.5 and Figure 2.2 for schematics. These rings are called upper plate (f_s), and are manufactured of polyvinyl chloride (PVC). Above the upper plate is the upper section, which the liquid reaches only in the continuous mode. In that condition, after "climbing" the upper plate, the fluid finds a path to the outer port on the side of the apparatus. The upper section is made of (PVC) and during operation is carefully attached to the upper cylinder in order to avoid leakage into the optical box, allowed by various o-rings placed along the upper section. The dimensions of the experimental set-up are described in Table 2.1.

Table 2.1. Dimension of experimental set-up

Symbol	Description	scale
d_h	Diameter of one transversal hole	10.2 mm
d_{lp}	Inlet port diameter	10 mm
H	Length of impeller	55 mm
h	Space between impeller and bottom	5 mm
h_T	Space between upper plate and impeller	10 mm
L	Length of vessel	70 mm
r_i	Impeller radius	38 mm
r_o	Large cylinder radius	40 mm
δ	Gap thickness	2 mm

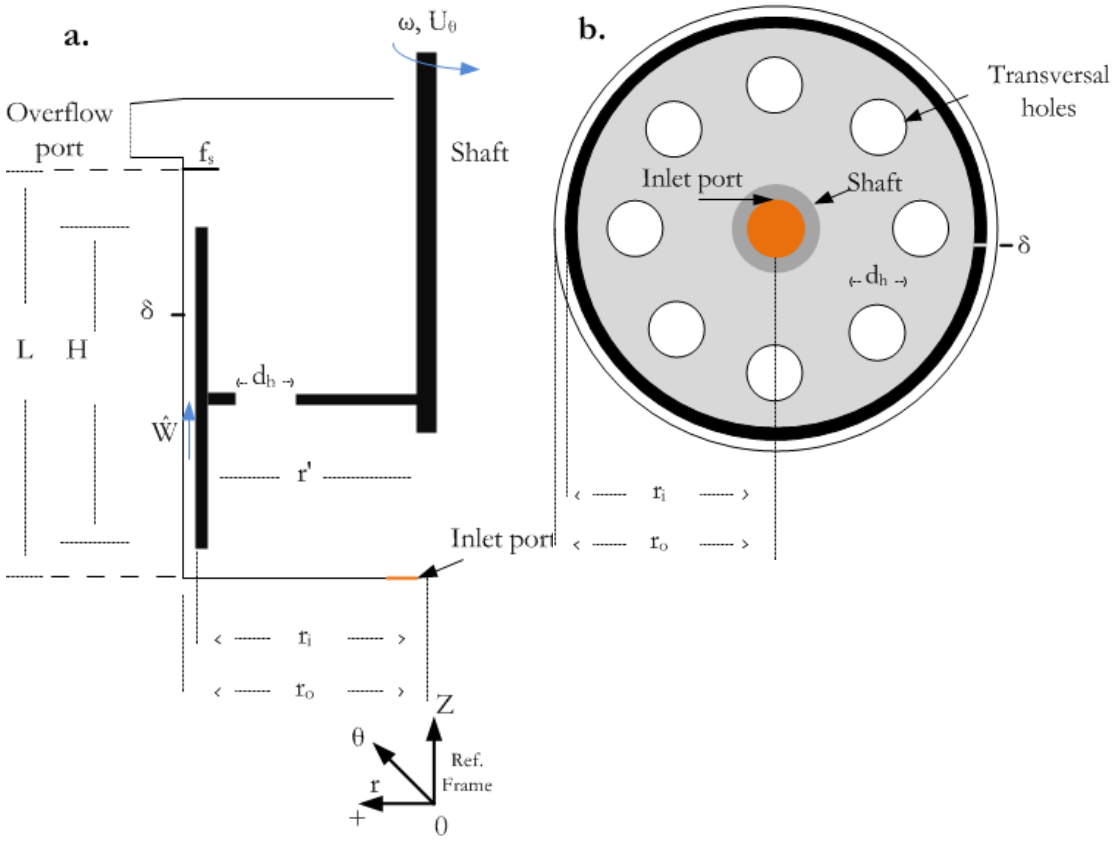

Figure 2.2. The pictorial diagram shows a) shows a vertical cross section of the SFA with the coreresponing geometrical variables and frame of reference. b) scaled radial cross section of the apparatus.

The tolerances and thicknesses of the upper plate, inner & outer cylinder and the glass box are described in Table 2.2.

Table 2.2. Dimensions and tolerance of the lower section of the SFA used in these experiments

Lower Section	
Part	Thickness [mm]
Inner cylinder	2 ± 0.08
Outer cylinder	3 ± 0.07
Bottom of apparatus	4 ± 0.05
Optical Box	2 ± 0.06

The cross sectional view of the SFA in Figure 2.2, shows that the apparatus can be split in two large sections. The lower part is where the experimental observations take place and the uppermost is used as means of controlling the film thickness. The vertical impeller location was chosen in such way that a separation between its lowest point and the bottom of the vessel is $2.5\delta=h_L$. The upper section is only used in the continuous case, its main purpose is to function as an overflow section where the film spins and evacuates through the outflow port (overflow port) as mentioned before.

Table 2.3. Dimensions and tolerance of the upper section of the SFA used in the experiments hereby described.

Upper Section

Part	Dimensions [mm]
Upper plate thickness	0.5 ± 0.1
Overflow chamber diameter	80 ± 0.15
Overflow chamber height	20 ± 0.5
Overflow port inner diameter	13 ± 0.08

For these experiments the SFA used an aluminum inner cylinder (impeller) that was anodized in black color as means to reduce reflections. The scattered light was produced by the various light sources utilized to collect velocity statistics and/or particle position. The step of anodizing increases the thickness of the natural oxide layer atop the impeller. In our experiments this part was anodized in a type II sulfuric acid bath**,** which deposits an oxide layer 0.018 mm–0.025 mm thick on the surface of the cylinder. The oxide layer is included in the measured r_i. The inner cylinder as seen in Figure 1.5 has 8 transversal holes of d_h = 10.2 mm. These holes are also part of the industrial designed apparatus. They account for 13% of the cross sectional area of the SFA as seen in Table 2.4, compared to the gap which is 9.8%.

Table 2.4. Dimensional overview of the impeller holes and gap compared to the vessel cross-sectional area.

Parameter	Cross sectional area [mm^2]	$\frac{\text{Parameter}}{A_T}$
Vessel diameter [T]	5.026×10^3	1
Gap [δ]	490.08	0.098
Transversal hole [$8 \times d_h$]	653.68	0.13

2.1.2 Batch condition

In the batch scenario, the inlet port is sealed flush with a screw-plug and the liquid/particle mixture necessary to perform the experiment is poured before placing the impeller in position. In this experimental condition both the spatial and temporal characteristic of the flow field are dictated by the Reynolds number and the holding volume ratio.

The liquid with tracing particles rests at the bottom of the apparatus when the azimuthal velocity is zero. Then at the chosen rotation speed, the liquid forms an annulus with nothing more than atmospheric air filling the innermost part as described in Chapter 1. The free boundary of the film extends from the bottom of the apparatus to the location where the impeller attaches to the shaft. A free boundary is also formed extending from the upward facing side of the impeller-shaft connection, to the ceiling of the apparatus. The ceiling/top in batch is the upper plate; in continuous flow the film extends beyond the upper plate and it is possible that it reaches the top of the upper section of the apparatus. The initial holding volumes used throughout the experiments in the batch and continuous case are 0.3 V_T, 0.42 V_T and 0.54 V_T.

The theoretical thickness of the film is the thickness of the annular region between the outer cylinder and the air interface. The free boundary thickness is then proportional to the initial liquid holding volume in the apparatus. Both the thickness and location of the free boundary are discussed in manuscript.

Table 2.5. Holding volumes of fluid used to perform batch experiments.

Fraction of V_T	Volume used [mL]
0.3 V_T	104
0.42 V_T	150.5
0.54 V_T	192.2

When no through flow is applied, as in batch mode, the upper plate extrudes radially inward to a distance of 1δ away from the shaft of the inner cylinder (18δ). In this condition there is no through flow and the inlet port is closed.

The values of Re_θ used in the experiments span from 1110 up to 3180, which are similar to values used in industrial operation for viscous coal and petroleum coke slurries, even though U_θ and μ are both lower in magnitude in comparison to the industrial scale operation. In the industrial case, being the viscosity of the dispersion larger than the fluid (water) used in the experiments with the SFA, the Reynolds number (e.g. Re_θ=3180) matches the values for industry.

Table 2.6. Dynamic conditions used with the SFA during data acquisition.

Re_θ	U_θ [m/s]	ω [rad/s]
1110	3.5	14.7
2230	7	29.3
2544	8	33.5
3180	10	41.9

2.1.3 Continuous Flow

The upper plate width in continuous flow f_s relates to holding volume ratio by creating a film having a thickness similar as in the batch mode. In cases with 0.54V_T this plate has a width of 19.5δ (39 mm) in the batch condition; comparatively in the continuous case the plate has a width of 3δ (6mm), 4.5δ (9 mm) and 6δ (12 mm).

In the continuous case, all aforementioned geometrical parameters are kept constant. The inlet port is circular in shape and centered on the cylinder axis. It has a diameter of slightly over 5δ (10 mm) and any fittings are flush with the bottom of the vessel. However, under this condition (continuous mode), a jet of fluid exiting the inlet port impinges on the impeller shaft bolt.

Table 2.7. Experimental parameters for axial through flow

f_s [mm]	V_{fs} [mL]	$\frac{V_{fs}}{V_T}$	$\dot{Q}\left[\frac{mL}{s}\right]$	$W_g\ \left[\frac{m}{s}\right]$	t_r [s]	t_g [s]
6	104	0.3	20.8	0.042	5	1.3
			6.9	0.014	15	3.9
9	150.5	0.42	30	0.061	5	0.9
			10	0.020	15	2.8
12	192.2	0.54	38.4	0.078	5	0.7
			12.8	0.026	15	2.1

In Table 2.7, f_s represents the upper plate thickness, V_{fs} the theoretical volume of the free boundary, and $\dot{Q}$ the volumetric flow rate of liquid into the SFA. These parameters are used to calculate the axial velocity in the gap W_g, the nominal residence time t_r and the gap residence time of the fluid t_g. The theoretical volume of the free boundary is calculated using the volume of an annular region with thickness f_s and height L; see Figure 2.2.

The nominal residence time is used in reference to the industrial operation in order to relate the time it takes to one volume of the free boundary to be displaced in its fullness by the volumetric flow rate. On the other hand, the residence time in the gap accounts to the time it takes the volume in the gap to be fully renewed. In these experiments is considerably smaller than the upper plate thickness.

In the continuous case, the overflow port tube (12 mm) discharges into the atmosphere at the mixing reservoir. For this reason in Figure 2.3 the recirculation tank is placed lower in height, compared to the overflow port.

2.1.4 Flow circuit

In the continuous flow experiments, the liquid was introduced into the SFA through the inlet port at the bottom of the apparatus. The axial through flow is imposed and controlled by a positive displacement Masterflex ® pump, model 7518-02. This type of pump generates a pulse with a characteristic frequency depending on the flow rate. Therefore, a pulse dampener was included in the flow circuit in order to minimize the impact of these pulses.

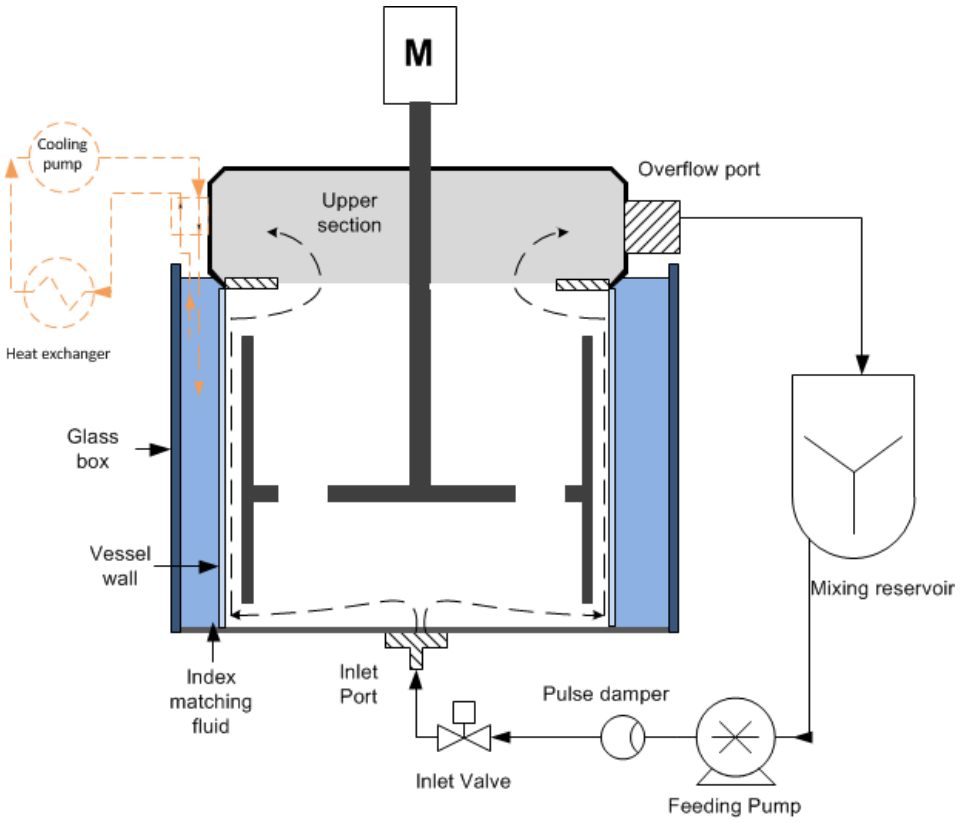

Figure 2.3. Flow loop schematic diagram with the temperature control loop.

The pump has a maximum flow rate of $30\frac{mL}{s}$, and the pulse dampener contained a volume of $0.53V_T$. The flow was kept in recirculation by using the overflow port to deliver fluid into an open tank holding 1 L ($\sim 3V_T$). The fluid delivered to the recirculating open tank was then directed back into the SFA.

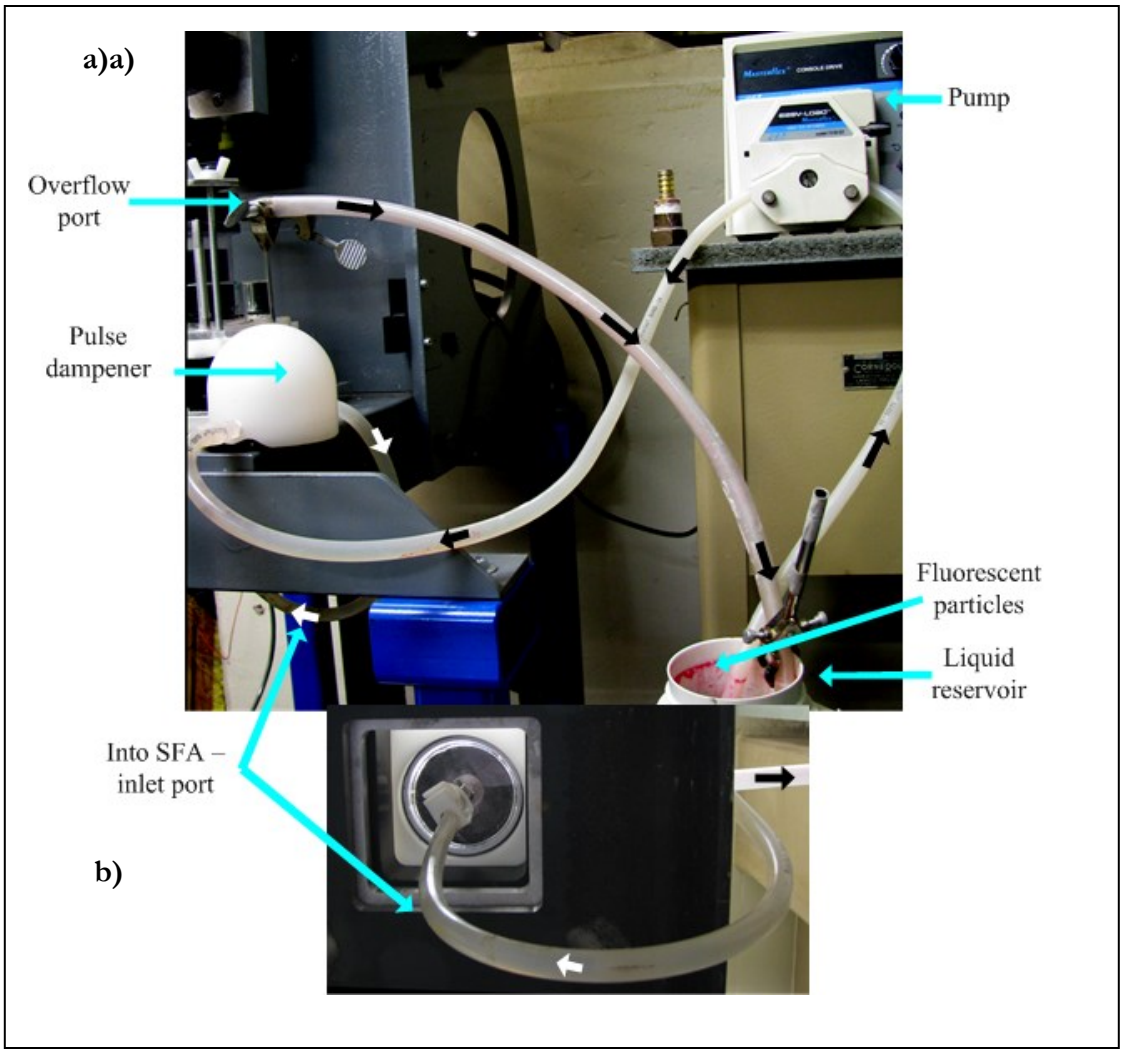

Figure 2.4. a) Flow loop with pulse dampener, feeding pump and liquid reservoir (holds $3V_T$). b) Bottom view of the SFA, the black circle is the impeller.

In Figure 2.4 the fluid leaving the overflow port flows into the liquid reservoir. In this state bubble entrainment was avoided by placing the overflow tube tangential to the wall of the reservoir, in this way an impinging jet was avoided. The flow was then pumped, passing through the pulse dampener. From the pulse dampener fluid was directed into the inlet port as shown in Figure 2.4b.

2.1.5 Temperature control and fluid properties

In both batch and continuous modes, the fluid used to perform the experiments was deionized water at room temperature. Moreover, deionized water was poured into the glass-box and used to match the index of refraction within the SFA. Water with dissolved minerals was not used as it leaves evaporation marks on the outer cylinder and the glass box container.

In steady state operation, heat is generated within the SFA. In batch mode at the experimental conditions, the temperature of the liquid within the SFA increased between 10°C to 20°C from the baseline (room temperature). Therefore, a system to minimize the impact of the increase in temperature on the fluid viscosity was adapted to the experimental apparatus.

In that matter, water from the glass-box was pumped using into an aluminum casing submerged in an ice-bath. The casing acted as a heat-exchanger by reducing the mean temperature of the glass-box. Using the temperature loop, the mean increase in temperature of the fluid inside the SFA was 3°C lower than room temperature (22°C) at Re_0 =2230.

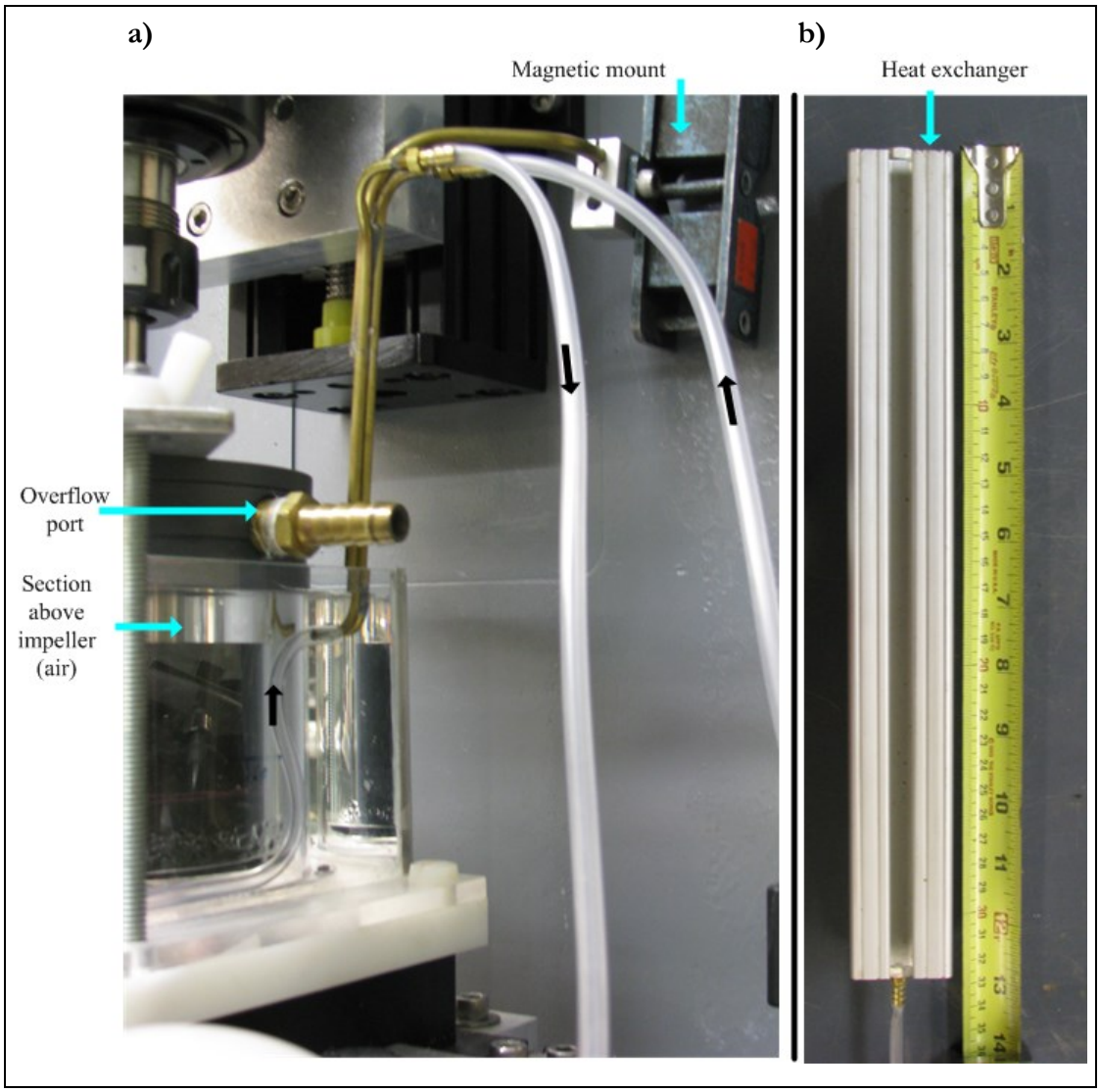

Figure 2.5. a) Temperature control circuit with inlet and oulet ports into the glass box. b) View of the rudimentary heat exchanger inner casing. The aluminum shell is submerged on a water bath with known temperature.

2.2 Seeding Particles

2.2.1. Tracking particles

For the experimental techniques of Laser Doppler Velocimetry (LDV) and Particle Image Velocimetry (PIV) various types of particles are recommended according to specific experimental needs. In both techniques the particles need to larger than the incident wavelength for them to be on the Lorenz-Mie scattering regime. Otherwise if the particle diameter is smaller than the incident wavelength, the scattering moves into Rayleigh regime. In the Mie domain the intensity of the scattered light is the sum of the diffracted and geometrical scattering, both are proportional to the light energy intercepted by the area of the particle $\sim d_p^2$ (Adrian, Westerweel 2011). For this reason, to maximize the exposure on a PIV image it is of convenience and economical reasons to choose the appropriate particle type/size over increasing the laser power input.

In the Mie scattering regime the normalized parameter in terms of particle diameter $\boldsymbol{q}$ can be used to characterize the intensity of light scattered for a particle between 0° and 180°.

$$\boldsymbol{q} = \frac{\pi d_p}{\lambda}$$

In the case that $\boldsymbol{q}$ is larger than unity; there is a distribution of intensity vs. scattering angle, such that forward scattering is typically orders of magnitude stronger than backscattering.

Where possible, it is desirable to use forward scattering to attempt to obtain the largest scattered power from the respective particles as shown in Appendix C, assuming the particles are spheres (Raffel, Willert et al. 2007). It is seen that at 90° the scattered intensity is small for polyamide particles at 60 μm. On the other hand, for the smaller particles used in LDV, the scattered intensity at 0° (forward scattering) is considerable larger than the previous scenario (90°), compensating for the lower laser power used in the LDV system.

Appendix C shows the polar diagram for the scattering of the tracer particles. The particles for LDV (~10 μm, 1.01 $\frac{g}{mL}$) were chosen due to their ability to follow the fluid streamlines accurately. To quantify the truthfulness of the particle tracking ability is cumbersome, especially in highly three dimensional flows such as TVF, where large spatial gradients occur within relatively small distances (wall-to-wall). As an estimate, one can use the inertial time constant derived from the momentum equation applied to an accelerating particle; as means to estimate the particle ability to respond to changes occurring in the domain of interest:

$$\tau_P = \frac{\rho_P d_P^2}{18 \nu_f \rho_f}, \text{ is the inertial response of a particle}$$

where, ρ_P and ρ_f are the particle density and fluid density respectively, d_P the particle nominal diameter and ν_f the fluid kinematic viscosity. This time scale can be compared to the time-scale of a representative eddy in the fluid on a particular spatial domain as:

$$St = \frac{\tau_p}{\tau_f} = \frac{\tau_p U_\theta}{\delta}$$

$$\tau_f = \frac{\delta}{U_\theta}$$

In these experiments, the domain is the gap between the inner and outer cylinder $\boldsymbol{\delta}$, where shear occurs due to the azimuthal velocity $\mathbf{U_\theta}$.

In Table 2.8, the variable d_p stands for particle diameter, τ_p particle time constant and St Stokes number. To obtain an approximation for the Stokes number the azimuthal velocity U_θ has a value of 3.5 $\frac{m}{s}$ (Re_θ =1110) and δ of 2 mm. Vestosint particles (used for LDV) are reasonable responsive at these conditions, while the PIV particles (20 μm & 60 μm, 1.03 $\frac{g}{mL}$) are less responsible. Moreover, the fluorescent particles are observed to be less responsive than the LDV particles at equal conditions.

For Re_0=2230, the same trend is observed. The LDV particles are still quite responsive, while the 20 μm PIV particles are still within acceptable range of responsiveness. However, the Stokes number for the 60 μm PIV particles at the highest Reynolds number is close to unity, therefore making them less suitable for tracking at this condition. At this Reynolds number, the fluorescent particles are observed to be less responsive

Table 2.8. Shows values of the inertial time constant and the Stokes number for tracking particles used in the LDV and PIV experiments. The LDV and PIV particles are manufactured out of polyamide resin, with density of~1010 kg/m³ and index of refraction of n=1.5. The fluorescent particles are made of styrene-divinylbenzene, ϱ=680.

Use	Commercial Name	d_P [μm]	τ_p [μs]	St	
				Re=1110	Re=2230
LDV	Vestosint 2159	9	4.6	0.008	0.02
PIV	Orgasol 2002 NAT1	20	22.8	0.040	0.08
PIV	Orgasol ES6 NAT3	60.3	207.4	0.363	0.73
Fluorescent	Sepabeads SP20SS	60	135.6	0.24	0.47

From the table one can infer that the response time of the particles is appropriate for the flow conditions.

2.2.2. Visualization particles

Taylor Couette Flow visualization has historically been made by using reflective particles, dyes and bubbles (Wereley, Lueptow 1994, Di Prima, Swinney 1981, Barcilon, Brindley et al. 1979, Andereck 1986, Prigent, Dauchot 2000, Gauthier, Gondret et al. 1998). In the experiments hereby shown, visualization was made using particles from the Kalliroscope corporation. These particles (Kalliroscope) are flake like with a length of 30 μm in the largest axis, they are commonly used in TCF and TVF experiments due to their anisotropic properties.

It was found by Gauthier, (2008) that these particles orient themselves according to their larger axis by means of following the stream surfaces, as described by (Savas 1985).The Kalliroscope particles are said to be anisotropic since they orient themselves according to

the shear gradients in the flow, scattering light according to their orientation. It was also suggested that these particles can follow the stream lines of the flow field although they are not spherical in nature. (Gauthier, Gondret et al. 1998, Matisse, Gorman 1984).

Table 2.9. Physical characteristics of Kalliroscope particles. Data from Matisse & Gorman, 1984.

Description	Dimension
Material	Guanine
Mean size [μm] (LxWxH)	30×6×0.07
Particle density [g/cm^3]	1.66
Refractive index (solution)	1.85

For successful visualization of Wavy Vortex Flow and nominally Turbulent Taylor Vortex regimes, the recommended dilution of the stock dispersion of Kalliroscopic particles is between 0.5% - 3% $\frac{v}{v}$. Others have also found that in the narrow gap scenario (as described in the experiments shown herein) one could increase the particle concentration up to 25% by volume. Although to increase the particle concentration will also increase the apparent viscosity of the fluid. Nevertheless, the dependence of the viscosity on the local shear rate was found to be negligible at 25%$\frac{v}{v}$ ∴ still Newtonian (King, Lee et al. 1984, Matisse, Gorman 1984, Prigent, Dauchot 2000).

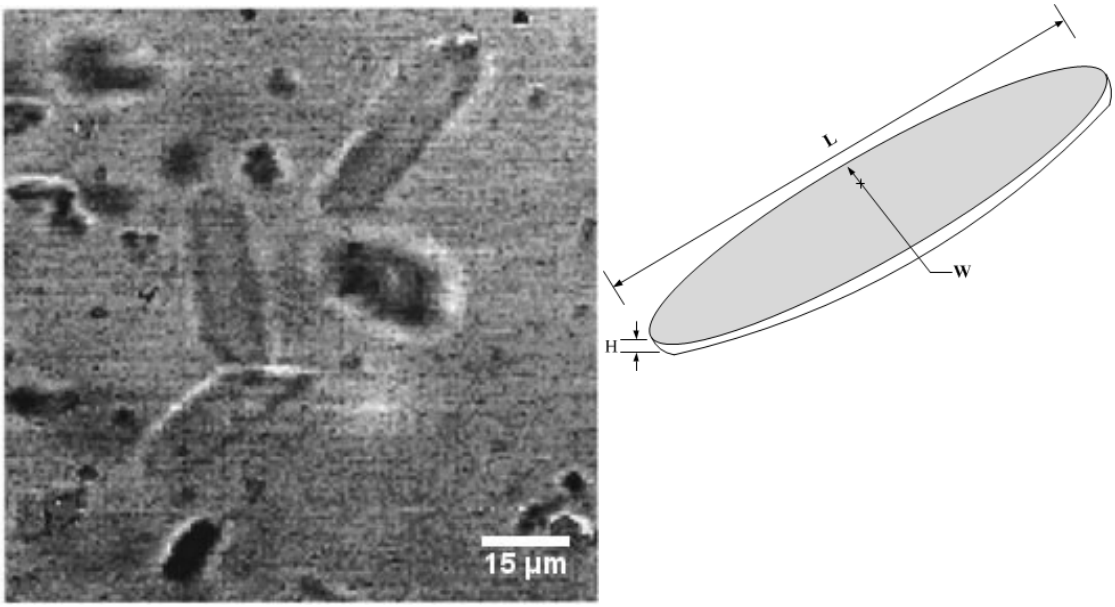

a) b)

Figure 2.6. a) Microscope image of concentrated Kalliroscopic particles, from Gauthier et al. 1998. b) Cartoon showing the flake like structure of a Kalliroscopic particle.

The concentration of these particles on in stock solution provided by the Kalliroscope corporation for the AQ-1000 concentrate product is unknown. However, analysis made by (Gauthier, Gondret et al. 1998) determined the estimated concentration of particles to be in the order of $1\times10^{6}\,\frac{\text{particles}}{\text{mm}^3}$. The measurement was performed by optical microscope observation after drying a sample of the dispersion.

The results obtained by flow visualization using these particles shown in this manuscript are performed with the industrial dispersion diluted to a maximum of $3\%\frac{v}{v}$ of total volume. The particle solution was accounted as part of the used holding volume for experimentation. Moreover, at higher concentrations (4-5% v/v), it was found that the scattered light from the particles was constant, therefore making unnecessary to increase the number of particles in the holding volume.

2.2.3. In-house manufacturing of fluorescent particles and implementation

The combined use of fluorescent particles in tandem with standard tracking particles is a resourceful practice, as it allows masking one type of particle using optical filters. In the case of the experiments described herein, a non-concentrated dispersion of neutrally buoyant (polyamide) particles (<1% V/V) was seeded with an almost negligible (<0.5% $\frac{V}{V}$) volume of fluorescent particles. The fluorescent particles are of similar or smaller size than the regular tracking beads depending on the experiment. Then, by applying optical filters the behavior of the fluorescent particles was emphasized, allowing them to be used for flow visualization.

A major impediment regarding the use of fluorescent particles is their elevated cost. Currently the cost of using these fluorescent particles on experiments not associated to microPIV is prohibitive. For quick reference, the cost of 100 g of brand particles is in the order of US $2,000, which limits their usage to small scale experiments (Pedocchi, Martin et al. 2008). For that reason, it seems appropriate to find a method to manufacture a large amount of these particles, even if the median operational life of them is considerably smaller than the industrial cousins. In the PIV and flow visualization experiments described in this document, the particles are used within 42 hours of being suspended in water, because they release of fluorescent dye into the carrier fluid.

The particles chosen as carriers of dye, namely Rhodamine 6G, are commonly used for high performance liquid chromatography (HPLC) as chemical carriers. They are manufactured by Mitsubishi Chemical Co. and are part of the family of products named SEPABEADS™; code SP20SS. These beads perform as adsorbent particles for chemical separation with a surface area in the range of ~500 $\frac{m^2}{g}$, and a mean pore radius of 266Å. In contrast Rhodamine 6G molecules have a maximum steric diameter of 15Å (Kievsky, Carey et al. 2008). Using those values as ballpark approximations, if only sizing is taken into account without considering the interaction of forces such as Van der Waals between the dye molecules and the SEPABEADS™, one can expect that rhodamine molecules will effectively fit into the pores of the particles; making them suitable carriers.

These particles have an estimated mean size of 75 μm, with an upper bound of 100 μm and a lower bound of 15% of particles < 63 μm; the reported density for the soon to be fluorescent particles is in the range of 680 kg/m^3. These particles are suitable for separating slightly hydrophilic materials as described by the manufacturer; however they are hydrophobic by nature, as they are made of cross-linked styrene-divinylbenzene polymer. Therefore, the use of a surface active agent to allow mixing the particles in water is required.

The technique of utilizing adsorbent particles as carriers, was used previously to perform single plane PIV measurements on structure induced vibrations as a result of a cross flow (Someya, Kuwabara et al. 2010). However, the information on the procedure regarding the manufacture is limited in the article. The overall methodology used in this thesis for manufacturing such particles is similar to techniques currently in development at the Center for Nonlinear Science at the Georgia Institute of Technology by Daniel Borrero. The technique is derived from experiments performed by (Pedocchi, Martin et al. 2008). However, the use of specific surfactants at various steps is specific to the method henceforth shown. Here is introduced a concrete and simplified method for manufacturing low-cost fluorescent particles suitable for PIV/Tracking applications.

1. Initial sieving
    a. The SEPABEADS come in polydisperse fashion; therefore an initial sieving step is required. The particles are first pre-mixed in a aqueous solution containing 0.09% v/v of Witconol-14 (Akzo Nobel Surface Chemistry LLC) a surfactant with an estimated hydrophilic-lipophilic balance (HLB) of 6.
    b. After wetting the particles they are then sieved with tap water through various U.S standard ASTM sieves; namely No. 200 & 270 (75 μm & 53 μm hole diameter). The particles that pass through the No. 270 sieve are filtered and washed through a 10 μm hole diameter plastic mesh.
2. Particle preparation
    a. In this step the particles are mixed with a solution of 0.014M of Rhodamine 6G (Sigma Aldrich) in histological grade alcohol (Ethanol, Isopropyl Alcohol, Methanol) mixture (Fischer Scientific). It was found that a lower Molarity of

the mixture (0.005M) could also be used to manufacture the particles. Yet, the final emission intensity of the fluorescent particles would be lower, which could present issues when performing experiments. The mixture is thoroughly homogenized for 8 hours with the open end of the vessel covered to reduce evaporation of the solvent.

b. After stirring the particles, the solvent is discarded and the particles are washed with tap water to eliminate the excess dye. Continued washing should be performed until leaching of dye is almost unnoticeable.

c. After removing the excess dye, the particles are homogenized on a solution containing Sodium Dodecyl Sulfate (SDS) (4.62×10^{-5} M). The mixture is stirred for 4 hours in order to remove the excess dye. If the excess dye is not fully removed, the experimental liquid will fluoresce ass well, therefore reducing the contrast of the particles.

3. Drying
    a. After removing the excess dye, step 2.b is performed again.
        i. SDS is a commodity type surfactant; with the ability to cause foaming. Therefore, it is important to wash the particles thoroughly
    b. Now the particles are dried at 60°C for 2 hours.
        i. This step allows the particles to be stored without leaching extra dye if they were to be kept in solution.
4. Usage
    a. Pre-wet the particles by mixing them in distilled water for 30 min. The wetting procedure can be helped by using additional wetting agents. After successfully wetting the particles they are ready to be put to use.

Wetting the particles allows them to be homogenously suspended in the fluid making them viable for Velocimetry measurements. The particles were placed in the apparatus as soon as the wetting step was finished. Once in the apparatus, the experimental run lasted less than ten minutes. It was observed that if the fluid carrying the particles is left unattended, the particles will start to float in the surface of the vessel where they are kept. The time it takes before the particles start to migrate is longer than the experimentation time.

The dyed particles are excited using a single pulse Nd:YLF laser, with a emitting wavelength of 527 nm. It is noted that Rhodamine 6G has a quantum yield of 0.92 ±0.02 in water (Magde, Wong et al. 2002), compared to Rhodamine B with a 0.65 yield (in EtOH) (Kubin, Fletcher 1982). The adsorption peak of Rhodamine 6G is near 532 nm with an emission peak above 550 nm, see

Figure 2.7 for reference. The two dyes have considerable adsorption peaks at the lasing wavelength, hence the required comparison.

Note that quantum yields tend to vary according to the reference solvent, concentration of dye and other factors such as temperature. Nevertheless, the uncertainty found in those results (ethanol or water as solvents) is less than the scale difference in quantum yield between both dyes as shown by Kubin, Fletcher, 1982.

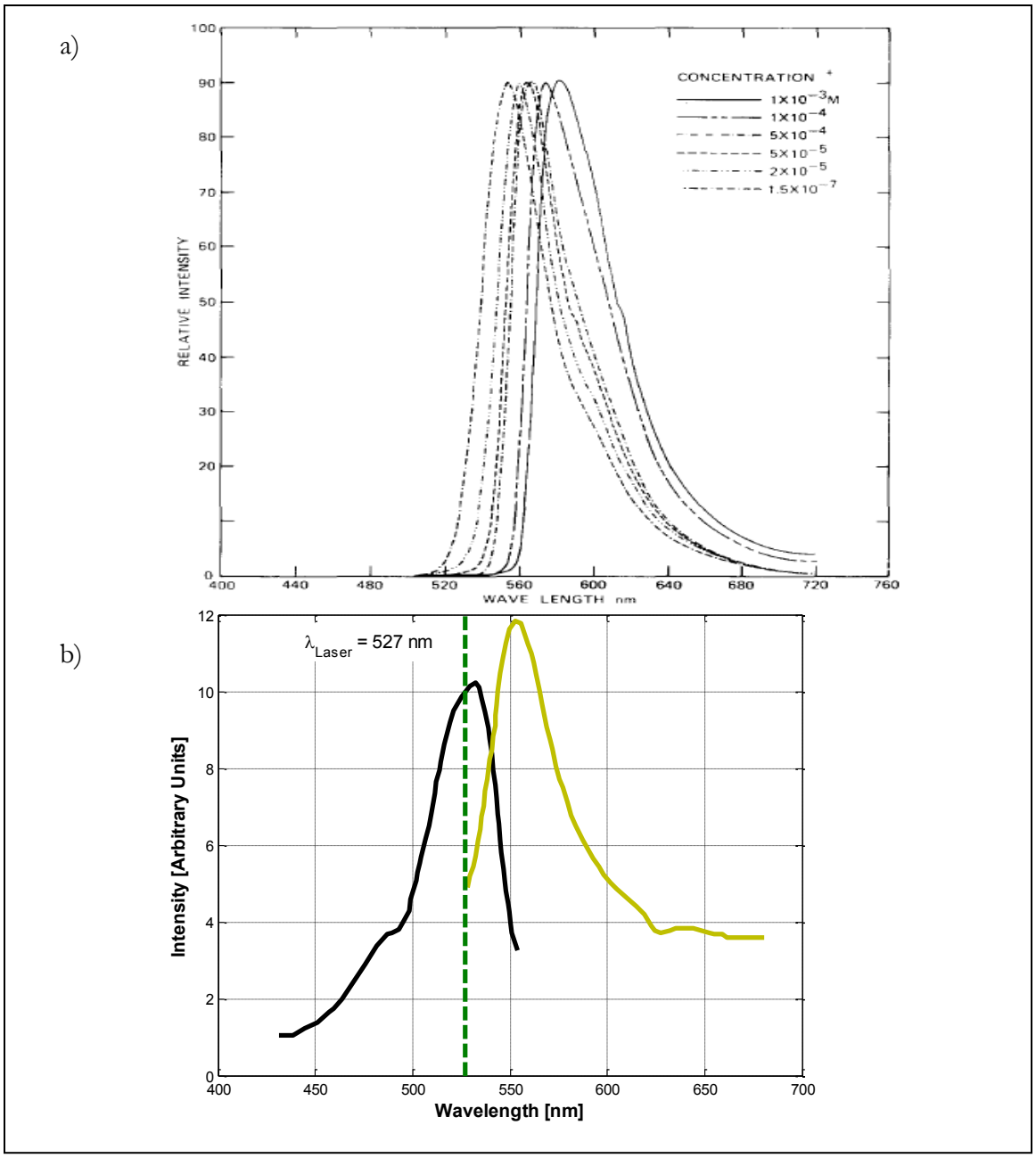

Figure 2.7. a) Fluorescence spectrum of Rhodamine 6G at various concentrations (Kubin, Fletcher 1982). b) Excitation and emission spectrum of Rhodamine 6G in EtOH, extracted from (Levy, Reisfeld 1984). The balck line indicates excitation range, yellow indicates emission range. Marker (--) indicates the lasing wavelength (527 nm).

Figure 2.7a shows the intensity plots at various concentrations in which a solution of Rhodamine 6G is excited. The plot indicates shows that increasing dye concentration shifts the emission profile towards higher wavelengths.

The initial concentration used to make fluorescent particles is two orders of magnitude higher than the ones shown in the plot. It is then expected that the adsorption/emission profile would be shifted. Nevertheless, since various dilution steps are used to remove the excess dye in the particles, it is expected that the nominal concentration within particles is smaller than the initial one.

2.3 Measurement Methods

2.3.1 Laser Doppler Velocimetry

The non-intrusive experimental method of Laser Doppler Velocimetry (LDV) was used to obtain averaged velocity statistics in the gap and the region beneath the impeller. In brief, the technique consists of intersecting two beams of coherent light with equal wavelength at a known angle κ, thus creating a volume of ellipsoidal shape. One of the beams is shifted by a known frequency relative to the incident beam from the laser head (40 MHz in this case), the intersection of the shifted and un-shifted beams then creates a moving fringe pattern.

The fringes translate at a constant speed across the measurement volume. When tracer particles pass through the volume they scatter light (in backscatter mode) into a photoreceptor located at the probe head. The speed by which the particles move through the volume is determined by calculating the shift in frequency from the scattered light bursts. The bursts are registered by a photomultiplier at the probe head. The velocity of the particles crossing the measurement volume is calculated by a frequency processor. The calculated velocity refers to particles traversing normal to the direction of motion of the fringes created by the Doppler shift.

Flow characterization using the LDV technique was performed using a TSI LDV system including a 9201 ColorBurst multicolor beam separator. This apparatus separates the

incident laser beam into different wavelengths used to measure two components of the velocity vectors. A PDM-100 Photo multiplier for acquisition registers the scattered light, a FSA-350 processor determines the speed of the passing particles, and TSI proprietary software (FIND) analyzes and records the data. The light source used in these experiments comes from a 100 mW 54900-Argon Ion laser (Ion Laser Technology). The light beams used to obtain velocity statistics had the following wavelengths: 514 nm (green) for the azimuthal component, and 488 nm (blue) for the axial component of the velocity.

The system was set up in such a way that the probe could be traversed at will in both the radial and axial directions. The radial displacement ensured to be towards the center of the apparatus and perpendicular to the glass box, therefore minimizing the angle bias source of error. The displacement of the optical probe (carrier of photovoltaic cell, focusing optics and light source) was automated with a Velmex-9000 step-motor controller programmed using FIND software. The location of the traversing mechanism that carried the optical probe is shown in Figure 2.8.

The resolution of the traversing mechanism is ($1.2\frac{\mu m}{step}$, $1.0\frac{\mu m}{step}$) on the (r,z) axis respectively. The system uses two independently controlled step motors, a Vexta Pk266 and a M062-LS9 for the radial and axial translation respectively, as seen in Figure 2.8a. The measurement volume is displaced along the SFA using this traversing mechanism, which is calibrated accordingly.

To accurately calibrate the traversing system, a highly seeded flow condition was used on the SFA, operating at the lowest Reynolds number. The flow was seeded with TiO_2 particles that have a larger refractive index than the tracer particles described in section 2.2.1. The calibration measurements for the traversing were performed at the middle of the gap (0.5δ) and 0.5 H (*H = length of the impeller*).

At that location the traversing motors are given commands to displace the LDV probe, consisting of the number of steps the motors need to execute when the "go" signal is given. The LDV probe was used to register changes in data rate and velocity statistics as a

result of traversing through the gap. By doing so it was determined that at the stationary wall side, a minimum of 5 steps per traversing command were necessary to register any difference in data rates in either the axial & radial velocity components (at $Re_0 = 1110$).

Emphasis was placed on accurately traversing the probe as data collection was partially automated and misalignment will cause errors. In that matter, a safety factor of 2 (20 steps) is used over the minimum number of steps required to send a command to initiate traversing of the probe. Moreover, a maximum traversing velocity of 100 $\frac{\text{steps}}{\text{s}}$ was employed as additional means to reduce traversing error which causes position bias on the registered velocities. Traversing the probe at a velocity higher than 100 $\frac{steps}{s}$ causes an error on the final location of the probe to be in the order of 2–15 steps short from the desired total displacement.

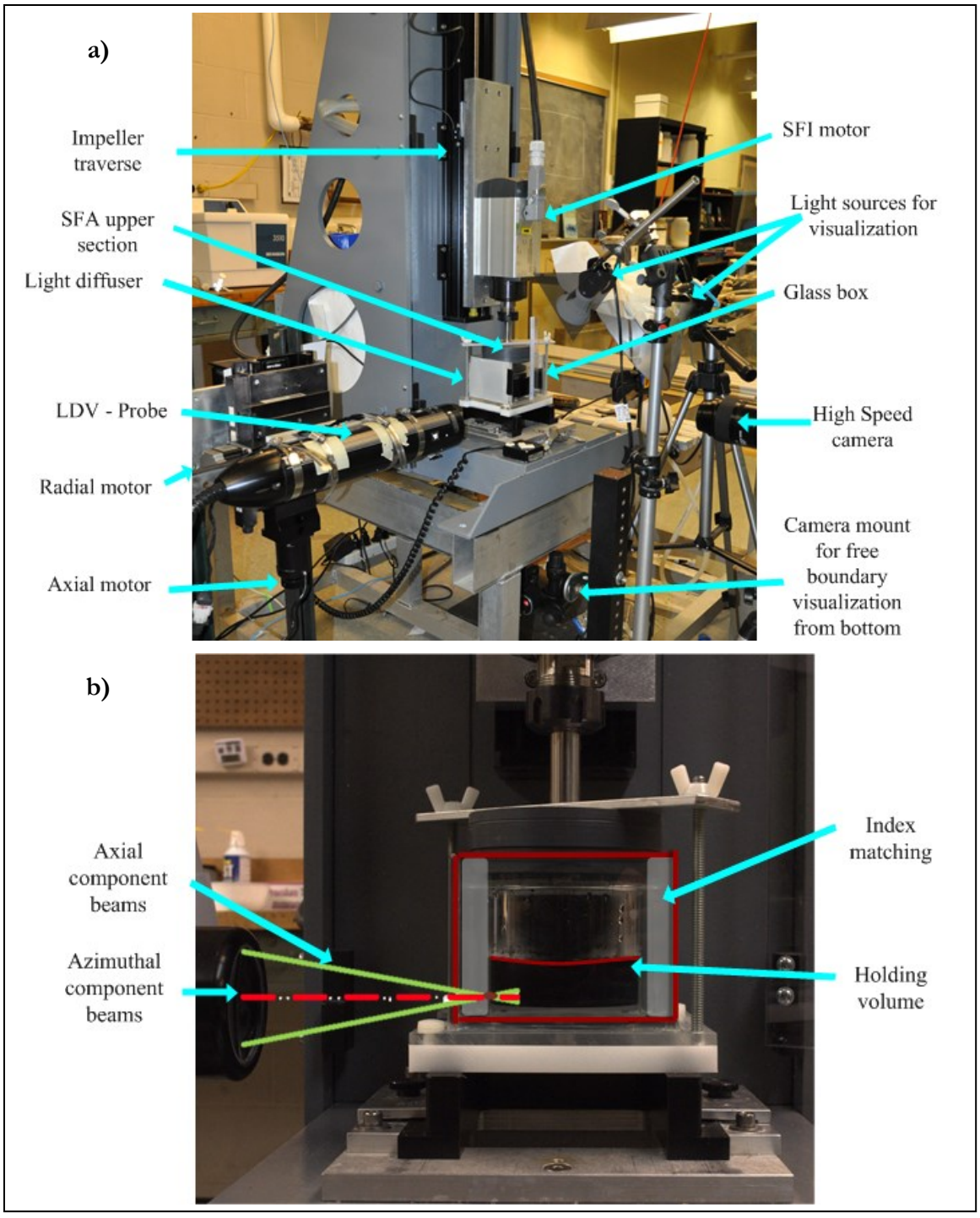

Figure 2.8. a) Set-up of LDV probe with traversing mechanism and initial arrangement for flow visualization of the SFA. b) Side view of LDV probe and location where beams cross to create volume. Also, shows where the liquid line lies at $0.54V_t$ in batch mode at rest (motor is off).

The LDV probe optical characteristics used for flow characterization are presented in Table 2.10.

Table 2.10. Optical variables related to the LDV measurement system.

Variable	Description	Value
D_b	Beam separation	50 mm
d_b	Beam diameter	2.65 mm
$\mathbf{f_L}$	Lens focal length	135 mm
$\boldsymbol{\kappa}$	Beam half angle = $\frac{\theta}{2}$ in air	10.75°
λ_1	Azimuthal component beam wavelength	514.5 nm
λ_2	Axial component beam wavelength	488 nm
θ_3	Half angle of the azimuthal component beams after the second curved interface.	8.05°

Calculations in Appendix A show the error caused by the curved surfaces (outer cylinder) on the incident angle for the beams measuring the azimuthal component. The calculated incident angle error for the measurement volume is ~0.6%. The fringe spacing for the measurement volume in water is calculated to be 1.8 μm and 1.7 μm for the azimuthal and axial components respectively. Moreover, the measurement volume used to measure the azimuthal component was 34 μm in diameter (at the waist) with length 241 μm. The azimuthal component measurement volume had a diameter of 32 μm at the waist, and 222 μm in length. The correction from the calculated error in the incident angle was applied for both measurement volumes.

2.3.1.1 Calibration of the position of the LDV measurement volume

While performing measurements, the LDV measurement volume was traversed radially and axially along the gap and bottom parts of the SFA. The measurement volumes were properly oriented by means of calibrating the angle of the probe. The procedures for setting the LDV probe are described as follows:

First, the SFA apparatus and the mounting system for the traversing mechanisms were leveled. To level the SFA apparatus, the height adjustable legs were set-up until no deviation from the horizon was observed on the bubble-level instrument. The traversing mechanism was leveled by using the 3 height adjustable legs of the mounts.

To align the LDV probe, a magnetic level is mounted above of the un-shifted axial beam. The level alignment plane is perpendicular to the axial beams as it sits on top of the probe, which is rotated until leveled. After the probe and the traversing mount were properly leveled, a calibration for the position in the radial plane was performed. This calibration was done by placing a calibration plate at the base of the SFA mounting platform.. The plate as seen in Appendix B. was placed accurately through reference points. The plate consists of a grid of points marking the centerline of the apparatus, also marking the inner and outer cylinder positions.

Once the plate was positioned, then the LDV system was turned on to show the beams of the azimuthal component (514 nm wavelength). The crossing beams were positioned at the mark of the outer cylinder, then the probe was traversed along the radial plane towards the center of the calibration plate (shifted and un-shifted beams are used). In this step the goal was to traverse the measurement volume along the centerline of the plate. If the measurement volume did not follow the centerline, then the mounting system for the traversing mechanism was repositioned to achieve this purpose. By following this calibration step we obtained accurate radial displacements of both measurement volumes.

Another calibration step was to ensure that the beams used to measure the axial velocity component were traversing in the vertical direction. Otherwise, the recorded velocity for this component will also register a velocity magnitude proportional to the deviation angle; causing an error on the measurement.

The axial alignment was performed by traversing the probe with a dial indicator using the impeller shaft as the reference frame. The SFA outer and inner cylinders are concentric and aligned were also aligned in reference to the shaft of the apparatus.

The indicator resolution was 0.0005 in (~12.7 μm). After calibrating the axial position, the probe deviated from the axial plane by +0.52° onto the azimuthal plane. This value is used as means to correct the angle bias measured by the axial velocity W_g through the experiments.

2.3.1.2 Location of the free boundary by LDV

The location of the free boundary at the bottom of the SFA was obtained both by visualization of images, and using the LDV system to estimate the interface location. The LDV measurement volume was traversed radially at a location near the observable liquid/air interface of the free boundary while observing the data rate of the particles in crossing the measurement volume.

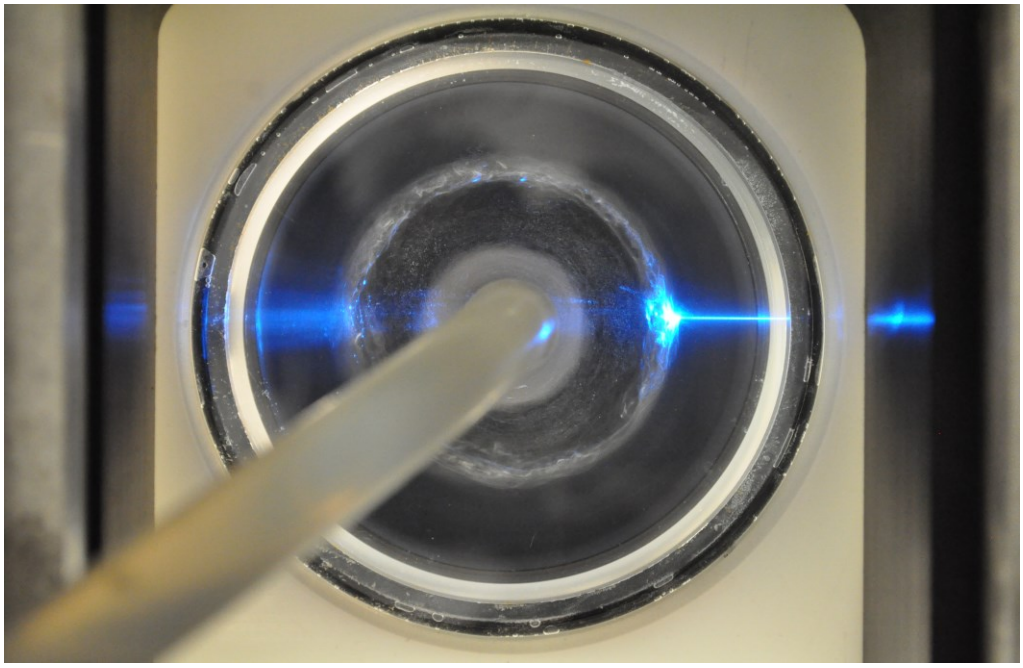

Figure 2.9. Bottom view of the SFA operating in continuous mode. The blue line entering at the right of the image represents one of the LDV beams (for the axial measurement volume)with the final position of the measurement volume located at the air/water interface

The location of the boundary was recorded as the point where the data rate of the particles dropped to the value of zero. This indicated that at this location the measurement volume was no longer in the fluid or at the interface. Figure 2.9 shows an

image of the free boundary location as it is mapped using the LDV beams. Observing the probe at the interface location one can distinguish a significant (unquantified) increase in random reflections caused by the oscillating interface. This simple visual inspection corroborated the aforementioned procedure.

2.3.2 Flow visualization

Single plane flow visualization was performed using high speed imaging with a non-collimated light source and Kalliroscopic particles, which have a flake type aspect ratio (specs in section 2.2.2). A high speed camera was oriented vertically aiming to obtain a large field of view encompassing the relevant flow zones.

In regards to the illumination field, two light emitting diode (L.E.D) bulbs emitting at 3500 K where used to illuminate the flow field. One of the bulbs was placed perpendicular to the camera lens next to the glass-box; the second bulb was placed above the camera with an angle of 36.5° as seen in Figure 2.10. The glass-box was covered with a liner of light diffusing fabric in order to reduce parasitic reflections. This type of configuration enhanced the contrast at the outermost locations of the field of view, and also created strong scattering at the axial center of the apparatus. Therefore, by using appropriate image processing techniques one could analyze the flow pattern in the SFA by observation of the finer structures at the axial center, and by focusing on the waveform of the instability at the edges of the field of view.

The purpose of using L.E.D lighting was to reduce the impact that radiative heat might have on the flow, as filament lights heat the fluid inside the SFA system, thus affecting the viscosity of the liquid.

Images were acquired with a Photron high speed camera; model *Fastcam-ultima APX (120 k)*. The camera has a maximum frame rate of 120 kHz. The system operates at full resolution up to a repetition rate of 2 kHz, above this benchmark the sensor resolution is reduced in order to achieve the desired frame rate. The camera head collects light onto a CMOS sensor array with 1024x1024 pixels, the pixel size is 17.5 μm; the data are relayed to a storage module until collection is required.

Table 2.11. Sensor resolution and frame rates used for data collection

Frame rate [Hz]	Resolution (WxH)	Recorded images (max)	Acquisition time [s]
1000	1024x1024	2048	2.05
2000	1024x1024	2048	1.02
3000	512x1024	4096	1.37
4000	1024x512	4096	1.02
6000	512x512	8192	1.37
8000	1024x256	8192	1.02

Table 2.11 shows the various frame rates that were used to obtain the images used for both PIV and flow visualization. Each frame rate corresponds to a sensor resolution, acquired images and total acquisition time. At maximum resolution, the field of view using a Nikon Nikkor 105 mm lens was 6 cm x 6 cm (WxH).

Table 2.12. Conditions at which flow visualization was performed with Kalliroscope particles.

U_0	Re_0	Camera frame rate [Hz]	Particle displacement between frames [mm]
3.5	1110	1000	3.50
3.5	1110	2000	1.75
7	2230	2000	3.50
7	2230	3000	2.33
10	3180	4000	2.50
20	6360	6000	3.33

Moreover, in flow visualization the tip speed of the impeller was used to calculate the estimated displacement of the particles between frames as shown in Table 2.12, column 4.

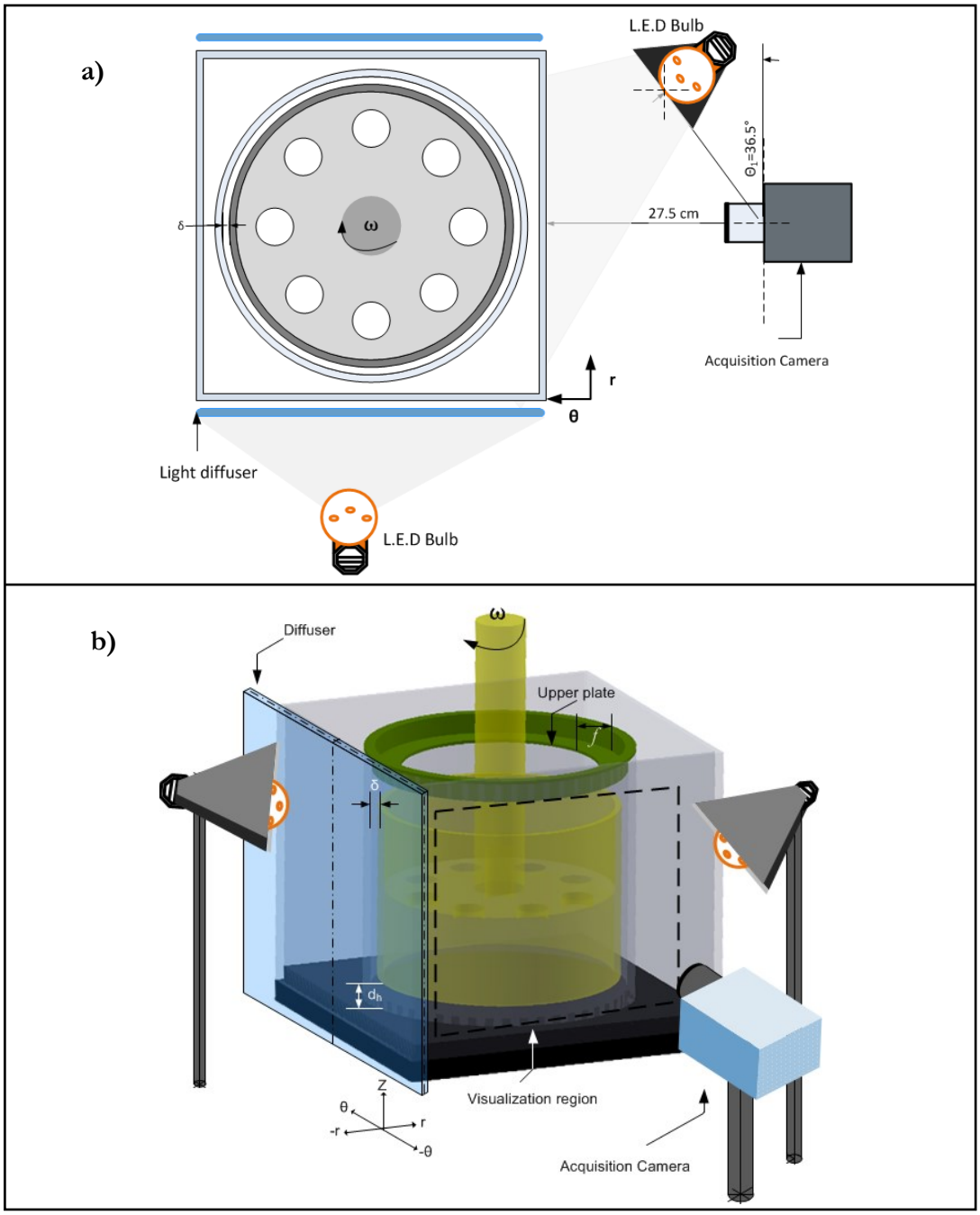

Figure 2.10. Shows the schematics of the SFA from two vantage locations. a) Top view with camera position and illumination equipment. b) isometric projection of the SFA with camera and illumination equipment. The drawings do not show the upper section allows seeing the upper plate. It shows a translucent inner cylinder (yellow) with attached shaft and transversal holes.

Flow visualization using Kalliroscopic particles was conducted by placing the high speed camera in front of one of the flat surfaces of the glass box as shown in Figure 2.10. The measurements were performed at various U_0. The camera shutter speed was adjusted accordingly as seen in Table 2.12. Moreover, for each azimuthal speed, the SFA motor was ramped from zero speed to the specified velocity.

Obtaining the locations of the free boundary and its position at various experimental conditions was performed in tandem using the LDV system. The characterization of the lower boundary was performed at the bottom of the apparatus while the camera was oriented towards the impeller. The camera used for these observations was a Nikon d5000 with a DX-VR 18-55 mm lens, having f-stop values of $f^{\#}$ 3.5-5.6. In Figure 2.9 one can observe an image obtained used to characterize the location of the free boundary.

2.3.3 Planar PIV

The velocity field calculation technique known as Particle Image Velocimetry (PIV) is part of a larger set of techniques that track motion in specific zones in the flow, using computer vision tools to obtain information on the spatial location of flow tracers, and their rate of change in time. The method hereby discussed is a sub-set of the general PIV technique by which vector velocities on a two dimensional plane are computed. This method focuses on finding the displacement (Δx, Δy) of various flow tracers between known time intervals Δt.

The flow tracer particles are illuminated by a pulsed laser sheet that resembles a plane. On the sheet plane consecutive images are captured by a high speed camera, the particle displacements are later determined from these images. This technique is therefore a non-intrusive flow characterization method, permitting to obtain instantaneous planar fields of velocity vectors.

The method using a high speed camera coupled with a high repetition rate laser system allows computing a sequential series of vector fields as means of addressing the location of unique patterns on the flow field. Therefore, by knowing the shutter frequency and the dimensions of the field of view the rate of displacement is known.

Tracer particles are illuminated as a result of manipulating a collimated light source using light sheet forming optics. The basic optic configuration usually consists of coated mirrors to direct the beam, a cylindrical lens to expand the beam into a sheet and a spherical lens to increase the light intensity at the desired acquisition location.

The computation of the vector field using this type of PIV technique is performed using single exposure dual-frame cross-correlations where an acquired image is segmented in a square grid fashion; inside each grid domain of $m \times n$ pixels a group of particles is found. Each grid domain is called a interrogation window (W_1 at t_1; W_2 at t_2); within this window, a cross-correlation algorithm is implemented. The correlation is applied between the two adjacent time frames (t_1,t_2) for each interrogation window (W_i). In short, this step is performed using the intensity peaks on the images according to their histograms. Therefore, the algorithm evaluates the pixel displacement of particles in each interrogation window between two images in a sequence. The cross-correlation of each interrogation window for dual frame recordings can be computed in the following way.

$$R_{I_1,I_2}(\Delta X, \Delta Y) = \iint_{t_1}^{t_2} I_1(X,Y) I_2(X+\Delta X, Y+\Delta Y) dX dY,$$

where I_1 is the intensity at frame 1, and I_2 is the intensity at a point shifted by $(\Delta X, \Delta Y)$ in the second frame at interrogation window W_2. This is the cross correlation of the image intensities in W_1 and W_2. Moreover, it is common to apply a Gaussian fit to the correlation peak to obtain the sub-pixel displacement. The final pixel displacement for a given interrogation window is then the displacement of the applied fit. The appropriate discussions on algorithms used to obtain the displacement of the interrogation domain, and other computational requirements are thoroughly shown in (Adrian, Westerweel 2011).

2.3.3.1 Laser, optics and timing

The experiments performed and shown in this work are a result of operating a single plane PIV set-up similar to Wereley, Lueptow 1998. The set-up consists of a similar high speed camera used in the flow visualization section (2.3.2), a high repetition rate Nd-YLF

laser of 30 $\frac{mJ}{pulse}$ (Photonics, DM-30, 527 nm wavelength) and the respective laser sheet optics. Acquisition of images is performed using both the Photron in house software and the high speed module from LaVision using DaVis software.

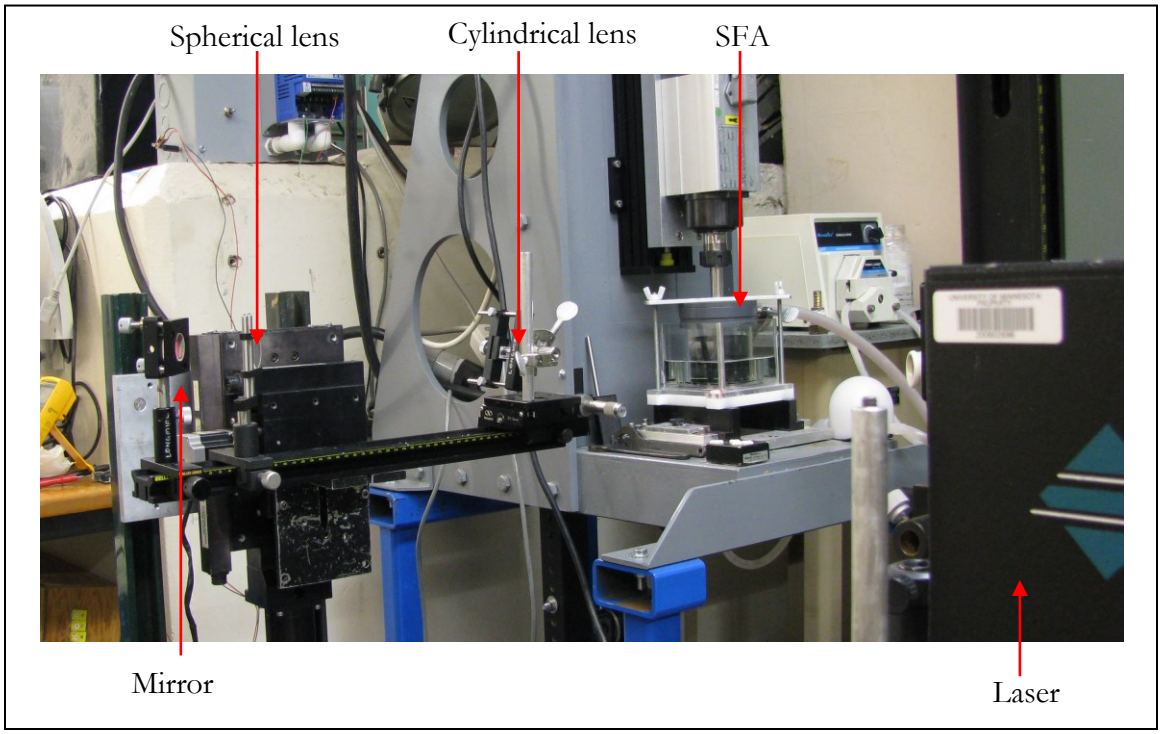

Figure 2.11. Experimental set-up for planar PIV and particle tracking showing the laser head, optics and SFA apparatus.

Figure 2.11 shows the experimental set-up used for single plane PIV. The optics used to generate the laser sheet are mounted on an optical rail system attached to traversing mechanism previously described in Section 2.3.1 used to traverse the LDV probe. The optics consist of 1 mirror to redirect the laser beam, 1 spherical lens of 1000 mm focal length, and one cylindrical lens with 300 mm focal length. The spherical lens is used to focus the beam and increase the intensity, while the cylindrical lens expands the laser beam into a plane. The laser sheet had a thickness of ~3 mm, for measurements at Re_0 of 1110 and 2230. The laser sheet is generated according to $\frac{|U_i|\Delta t}{\Delta Z_o}$ <0.25, where $|U_i|$ is the out of plane velocity, Δt time between pulses (in this case, between image frames) and ΔZ_o is the sheet thickness (Adrian, Westerweel 2011).

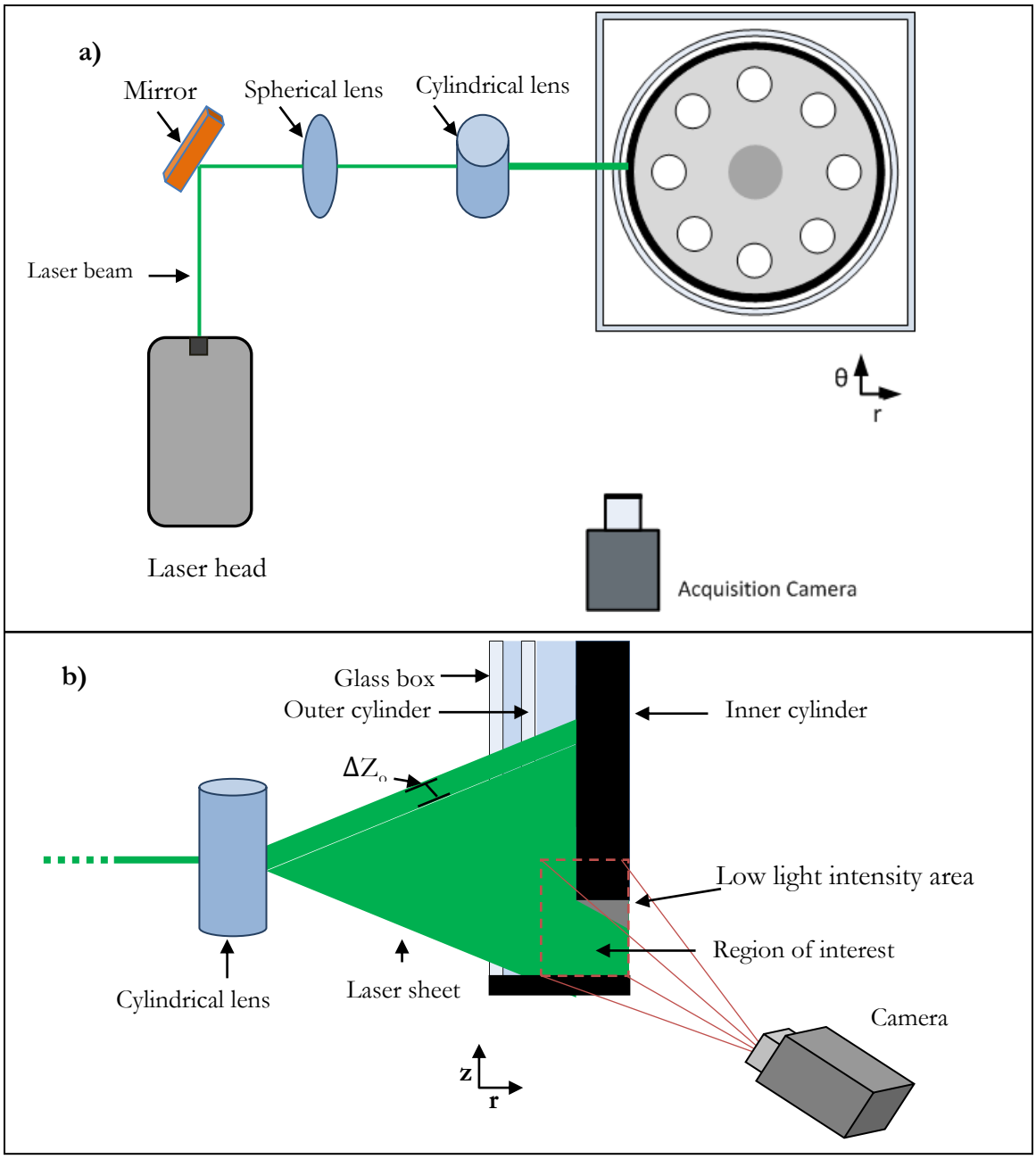

Figure 2.12. Pictorial diagram of the PIV and PTV set-up. a) Top view of the PIV showing laser head, optics and radial cross section of the SFA. b) Expanded view showing an example of the laser sheet illuminating the bottom of the apparatus.

Figure 2.12a shows a simplified view of the PIV set-up. The camera was placed off-axis from the centerline, such that the radial-axial plane is imaged as shown in Figure 2.12b. In Figure 2.12b the laser sheet

Table 2.13. Shows the acquisition set-up for the high speed camera based on Re_θ. In addition the table shows various laser sheet thickness and out of plane velocity ratios for the camera set-up.

Re_θ	Camera frame rate [Hz]	ΔZ_o [mm]	$\frac{\lvert U_i \rvert \Delta t}{\Delta Z_o}$
1110	2000	3	0.30
1110	3000	3	0.20
2230	3000	3.5	0.33
2230	4000	3.5	0.25

The out of plane velocity U_i used to calculate the velocity ratio in Table 2.13 is 50% of the tip velocity U_0 at the given Re_0. The value of U_i was obtained after analyzing LDV data for measured azimuthal speeds in the gap, where the average velocity drops to $0.5U_0$ at a radial distance of 0.2δ (400 μm) from the impeller consistently for both Re_θ (1110 and 2230). For the various values U_i it was found through tests that the out of plane velocity was not impeding with the cross-correlation of images. It was then determined that the laser sheet thicknesses shown in Table 2.13 were sufficient to perform PIV and particle tracking.

Figure 2.13 shows the timing diagram for the laser, and Photron camera controlled by the high speed controller. The laser is triggered 7 μs after the camera.

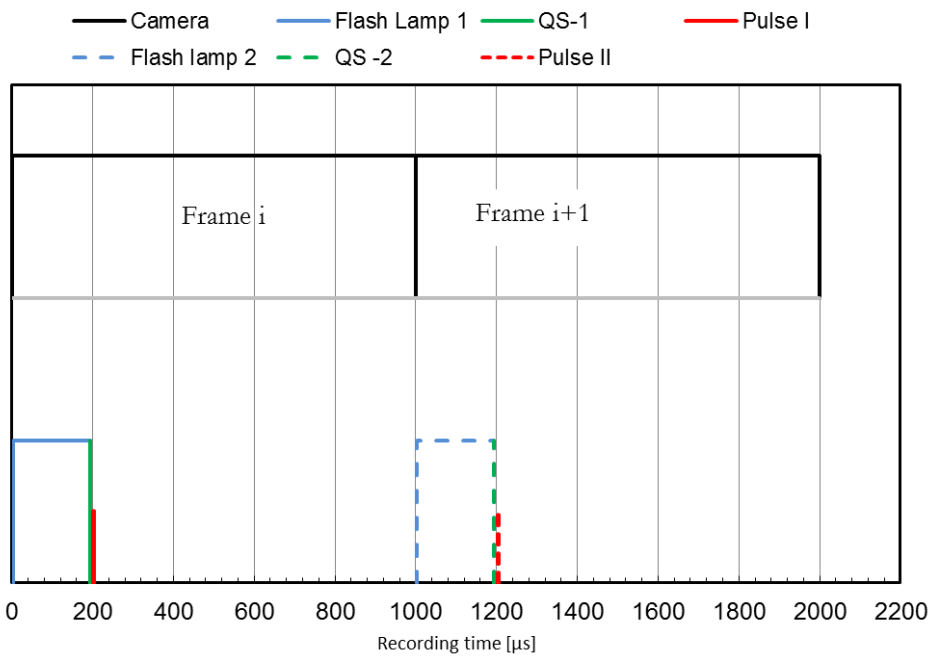

Figure 2.13 Sample of the timing diagram for the first two frames of one acquisition sequence at a frame rate of 1000 Hz. Acronym QS stands for Q-switch.

Chapter 3

Experimental uncertainty

3.1. Dynamic conditions

3.1.1 Reynolds number uncertainty

The uncertainty on the rotational Reynolds number depends on the tip speed of the inner cylinder, the thickness of the gap and the viscosity of the fluid.

The rotational speed of the inner cylinder was calibrated using a stroboscopic light with a resolution of 0.1 Hz, or ~0.024 m/s when transformed into the rotational frame of reference for the impeller. The maximum measured standard deviation for the tip speed of the inner cylinder occurs at a speed of 20 m/s with a value $\sigma_{U_\theta}=0.48\frac{m}{s}$.

Figure 3.1 shows the uncertainty in the tip speed is found to be at a maximum of 0.06 m/s based on $\delta U_\theta=\frac{\sigma_{U_\theta}1.96}{\sqrt{N}}$. In the equation, σ_{U_θ} corresponds to the standard deviation, and N number of samples. The maximum value of the uncertainty of the azimuthal velocity translates to an uncertainty in the rotational speed of $\delta\omega=0.25\frac{rad}{s}$

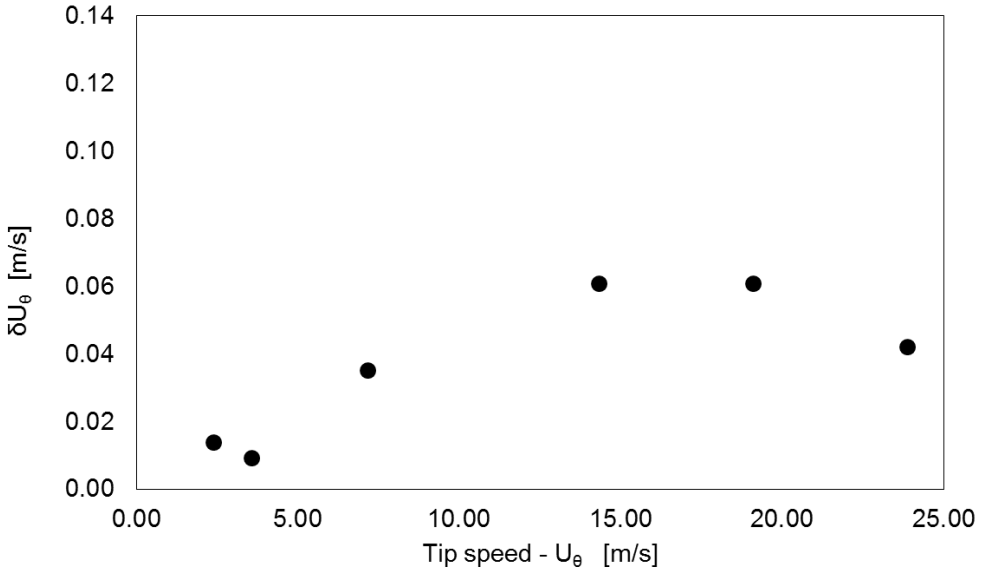

Figure 3.1. Uncertainty in the rotational speed of the impeller based on the required velocity U_θ

In steady state operation, the rotation of the inner cylinder imposes work on the fluid. The mechanical work applied by the impeller raises the internal energy of the fluid (water in this case), is dissipated as excess heat.

The baseline reference operating mode was room a temperature of 22°C ± 2°C. It was mentioned in Section 2.15 that the increase in temperature of the fluid could reach a maximum of 20°C above the baseline, decreasing the liquid viscosity. For that reason, a heat exchanger was used to decrease the effect in temperature change of the working fluid. The relationship of the viscosity to temperature for the baseline, and its deviation is well defined in literature; see Batchelor, 1967.

In steady state operation using the temperature control loop, the mean temperature of the liquid within the SFA was measured at 19.4°C, and the calculated uncertainty in the temperature of the liquid was found to be δTemp=1.23°C. Therefore, the uncertainty for the kinematic viscosity of the fluid was 0.994×10^{-6} $m^2s^{-1}\pm0.064\times10^{-6}$ m^2s^{-1}.

The uncertainty in the thickness of the gap is related to the precision in the machining process. The uncertainty in thickness of the gap is obtained by combining the uncertainties for both cylinders.

$$\frac{\delta gap}{gap}=\left\{\left(\frac{\delta r_i}{r_i}\right)^2+\left(\frac{\delta r_o}{r_o}\right)^2\right\}^{\frac{1}{2}}$$

Using this method, the uncertainty in the gap was calculated to be 0.2% of the gap thickness.

The propagation of the uncertainty for the Reynolds number is calculated assuming the maximum error in the azimuthal velocity which occurs at the tip speed of 20 m/s. Moreover, to obtain the uncertainty in the value of the Reynolds number, the calculated uncertainties for the azimuthal velocity, viscosity and gap thickness are combined in the following way:

$$\frac{\delta Re_\theta}{Re_\theta}=\left\{\left(\frac{\delta U_\theta}{U_\theta}\right)^2+\left(\frac{\delta \nu}{\nu}\right)^2+\left(\frac{\delta gap}{gap}\right)^2\right\}^{\frac{1}{2}}$$

For the calculation of the error in Reynolds number, δU_θ corresponds to the uncertainty in the tip speed, $\delta\nu$ is to the kinematic viscosity and δgap to the uncertainty in the gap thickness. Using the maximum error for the azimuthal velocity, the uncertainty in the Reynolds number is 6.4%.

3.1.2 Axial through flow

The uncertainty in the axial through flow is mainly dependent on the volumetric flow rate of the Masterflex pump discussed in section 2.1.4. The pump has a maximum output of 30 mL/s that corresponds to an axial velocity of 0.061 m/s. It was found that the maximum uncertainty for the volumetric flow rate occurs at 30 mL/s with an uncertainty $\delta\dot{Q}=0.4\frac{mL}{s}$ as shown in Figure 3.2.

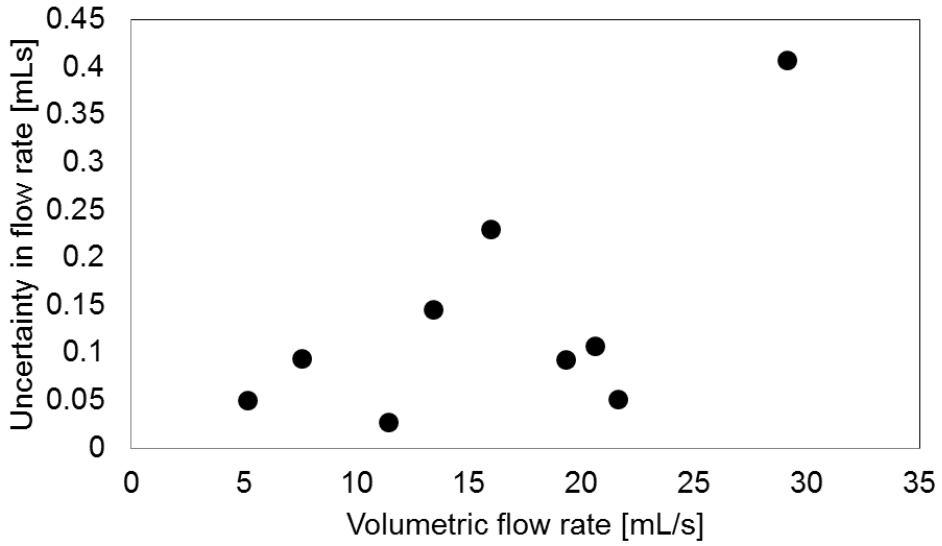

Figure 3.2. Calculated uncertainty in the volumetric flow rate $\dot{Q}\left[\frac{mL}{s}\right]$

Is is shown through Figure 3.2 that the deviation from the values in axial flow are almost negligible compared to the impeller tip speed even at the smallest Reynolds number (Re_θ=1110). For example, the highest uncertainty in volumetric flow rate corresponds to an axial velocity of $W_g=8.3\times10^{-4}\frac{m}{s}$, which is 1.4% of the estimated velocity in the gap at this condition (0.06 m/s).

3.2. Laser Doppler Velocimetry

The major types of errors in LDV are velocity bias, filtering the signal, angle bias and gradient bias. In here we discuss the uncertainty in the measured velocity caused by the

arrival of particles at the measurement volume. For a probe that is stationary, the notion of velocity bias states that particles traveling at a higher speed will stamp a higher number of measurements per unit time when compared to slow moving particles. Therefore, the average of the velocity measurements for a given location will be skewed towards higher velocities.

It was found by Tiederman, 1973, that the magnitude of the velocity bias is proportional to the square of the local turbulent intensity. Here, we used a sampling method to correct for the velocity bias instead of post-processing. The data rates experienced while acquiring data at the gap ranged in average from 0.5 Hz near the wall up to 1600 Hz near the impeller. To account for this difference, near the wall-0.3δ, the data was sampled at a fixed rate to eliminate the velocity bias. The sampling rate was 10 Hz, later as the data rate increased the sampling time between two measurements was changed to 100 Hz. At the given sampling rates it was desired to acquire 3000 independent samples as means of reducing the velocity bias.

For 3000 independent samples at Re_θ=2230 in batch condition, the uncertainty in the measured azimuthal velocity was $\frac{1.96\sigma}{\sqrt{N}} = 2.6\times10^{-4}\frac{m}{s}$, where σ is the root mean square value of one data set consisting of N samples. The upper bound for the standard error on LDV measurements of the azimuthal component with 95% confidence interval is calculated to be 0.00153 m/s. The minimum standard error seen in these measurements is in the order of 5.1×10^{-4} m/s on the lower bound. The uncertainty in the root mean square velocity (RMS) for the same Reynolds number was found to be $4.12\times10^{-3}\frac{m}{s}$, which corresponds to 1% of the measured RMS at 0.6δ in the gap.

The errors caused by the probe location and angle are discussed in Chapter 2. However, it is difficult to quantify other errors such as filtering and gradient bias. The latter corresponds to the size of the length of the measurement volume. Since the particles passing at one location might be traveling at a different speed than others moving at one of the extremes of the volume. This will also skew the average measurement of the velocity at one location. We have approached this problem by reducing the size of the

measurement volume to 0.1δ (gap size). To reduce the error of filter bias we use FIND software to downshift the frequency at values that lie between the expected velocities at the gap. For example, it is known that near the stationary wall and the impeller the azimuthal velocity will be 0 m/s and ~U_θ respectively. Therefore appropriate downshifting was used in the range of 35 -39.5 MHz to accommodate for the expected velocities. Moreover, the signal was treated by a band pass filter (using FIND), with a filter setting at 1-10 MHz. It was found that the filtering at these frequencies was appropriate considering the limits of the processor and the expected velocities.

3.3. Single Plane PIV

In single plane (planar) PIV the random uncertainty can be approximated by using the magnification of the measurement (M_o), the uncertainty in the displacement of particles ($\sigma_{\Delta r}$) and the time between images (Δt) which is given by the camera frame rate (Adrian and Westerweel, 2011).

$$\delta u = \frac{\sigma_{\Delta r}}{M_o \Delta t}$$

The random uncertainty in planar PIV can be approximated by $\sigma_{\Delta r} = \sigma_{\Delta z}$ to be 0.1 pixels. It was found that the magnification for the images to be 0.0295 mm/pixel. The highest uncertainty in the velocity was calculated to be 0.15% of the tip speed; this is for cases acquired at 3000 frames per second and 3.5 m/s of tip speed.

Chapter 4 - Averaged Flow Behavior

Results and Discussion: Flow statistics, free boundary

The characterization of the flow field in the SFA is focused towards understanding the flow physics at two operating conditions: Re_θ =1110 and Re_θ= 2230. Previous experiments performed by Andereck show in Figure 1.8 the mapping of various distinct flow regimes at said Reynolds numbers. From these experiments it is expected to observe wavy vortex flow and nominally turbulent Taylor vortices at these two Re_θ conditions.

Table 2.6 shows the configurations of upper plates used to alter the thickness of the free boundary as means of matching the continuous conditions to the batch condition. The most studied flow rates [$\dot{Q}$] are 10, 20 and 30 $\frac{mL}{s}$ which translate to gap residence times (t_g) of 2.8s, 1.3s and 0.9s respectively. These experimental conditions correspond to the mean axial velocities at the gap of W_g=0.02 $\frac{m}{s}$, 0.04 $\frac{m}{s}$ and 0.061 $\frac{m}{s}$ respectively.

Moreover, as noted in Table 2.6 and explained in section 1.2.2 the SFA in continuous operation is fitted with the upper plate (f_s) as means of controlling the thickness of the spinning film (free boundary). Herein we discuss the effect and relationship of the upper plate on axial through flow and the impact it has on the location of the free boundary.

4.1. Topology of the free surface

In the following sections the response of the free boundary to experimental conditions such as the upper plate thickness, axial through flow and their interaction is discussed. Moreover, the response of the boundary to Reynolds number is also studied.

First, in Figure 4.1, the response of the free boundary in batch condition $\left(W_g=0\frac{m}{s}\right)$ is seen for two values of Reynolds number. In Figure 4.1a the boundary is developed, meaning it intersects the bottom surface of the apparatus. The location where the boundary touches the bottom surface of the apparatus is evident by the observable halo on the surface.

At smaller radius (towards the center of the apparatus), droplets of liquid resting on the surface are observable; they are surrounded by air. However, in Figure 4.1b, the contrasting difference between the liquid and air across the edge of the spinning film is not so well defined. In this scenario, it is said that the free boundary is not developed, since it is not extending to the bottom surface of the apparatus. In both images the system has achieved steady state.

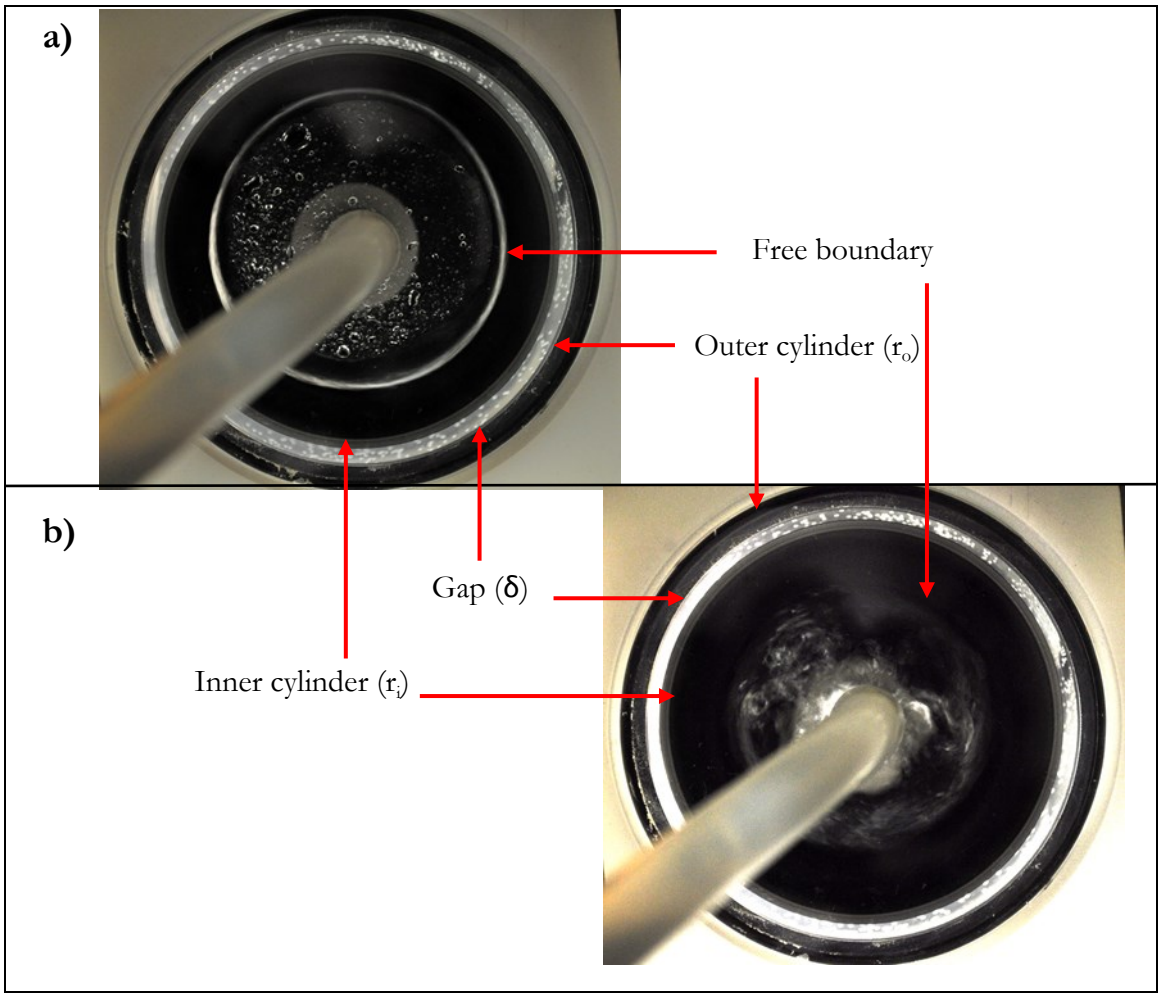

Figure 4.1. View from bottom of the free boundary for a) fully developed boundary at $Re_\theta = 2230$, $W_g = 0$ m/s. b) Undeveloped boundary at $Re_\theta = 1110$, $W_g = 0$ m/s.

4.1.1 Batch condition – Constant Reynolds number

To obtain the location of the free boundary under various conditions, a combined effort for visualizing the position of the interface coupled with the LDV based location is implemented. The location of the boundary is recorded at the position where the LDV probe records no data rate. This location is also visualized from underneath of the SFA as discussed in section 2.11.

Figure 4.2 shows the theoretical, interface locations values for each holding volume. The theoretical locations do not include the displaced volume by the impeller, which is $0.06V_T$.

This volume would displace the theoretical position of the boundary by 0.5δ in the radial direction. Figure 4.2 contains data relevant to the size and location of the spinning films in regard to the gap and impeller. The lowest part of the impeller is located at 2.5δ above the bottom of the apparatus, which equals to 1.0 h_L. In the same figure, the uppermost point of the impeller is situated at z=27.5δ

Figure 4.2 shows results at Re_θ = 2040 where the free boundary transitions from undeveloped to fully formed as holding volume is increased. At holding volumes $0.3V_T$ and $0.42V_T$, the free boundary does not reach the bottom surface of the vessel. For the unformed free boundaries, the observed positions move outwards radially (larger $\frac{r}{\delta}$) as $\frac{z}{\delta}$ is increased. The free boundary in the $0.3V_T$ holding volume case, stops moving outward radially at a height of ~1.5δ and radial position ~16δ. Beyond these coordinates, the interface maintains a constant radial position. The condition of $0.42V_T$ on the other hand, is seen to reach the estimated boundary position at a height of 2.5δ.

For the largest holding volume shown, the film is fully formed at the given Re_θ. At this condition ($0.54V_T$), the final radial position of the free boundary has a smaller variation from the initial recorded location (at the smallest $\frac{z}{\delta}$) than the other holding volumes. Specifically, for $0.3\ V_T$ the separation from the theoretical boundary location (dashed lines) is about 2δ from the smallest $\frac{z}{\delta}$, for $0.42\ V_T$ separation is in the range of 2.5δ and for the largest holding volume the separation is 1.5δ.

For measurements closer to the impeller $\frac{z}{\delta}$~2.5 for a given Reynolds number, it is seen that the free boundary location approaches the theoretical position as holding volume is increased. Moreover, it is observed that as the holding volume within the SFA is increased, the free boundary reaches the bottom surface of the apparatus.

a)

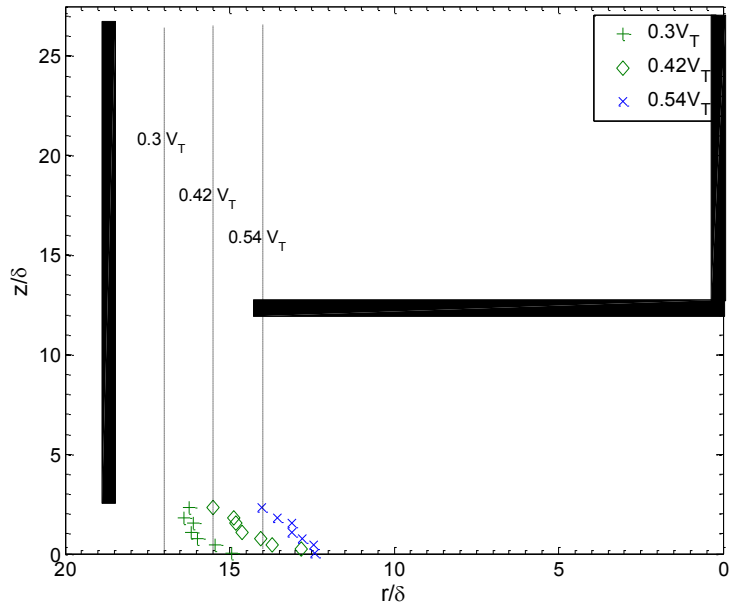

b)

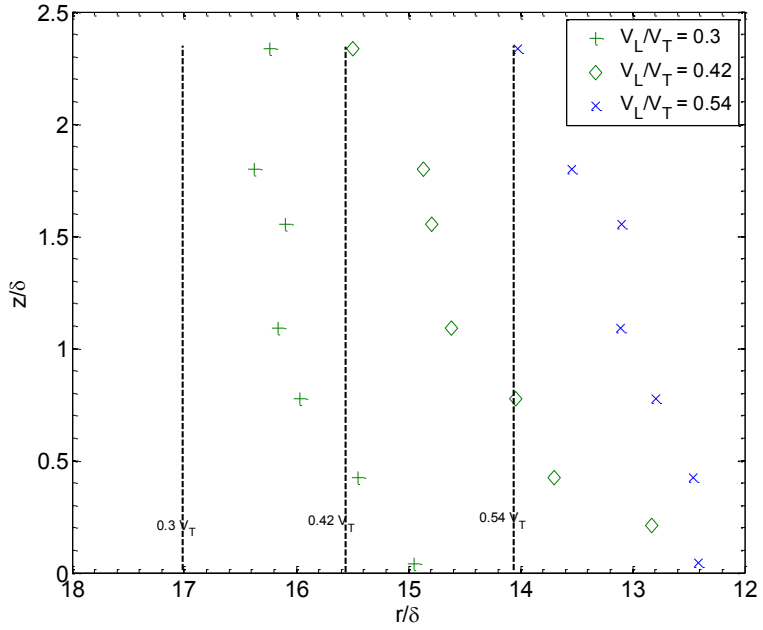

Figure 4.2. Location of the boundary for various holding volumes at Re_θ=2040 in batch condition W_g= 0 m/s. a) Cross sectional view of the impeller with superimposed free boundary locations at $0.3V_T$, $0.42V_T$ and $0.54V_T$. b) Expanded view on the displacement of the free boundary caused by various holding volumes. Blue marker represent a spinning film fully developed, green markers are for free boundaries not fully formed. Marker (+) is for $0.3V_T$, (◊) for $0.42V_T$ and (x) for $0.54V_T$.

4.1.2 Batch condition – Variable Reynolds number

In the batch condition, where $W_g = 0$ m/s and the value of $f_{sj} >> \delta$ (19δ) the spinning film does not rise above the height at which the upper plate is located. Therefore, the whole of the holding volume is contained within the outer and inner cylinders. Previously it was observed that a fully developed boundary is achievable by increasing the holding volume within the apparatus. Now, the effect of varying the rotation rate of the inner cylinder is evaluated. The Reynolds number increases as the rate of rotation of the inner cylinder is increased.

In both plots in Figure 4.3, (0.3 V_T and 0.42 V_T) the data point at the smallest $\frac{z}{\delta}$ position indicates the approximate thickness of the liquid film just above the bottom surface of the SFA. Figure 4.3a, showing data for holding volume of $0.3V_T$ displays that for Reynolds values equal or less than 2228 the boundary does not intersect with the bottom of the apparatus (not fully developed). For the same plot the free boundary formed for values of Re_0=2546 and above. For the fully developed conditions, the boundary seems to moves outward as $\frac{z}{\delta}$ is increased from 0 to up to ~1. From the latter position, the radial location remains to be constant up to $\frac{z}{\delta}$~1.5 and is found to be the nearest to the predicted value. Then, the interface is observed to shift inwards radially as $\frac{z}{\delta}$ is increased up to the last observable position near 2.5 which is just below the impeller base.

The required Reynolds number to achieve a fully developed boundary for $0.42V_T$ is 28% smaller than for $0.3V_T$. In Figure 4.3b the theoretical location of the boundary is calculated to occur at a radius of 15.5δ. It is seen that the radial positions for this holding volume extend to the region near 16δ for the developed profiles. The values of the measured location of the film surpass the calculated location when $\frac{z}{\delta}$>0.5.

a)

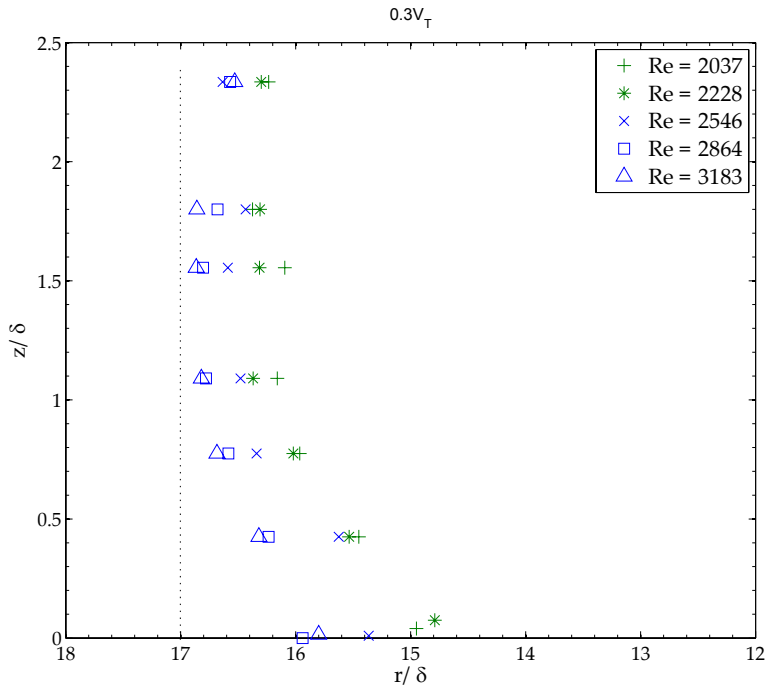

b)

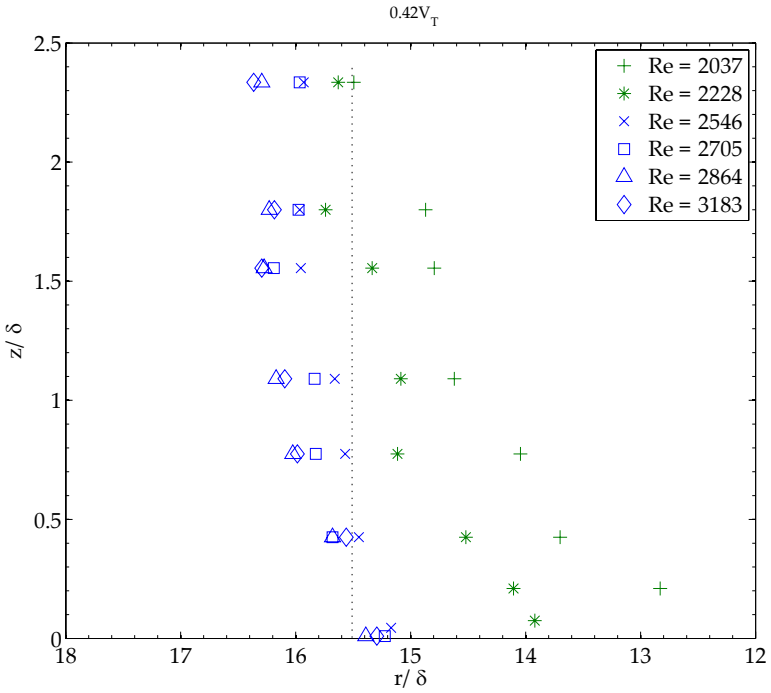

Figure 4.3. Mapping of the location of the free boundary at various Reynolds number and W_g = 0 m/s (batch condition). a) Holding volume of $0.3V_T$, the vertical line at 17δ is the theoretical position of the boundary. b) Holding volume of $0.42V_T$, the theoretical position is found at 15.5δ. Green markers represent films not ending at the bottom of apparatus.

All developed spinning films in Figure 4.3b initiate at position $\left(\frac{r}{\delta} = 15.3, \frac{z}{\delta} = 0\right)$. At those dynamic conditions, the boundaries collapse near the theoretical position at $\frac{r}{\delta} = 15.5$, although the interface moves outwards as the value of $\frac{z}{\delta}$ is increased. A behavior slightly different is observed in Figure 4.3a ($0.3V_T$) as previously discussed, where the free boundary eventually moves inwards (reduced radial position) as $\frac{z}{\delta}$ increases.

4.1.3 Continuous flow condition

Unlike in batch operation, the liquid volume fraction is unknown inside of the apparatus. One assumption is that the liquid forms a spinning film of similar shape to batch condition. It is thought that the liquid volume fraction corresponds with an annulus starting at the outer wall and with a width f_s.

In these conditions, an axial flow is imposed by introducing liquid into the SFA through the inlet port at the bottom of the apparatus. The fluid exits the apparatus by climbing over the upper plate and eventually finding its way through the outlet port. The effect of the outlet port is not considered in mapping the free boundary through the techniques discussed in this chapter. Yet, the response of the free boundary to various upper plate thicknesses is evaluated, specifically for the conditions of f_s = 6 mm and 9 mm, which correspond to nominally $0.3V_T$ and $0.42V_T$ in the batch case.

For Figure 4.4 the position of the spinning film was recorded for a single upper plate f_s=9 mm varying the rotational Reynolds number (Re_θ). The lowermost radial position of the interface is plotted as a function of Re_θ for three values of $\dot{Q}$, having a nominal volume fraction of $0.42V_T$. These correspond to W_g = 0.020 $\frac{m}{s}$, and 0.061 $\frac{m}{s}$.

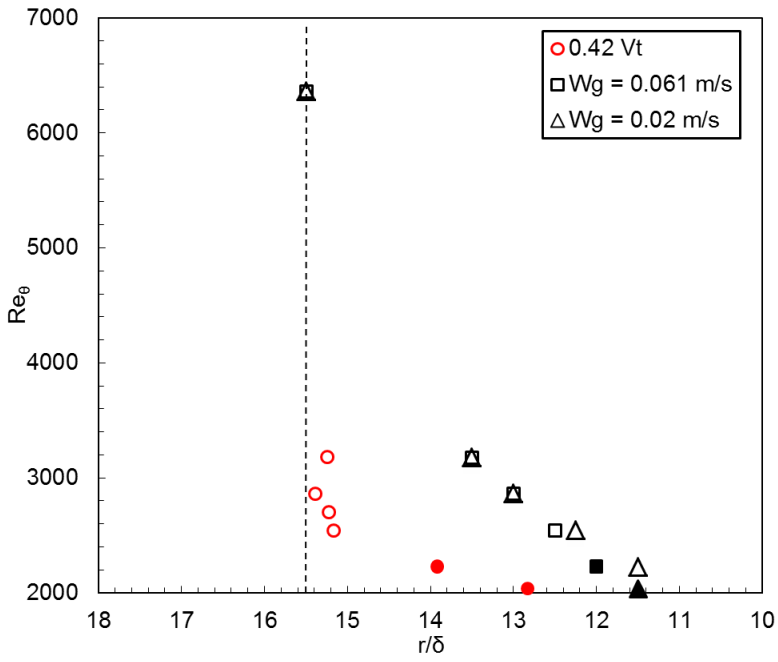

Figure 4.4. Free boundary location near z=0 for f_s = 9mm, equivalent to batch case 0.42V_T. The red circles (○) are batch results at 0.42 V_T. (□) represent t_g=0.9 s and W_g= 0.06 m/s. (◊) for t_g =2.8 s, and W_g= 0.02 m/s. All filled markers represent boundaries not developed.

Data for the larger axial velocity shows undeveloped boundary points at similar Reynolds number as in batch condition. However for Re_0= 2028, the recorded radial position is displaced inward by 1.9 δ from the batch case. A similar behavior is observed for W_g=0.02 $\frac{m}{s}$, where the inward radial displacement is 1.5δ.

With axial flow present, the radial position of the film collapses for values above Re_0>2870. In these conditions, it is clear that one constraint for the spinning film to be fully developed is the need of higher azimuthal velocities. In the case of batch condition with no axial through flow, the boundary is established and appears to reach the theoretical position at Re_0≈2545. With axial flow, however, the film is located at ~2.7δ inward for equal Reynolds numbers as in the batch case.

At higher Re_0, the base of the interface moves to the location predicted when the fluid volume is 0.42V_T and the interior fluid takes the shape of an annulus with width f_s=9mm. The two cases with axial throughflow both converge at this location at Re_0= 6500. Most

importantly, the addition of axial throughflow appears to delay the development of the annular shape of the boundary to a significantly higher Reynolds number, at least in the zone beneath the impeller. This is true even though the axial flow velocity in the gap is almost 1% of the azimuthal speed.

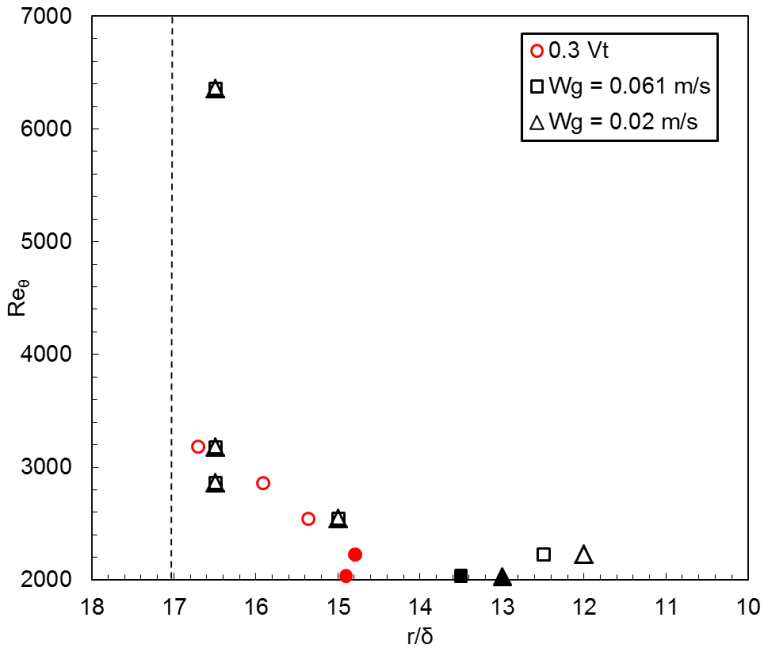

Figure 4.5. Free boundary location near z=0, for f_s = 6mm, equivalent to batch case 0.3V_T. The red circles (○) are batch results at 0.42 VT, squares (□) represent t_g=0.9 s and diamonds (◊) for t_g =2.8 s. All filled markers represent boundaries not developed.

Figure 4.5 shows the lowermost radial point of the boundary as a function of Reynolds number. The imposed axial flow velocities are similar as in Figure 4.4. The plot shows that undeveloped free boundaries are found at the lowest Reynolds number for the cases with axial flow. It is seen that in the throughflow cases both data sets display their first developed point at a higher Reynolds number and a smaller $\frac{r}{\delta}$ compared to the undeveloped boundary point.

The plot shows that by increasing Re_0 the location of the free boundary approximates the predicted location for the conditions with axial flow. It also shows that for values greater than Re_0=2800 the radial position of the free boundary is about constant for both axial

flow rates. For the batch case in Figure 4.5, the data also approximates the theoretical film location at similar Reynolds number as in continuous flow. For this holding volume of $0.3V_T$ higher values of Re_θ are required to have the free boundary to approachthe calculated location when compared to Figure 4.4 with $0.42V_T$.

4.2. Averaged velocity statistics by LDV

In batch condition, the SFA operates similar to Taylor Couette apparatuses where the inner cylinder rotates while the outer is held stationary. The dynamics of the flow inside the space between the cylinders (gap) undergoes various changes as the speed of the inner cylinder is increased.

In this section, flow statistics are described based on the azimuthal and axial velocity components at various locations within the SFA. For these measurements the apparatus operated in batch mode. The axial location where data was collected is shown in Figure 4.6. The measurements were performed for two azimuthal tip speeds (U_θ) as shown in Table 4.1.

Table 4.1. Evaluated experimental set-up for the SFA in batch condition $W_g=0\frac{m}{s}$

$U_\theta \left[\frac{m}{s}\right]$	Re_θ
3.5	1110
7	2230

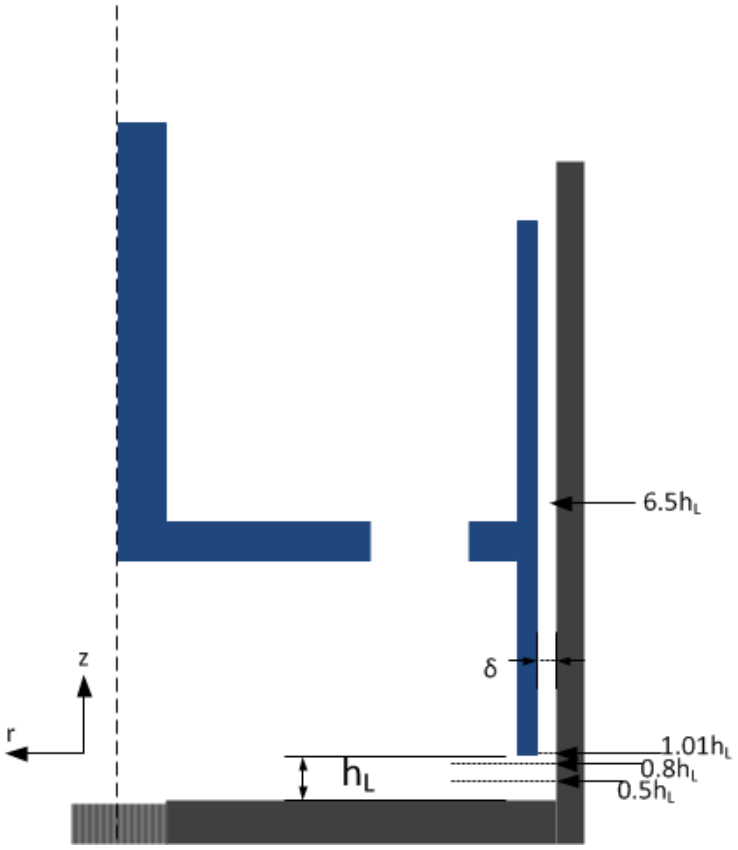

Figure 4.6. Pictorial cross section of the SFA showing locations based on the space between the impeller and the bottom of the apparatus. Variable δ represents the gap width with thickness 2 mm, and H_L the height between the impeller and the bottom of the apparatus.

Measurements were performed at multiple heights along the axial plane flow statistics were measured by traversing the LDV probe in the radial direction at the axial locations shown in Figure 4.6. For each point measurement both at the gap and underneath the impeller, two velocity components are measured. Instantaneous measurements are performed for the azimuthal (U_θ^i) and axial components (W_i^{gap}). Each variable is normalized and mean values are plotted as:

$$U_\theta^{mean} = \frac{1}{n}\sum_{i=1}^{n} U_\theta^i;\ U_\theta^* = \frac{U_\theta^{mean}}{U_\theta}$$

$$W_i^{mean} = \frac{1}{n}\sum_{i=1}^{n} W_i^{gap};\ W_i^* = \frac{W_i^{mean}}{U_\theta}$$

For flows that present instabilities above the value of Ta_{cr} (critical Taylor number) a characteristic signature in U_θ^i should be present as seen in Figure 4.7. Plotted is a sample data set for a point measurement at the center of the gap at height $6.5h_L$. The variable t^* is normalized by the total sample time (t_{max})

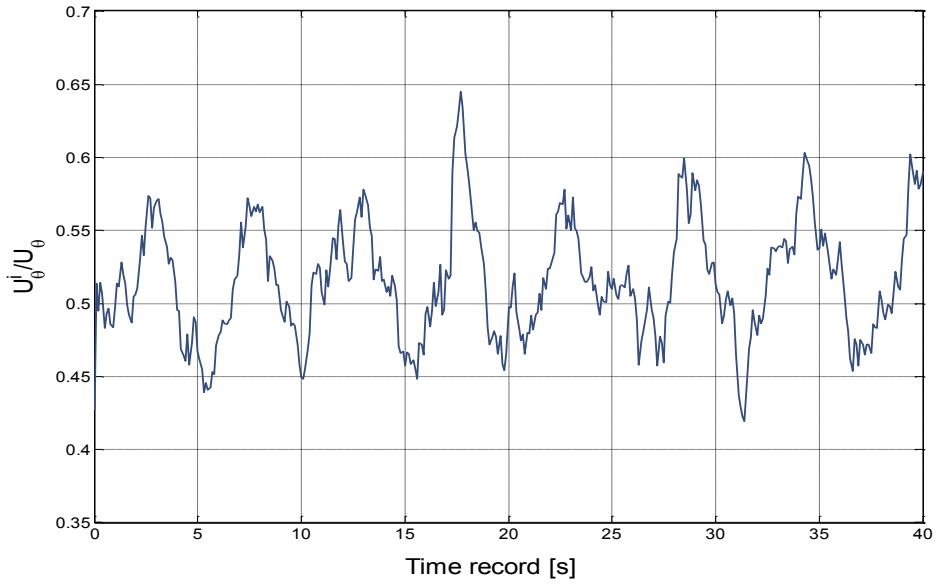

Figure 4.7. Point measurement of instantaneous data at Re_θ = 1110. The variable $U_\theta^i$is the acquired azimuthal velocity at a given point, and U_θ is the speed of the impeller. Data acquired at z=6.5h_L from the bottom of the apparatus; the measurement corresponds to 0.5δ radially in the gap. The axial flow rate is W_g=0$\frac{m}{s}$

Figure 4.7 shows sample data collected in the center of the gap at Re_θ=1110. The data shows a signal with oscillation frequency of 0.2Hz. In this condition SFA is said to have surpassed the critical Taylor number necessary to generate the Taylor-Couette instability as it shown in the azimuthal velocity statistics in the middle of the gap.

For higher Reynolds numbers it is seen that the velocity signal for the azimuthal component oscillates a higher frequency. Figure 4.8 shows the signal for the measured instantaneous azimuthal velocity at the same location as the data shown in Figure 4.7.

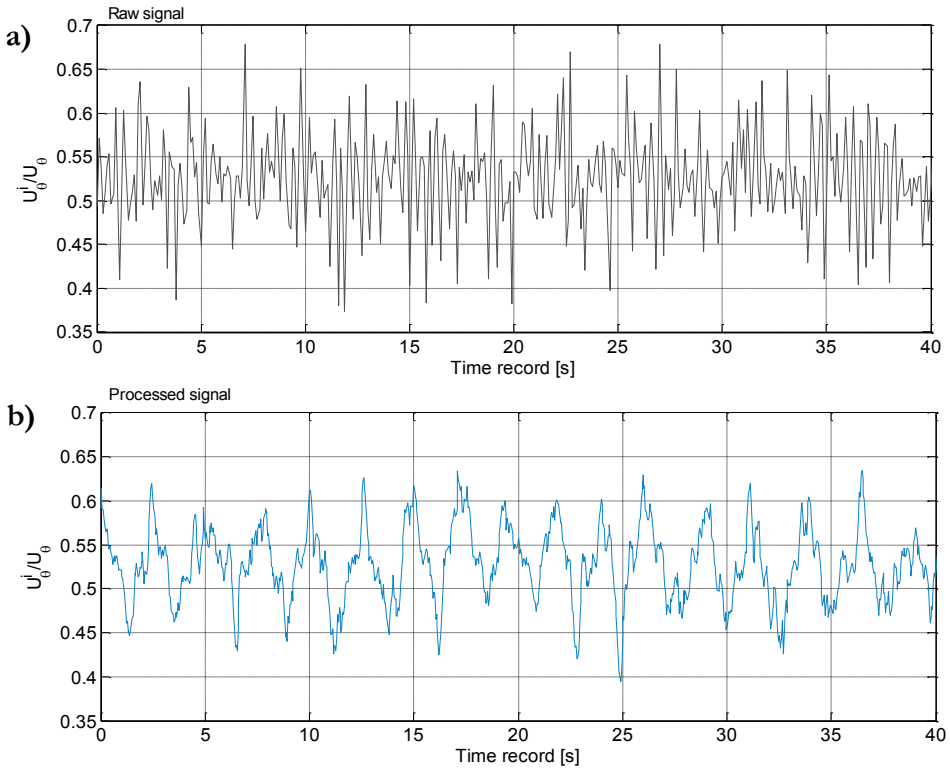

Figure 4.8. For batch condition, W_g = 0m/s. The figure shows normalized data for the azimuthal velocity component at Re_0=2230. a) Raw velocity signal of the azimuthal velocity component. b) Sample of the processed data where points beyond 3-standard deviation from the mean are removed and a low pass filter is applied.

By applying a low pass filter we are now allowed to observe a clear oscillating signal at this Reynolds number. The frequency of the periodic signal is ~0.45Hz showing that by doubling the impeller tip speed the frequency doubles from the previous scenario, at Re_0=1110. This suggests that both Reynolds numbers support a similar regime although the higher Re_0 appears to have a wider range of fluctuation frequencies.

4.2.1 Characterization in the gap, mean & RMS

Before mapping velocities across the gap, various measurements were taken near the moving and stationary walls to seek locations at which the measurement volume would intersect these boundaries. It was seen that the data rate at a distance of 100 μm from the stationary wall decayed considerably, and the instantaneous measured velocity (U_0^i, W_i^{gap}) at that location registered mainly $0\,\frac{m}{s}$ for the azimuthal component. as shown

in Figure 4.9a. On the other hand, near the impeller the measured azimuthal velocity, especially the azimuthal component registers the tip speed of the inner cylinder. Moreover, it was observed that the calculated root mean square (U_{rms}, W_{rms}) velocities both for the azimuthal and axial components increased when the LDV probe partially intersected the boundaries.

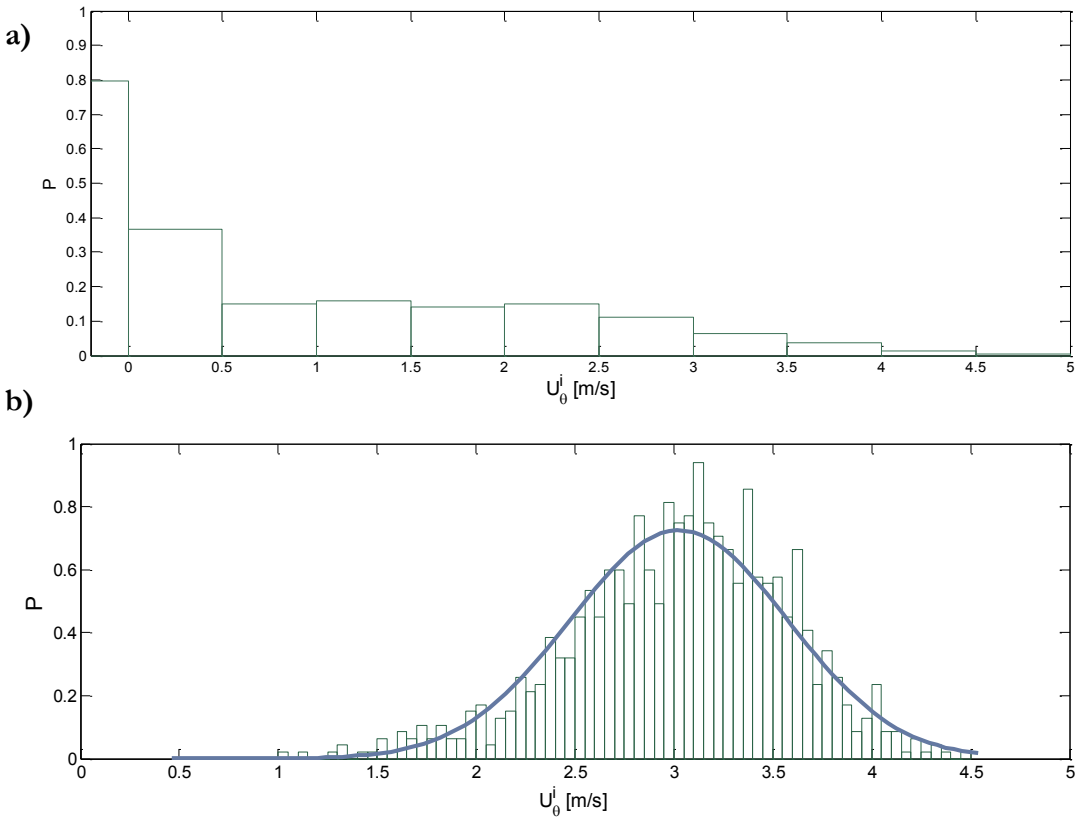

Figure 4.9. Histogram plots for the measured azimuthal velocity at a single location in the gap at height 6.5H_L. Variable U_θ^i corresponds to the instantaneous measured velocity. The impeller tip speed $U_\theta^i = 3.5\frac{m}{s}$, and the axial velocity $W_g = 0\frac{m}{s}$. a) Velocity histogram for a location 0.05δ from wall. b) Corresponds to the velocity histogram at 0.85δ from stationary wall.

Velocity statistics were computed at various locations within the SFA in batch condition, W_g=0$\frac{m}{s}$. These measurements took place at the axial (z) positions shown in Figure 4.6. The mean azimuthal velocity in the gap at the relevant Reynolds numbers is shown in Figure 4.10. At $Re_0 = 1110$ it is thought that the flow is operating at the Wavy Vortex

Flow regime, whereas for $Re_\theta = 2230$ the flow is nominally in the turbulent Taylor vortex regime. The data for the profiles at these conditions represent Taylor numbers of $4Ta_{cr}$ and $8Ta_{cr}$ for Re_θ=1110 and 2230 respectively.

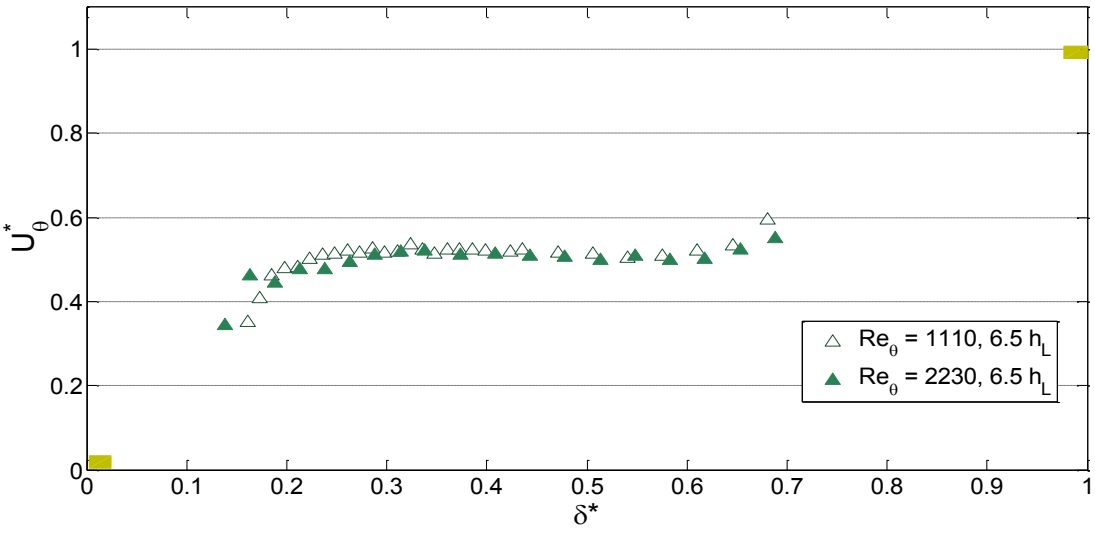

Figure 4.10. The figure compares the profile of the azimuthal velocity component in the gap at two Reynolds numbers. Square markers represent theoretical final value of the velocity vector following non-slip condition. Both conditions are evaluated at W_g=0m/s and 0.42V_T. (△) $Re_\theta = 1110$, (▲)$Re_\theta = 2230$

The plotted profiles show that for both conditions the magnitude of the azimuthal velocity decreases near the stationary wall, then it is raised to an average of $0.5U_\theta$ between radial locations 0.2δ-0.65δ. In the plot it is also observed that both profiles collapse at similar velocity magnitudes.

In the literature it is shown that for the turbulent regime, the azimuthal profile of a Taylor experiment at these conditions is undulated throughout the region 0.2δ to ~0.7δ (Wereley & Lueptow, 1994). In these results it is seen that the profiles for both Reynolds numbers have a undulation type of pattern for the same radial location as Wereley & Lueptow. Yet, the relative difference in the magnitude of the measured velocity when compared to their results is considerably smaller.

For the case of $Re_\theta = 1110$ as δ^* increases (towards the impeller) the measured velocity profile nominally increases in magnitude to a value of $0.58U_\theta$ later decreasing to $0.55U_\theta$

within the aforementioned radial distances. Although this behavior is seen for Wereley's apparatus, the profiles hereby shown in the gap do not encounter such large inflections on the azimuthal velocity.

At the larger Reynolds number, the azimuthal velocity in Figure 4.10 displays waviness in its magnitude similar as in the $Re_\theta = 1110$ case. For the $Re_\theta = 2230$ profile, the magnitude appears to increase for radial positions between 0.2δ-0.4δ. Then, the velocity gradually decreases at ~0.6δ to later raise in magnitude as it the measurement volume approaches the inner cylinder. The fluctuations in the measured velocity for both Reynolds number are twice the magnitude than the experimental uncertainty ($\sim 0.014 U_\theta$), suggesting that the observed waviness is true to the nature of the flow.

Figure 4.11 shows the averaged axial velocity profiles taken in the gap of the SFA for $Re_\theta = 1110$ and $Re_\theta = 2230$. In the figure it is observed that both profiles collapse at similar axial velocities for all the radial positions. The averaged measured velocity for $Re_\theta = 1110$ is found to be $-0.01U_0$ and $-0.009U_0$ for $Re_\theta = 2230$. The plot suggests a small down flow in the gap which of about 1% of the azimuthal tip speed. The deviation from zero, however, is within the order of uncertainty for these measurements, and could be caused, for example, by very small alignment errors.

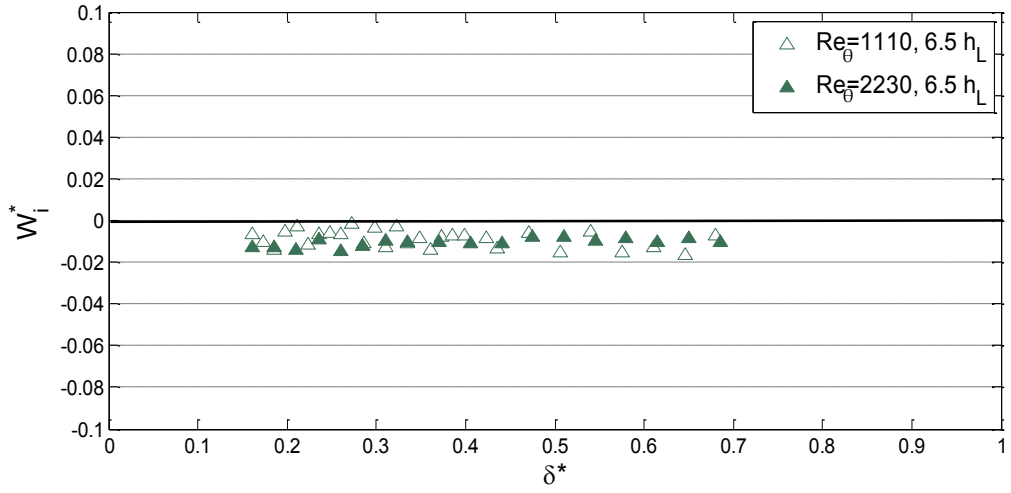

Figure 4.11. Normalized mean profile at the gap for the axial velocity component, measurements performed at $6.5h_L$. Both conditions are evaluated at W_g=0m/s and $0.42V_T$. Open triangles (△) are for $\mathbf{Re_\theta = 1110}$, and filled triangles(▲) are for $\mathbf{Re_\theta = 2230}$

The root mean square (RMS) velocities for the azimuthal and axial velocity components are shown in Figure 4.12 for $Re_\theta = 1110$ and $Re_\theta = 2230$. Figure 4.12a shows that for both Reynolds numbers the azimuthal RMS velocities increases near the boundaries. The data near the stationary wall shows RMS values of $0.1U_0$; the measured fluctuations are reduced as δ^* increases reaching values of $0.05U_0$ for $Re_\theta = 2230$ and $0.07U_0$ for $Re_\theta = 1110$. The data plotted for the azimuthal RMS profile shows similar behavior for both Reynolds numbers.

The data shows that the lowest azimuthal-RMS fluctuations are found near the radial center of the gap for both Reynolds numbers. The profiles also indicate that the RMS magnitude for $Re_\theta = 1110$ is on average $0.08U_0$ compared to $0.07U_0$ for the higher Reynolds number.

Figure 4.12b shows the axial-RMS velocity profile of the aforementioned Reynolds numbers. The profiles for both conditions collapse on one each other, even at positions near the impeller. Comparatively, the axial-RMS velocity for both Reynolds number is smaller than the azimuthal-RMS magnitude between 0.15δ and 0.3δ.

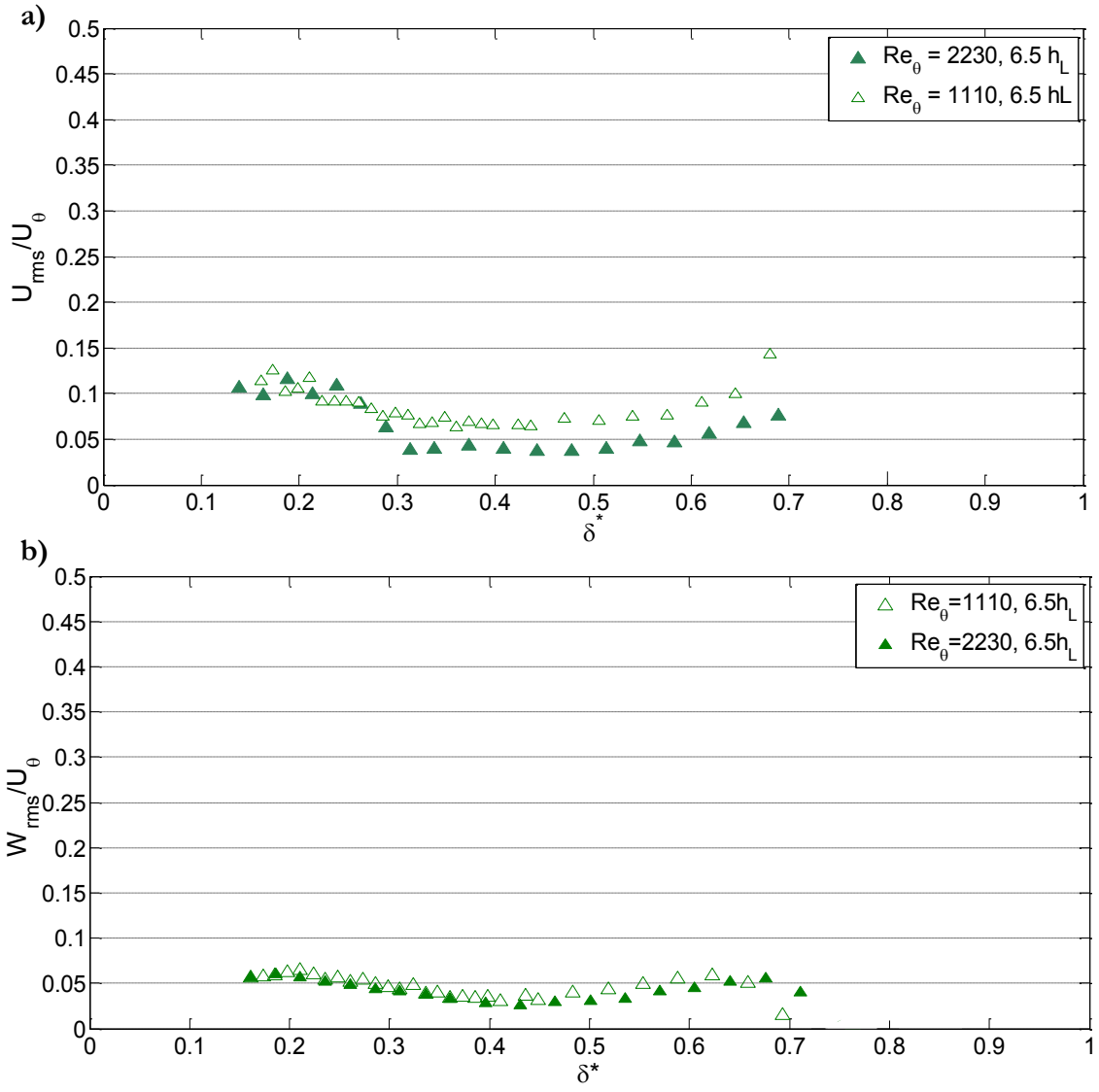

Figure 4.12. Normalized mean RMS velocities: (a) $\frac{U_{rms}}{U_\theta}$; (b) $\frac{W_{rms}}{U_\theta}$ at 6.5h$_L$. Filled markers are for Re$_\theta$=1110, hollow represent Re$_\theta$=2230. (Δ) Re$_\theta$=1110 and (▲) Re$_\theta$=2230. Measurements were performed in batch condition W$_g$=0 m/s and 0.42V$_T$.

For $Re_\theta = 1110$ the magnitude of W_{rms} between 0.3δ-0.6δ has the same magnitude as in the higher Reynolds number.

Interestingly W_{rms} has a similar magnitude as U_{rms} for data located between 0.3δ-0.6δ at $Re_\theta = 2230$. Yet, beyond 0.6δ the axial-RMS for this Reynolds number stays below $0.5U_\theta$.

4.2.2 Measurements at the bottom edge of the inner cylinder

Ekman vortices have been found to exist in canonical Taylor Couette flow experiments at the leading edges of the inner cylinder. They originate as a result of redistributed angular momentum due to the stationary upper and lower surfaces of the apparatus. These vortices are found to spin inwardly as discussed in Section 1.2.4. Nevertheless, there is no previous knowledge on the characteristics of the flow at the leading edges of an apparatus with an open space between the inner cylinder and the bottom/upper surfaces as the SFA is unique in this aspect. Therein, data is plotted for measurements in the gap at the leading edge of the inner cylinder at a height of $1.01h_L$.

The mapping of U_θ in the gap at the leading edge of the impeller shown in Figure 4.13a shows that at both Reynolds numbers the profiles collapse at the same values as in Figure 4.12a. In Figure 4.13a both Reynolds number show constant values U_θ^* from 0.2 δ -0.7 δ, whereas in Figure 4.10 the magnitude of the azimuthal velocity has a relatively small variation between 0.2δ -0.7δ.

Figure 4.13b shows the mean profiles for the axial velocity for experimental conditions at $1.01h_L$ at $Re_\theta = 1110$ and $Re_\theta = 2230$. The plot also includes the gap profile for the axial velocity at $Re_\theta = 2230$ and $6.5h_L$ for comparison. For $Re_\theta = 1110$ the magnitude of W_i^* decreases with increasing δ^*. For this condition the value of W_i^* spans from W_i^*=0.01 at 0.2 δ to W_i^*=-0.06 at 0.7δ. In comparison at $6.5h_L$ and similar Reynolds number, the magnitude of W_i^* was maintained at W_i^*=-0.01 across the gap.

For the higher Reynolds number condition at Re_θ=2230, the measured axial velocity increases with increasing δ^*. At this condition, W_i^* has a value of W_i^*=-0.08 at 0.2δ, the measured axial velocity is seen to increase linearly to near W_i^*=-0.01 at 0.7δ.

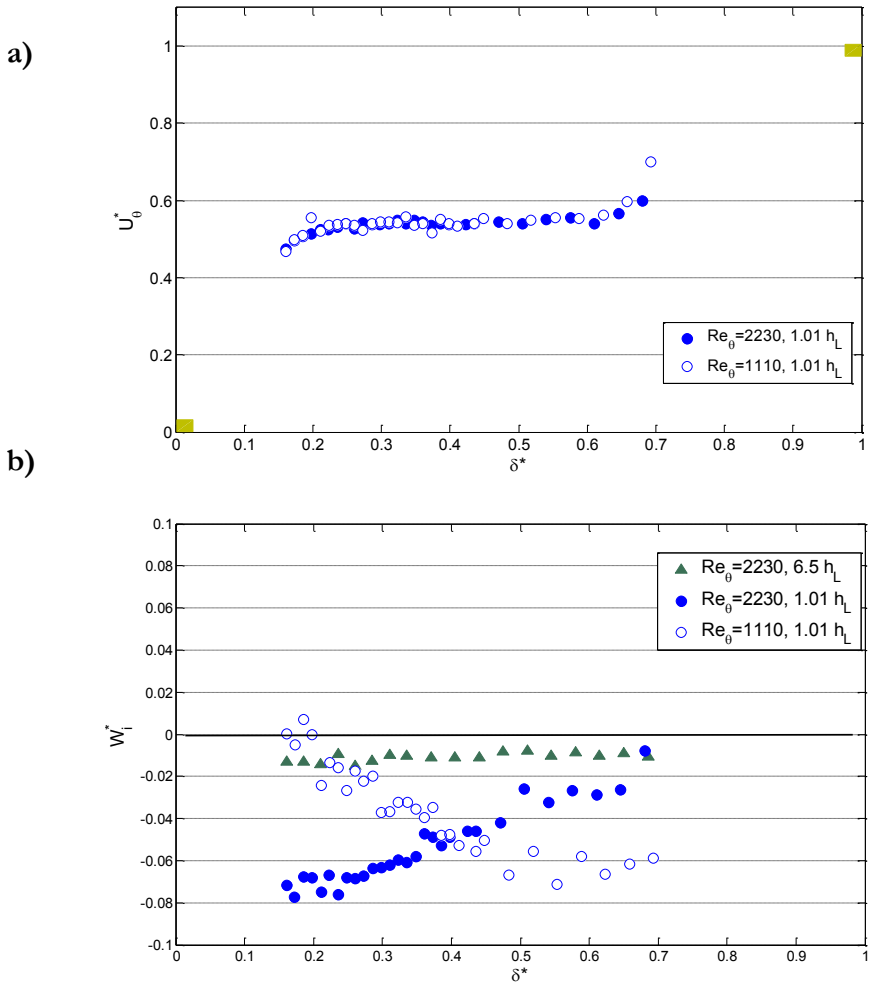

Figure 4.13. Gap profiles of the batch condition (W_g=0 m/s) at the bottom edge of the inner cylinder with a hold up volume of 0.42V_T. a) Normalized mean azimuthal velocity profile at the leading edge of the impeller for Re_θ=1110 & 2230 represented by hollow (○) and filled (●) markers respectively. b) Normalized mean axial velocity component. In b) the axial profile at 6.5h_L is shown as means for contrast, represented by (▲).

The significant difference between the axial velocities at the bottom corner (1.01h_L) and the middle point of the inner cylinder (6.5h_L) indicate that the topology of the flow is different at both locations. The difference between profiles for the two Reynolds numbers is surprising and difficult to explain by physical arguments.

Figure 4.14 shows the normalized root mean square (RMS) velocities for both dynamical conditions and heights 1.01h_L and 6.5h_L. Plotted in Figure 4.14a is the mean RMS velocity for the azimuthal velocity component. At both axial positions (1.01h_L and 6.5h_L) the

obtained RMS velocities for $Re_0 = 1110$ mostly overlap in the gap. With exception near the inner cylinder, at 0.68δ where it is seen that the intensity of the RMS velocity is larger for the data obtained $6.5h_L$. For Figure 4.14a the RMS for this Reynolds number decreases in magnitude to a minimum of $0.06U_0$ for both axial locations. The RMS-velocity difference between both axial positions for 0.7δ, is about $0.06U_0$, which is the largest RMS difference between the two data sets. The mean RMS azimuthal velocity for both heights ($1.01h_L$ and $6.5h_L$) is $0.08U_0$ for the azimuthal component.

For Re_0=2230 in Figure 4.14 closest to the stationary wall, the mean RMS is similar at both heights. However, as we move inward radially towards the impeller, the RMS start to increase for both positions at 0.18δ. The highest RMS measurement for this Reynolds number occurs for the data obtained at $1.01h_L$ having a value of $0.18U_0$.

For the profile at the bottom of the impeller and Re_0=1110, the RMS velocity drops abruptly to $0.045U_0$ reaching the same value as the data at $6.5h_L$ and Re_0=2230. A similar behavior occurs for the profile of Re_0=2230 and $6.5h_L$, where the RMS is at the highest value at 0.22δ recording a magnitude of $0.12U_0$, later decreasing to a minimum of $0.04U_0$ between 0.2δ -0.3δ. Beyond 0.35δ, the RMS for both Reynolds numbers maintains a stable value at both axial positions.

In Figure 4.14a, data plotted shows a smaller RMS magnitude than the normalized values for the lower Reynolds number at both axial locations. The jump in azimuthal-RMS from $0.1U_0$ to $0.15U_0$ for Re_0=1110 at $1.01h_L$ between 0.2δ -0.3δ is attributed to the signal filtering settings from experimentation and not attributes of the flow at those radial positions.

In Figure 4.14a, from 0.35δ-0.6δ all data collapses at values of $0.05U_0$ $\pm 0.02U_0$ for Re_0=2230. Interestingly, the calculated RMS for the data for Re_0=1110 is in average 25% than for the higher Reynolds number for the aforementioned radial (0.35δ -0.65δ) locations. In Figure 4.14a after ~0.65δ, the normalized RMS velocity for Re_0=1110 at

$6.5h_L$ increases to $0.15U_\theta$, however for Re_θ=2230 the azimuthal-RMS is ~$0.1U_\theta$ at the same radial position.

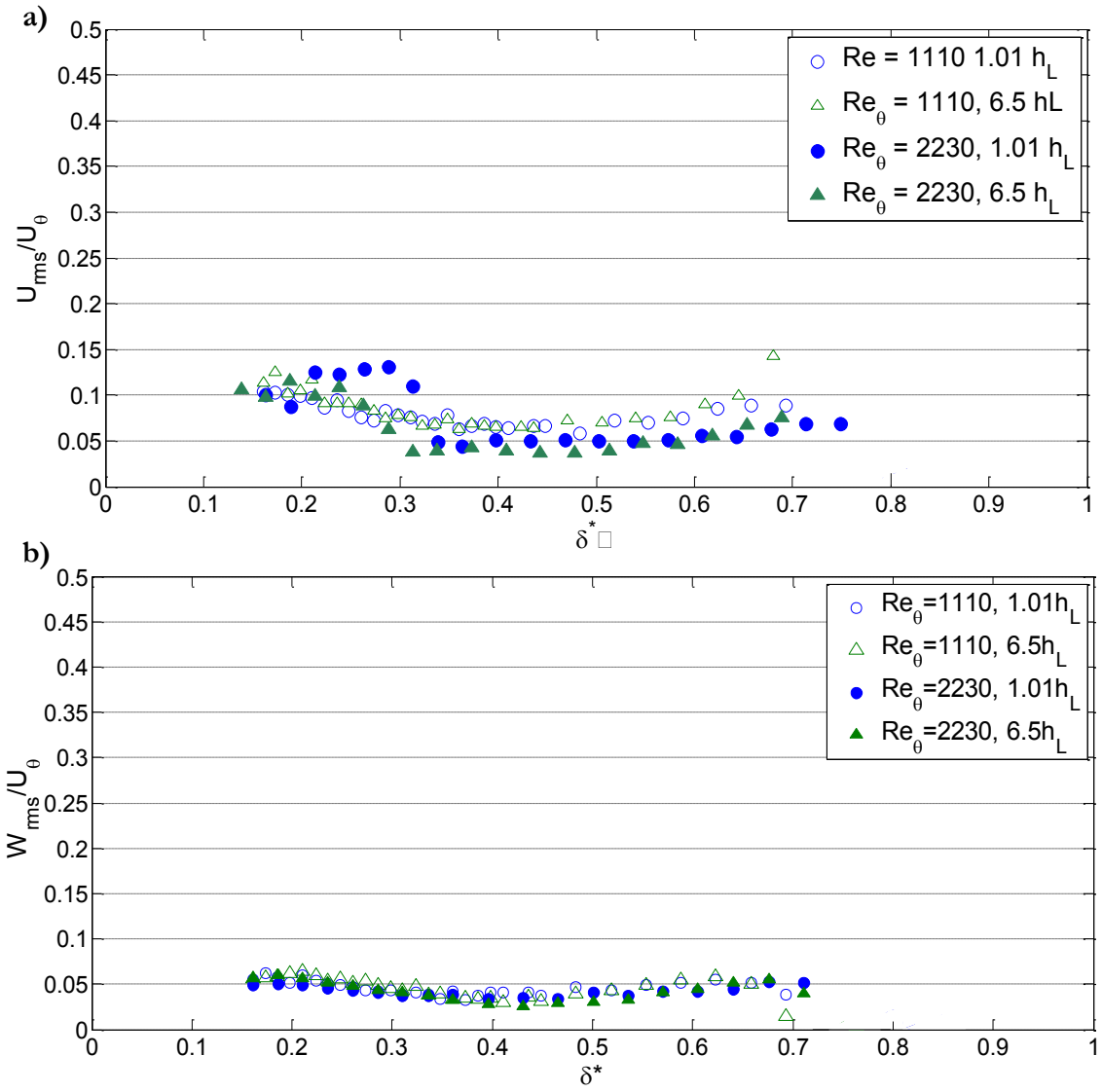

Figure 4.14. Normalized mean RMS velocities: (a) $\frac{U_{rms}}{U_\theta}$; (b) $\frac{W_{rms}}{U_\theta}$ at locations $6.5h_L$ and $1.01h_L$. All measurements were obtained at W_g=0 m/s and $0.42V_T$. Filled markers are for Re_θ=1110, hollow represent Re_θ=2230. For height $1.01h_L$ & Re_θ=1110 (○); $6.5h_L$ & Re_θ=2230 (●); $1.01h_L$ & Re_θ=1110 (Δ); height $6.5h_L$ & Re_θ=2230 (▲).

Figure 4.14b shows the normalized axial RMS velocity profiles in the gap at $1.01h_L$ and $6.5h_L$, for Re_0=1110 and Re_0=2230. The profiles for the magnitude of the RMS velocity at both Reynolds numbers are observed to collapse throughout the gap, which also occurs at $6.5h_L$.

4.2.3 Velocity statistics beneath the inner cylinder

Similar measurements as in the gap were performed in the space between the bottom of the impeller and the base of the apparatus. In Figure 4.15, the impeller radial location is shown as a darkened rectangle at the top of the figure. Figure 4.15 shows the normalized azimuthal velocity profiles at the middle point between the inner cylinder and the bottom of the apparatus, $z=0.5h_L$, and $z=0.8h_L$ just underneath the impeller's edge.

The theoretical film-thickness for a holding volume of $0.42V_T$ is 9 mm corresponding to a radial distance of 4.5δ from the wall. For data at Re_0=1110 the boundary is not fully developed as discussed in Section 4.1.1. The boundary resides inward of 4.5δ, allowing for measurements beyond the theoretical boundary location.

Moving away of the stationary wall for both Reynolds numbers, Figure 4.15 shows that the measured azimuthal velocities increase between 0.2δ-0.4δ maintaining similar U_0^* values. After 0.4δ at Re_0=1110 and $0.5h_L$, the measured azimuthal velocity maintains a constant value within $\pm 0.01 U_0^*$ from its peak of U_0^*=0.58 until 1.4δ as seen in Figure 4.15b (which is an expanded view of Figure 4.15a), afterwards it starts to drop monotonically towards the radial center of the apparatus.

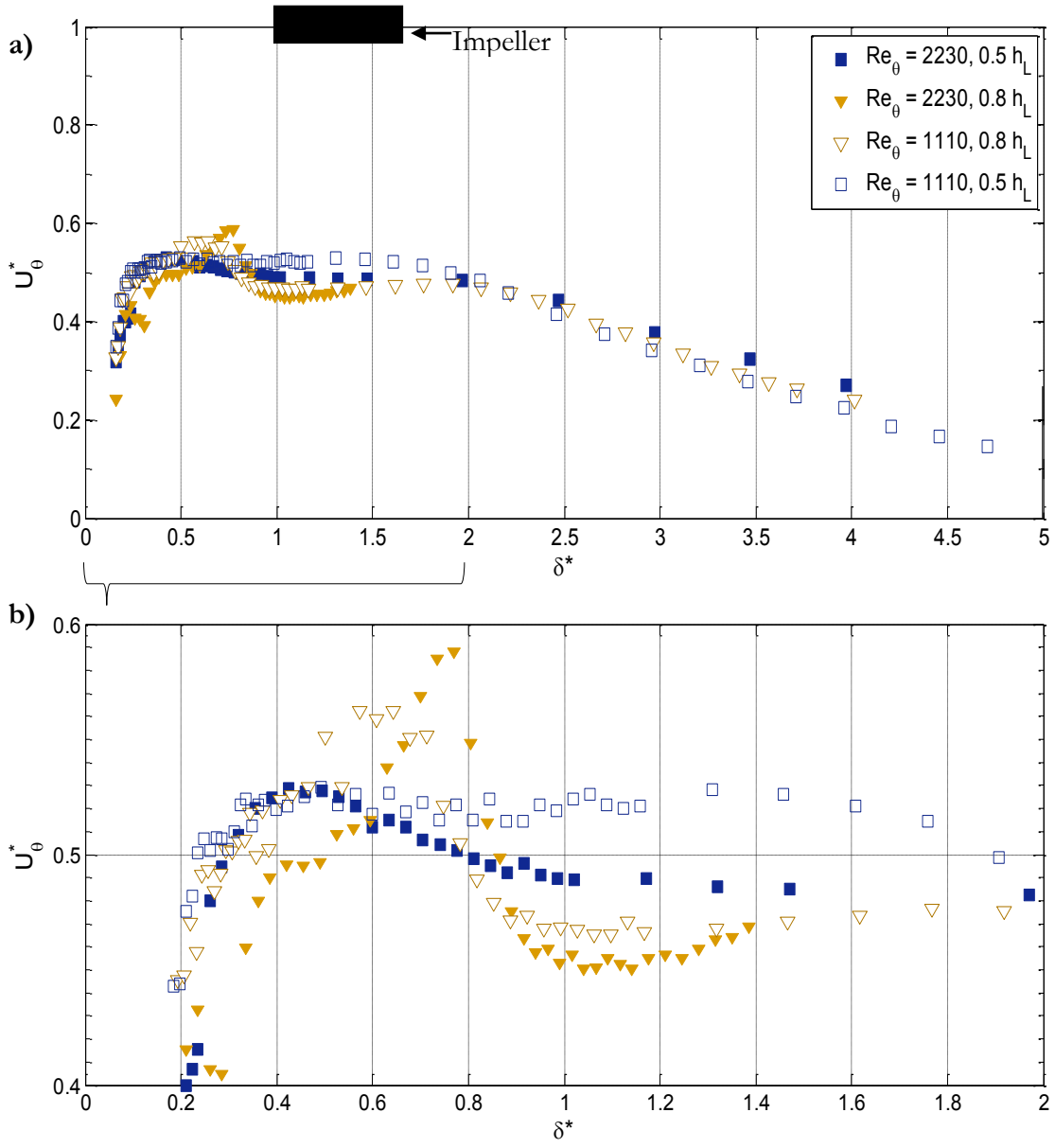

Figure 4.15. Normalized mapping of the mean azimuthal velocity profiles underneath the impeller at various heights. The location $\delta^* = 0$ refers to the wall of the outer cylinder. For height for 0.5h$_L$ & Re$_\theta$=2230 (■); for 0.8h$_L$ & Re$_\theta$=2230 (▼); for 0.8h$_L$ Re$_\theta$=1110 (▽); 0.5h$_L$ & Re$_\theta$=1110 (□). a) Shows the complete mapping up to δ^* =5 from the stationary wall. b) Shows the expanded view from the wall up to δ^*=2 and U^*_θ between 0.4-0.6. The SFA was operated in batch W$_g$=0 m/s and 0.42V$_T$.

For Re$_0$=2230 and 0.5h$_L$, the measured velocity magnitude starts to decrease from U^*_0=0.53 to a minimum of U^*_0=0.5 at a constant slope between radial positions 0.4δ- 0.8δ. Then, the velocity decreases in magnitude steadily by -0.01 $\frac{U^*_\theta}{\delta^*}$. The slope of the normalized azimuthal

velocity shifts again after 2δ as the profile is moves towards the radial center of the apparatus. Beyond the aforementioned radial position, the azimuthal velocity profile decreases at a rate of $-0.12\frac{U_\theta^*}{\delta^*}$ up to 6δ; which is the last measured point for this data set.

At both Reynolds numbers, points closer to the impeller at $z=0.8h_L$ show similar trends between 0.2δ-0.4δ, as for $z=0.5h_L$. Yet, the azimuthal velocity continues to increase rapidly between 0.5δ-0.8δ for both Reynolds numbers. For the data at $Re_0=1110$ and $0.8h_L$ it is seen that the velocity reaches a maximum value of $U_0^*=0.55$ at 0.6δ, whereas for $Re_0=2230$ the measured velocity peaks at $U_0^*=0.59$ at 0.8δ. The elevated gradient in the mean azimuthal velocity at a distance 600 μm below the impeller indicates high shearing at these locations. After peaking in magnitude near 0.8δ, the velocity decays sharply.

For the profiles at $0.8h_L$ it is observed that in the case of $Re_0=2230$, the peak of the velocity is higher than at $Re_0=1110$. Yet, the profile for the higher Reynolds number appears to drop to a lower velocity magnitude than its counterpart (at the same height). Moreover, between the radial positions of 0.8δ-1.4δ and for both heights, the measured velocities for $Re_0=1110$ are larger than those for $Re_0=2230$. These results are consistent with the idea that boundary layers are thinner for higher Reynolds numbers.

All measured locations and dynamical conditions seem to collapse starting at 2δ for the azimuthal velocities shown in Figure 4.15, decreasing monotonically up to a distance of 5δ from the stationary wall and 28δ from the axial center of the apparatus.

Figure 4.16 shows results for the mean axial profiles underneath the impeller. The acquired axial locations and Reynolds numbers are the same as in Figure 4.15. For $Re_0=1110$ and $Re_0=2230$ near the stationary wall $W_i^*=-0.05$ & -0.08 for each height as seen in Figure 4.16b.

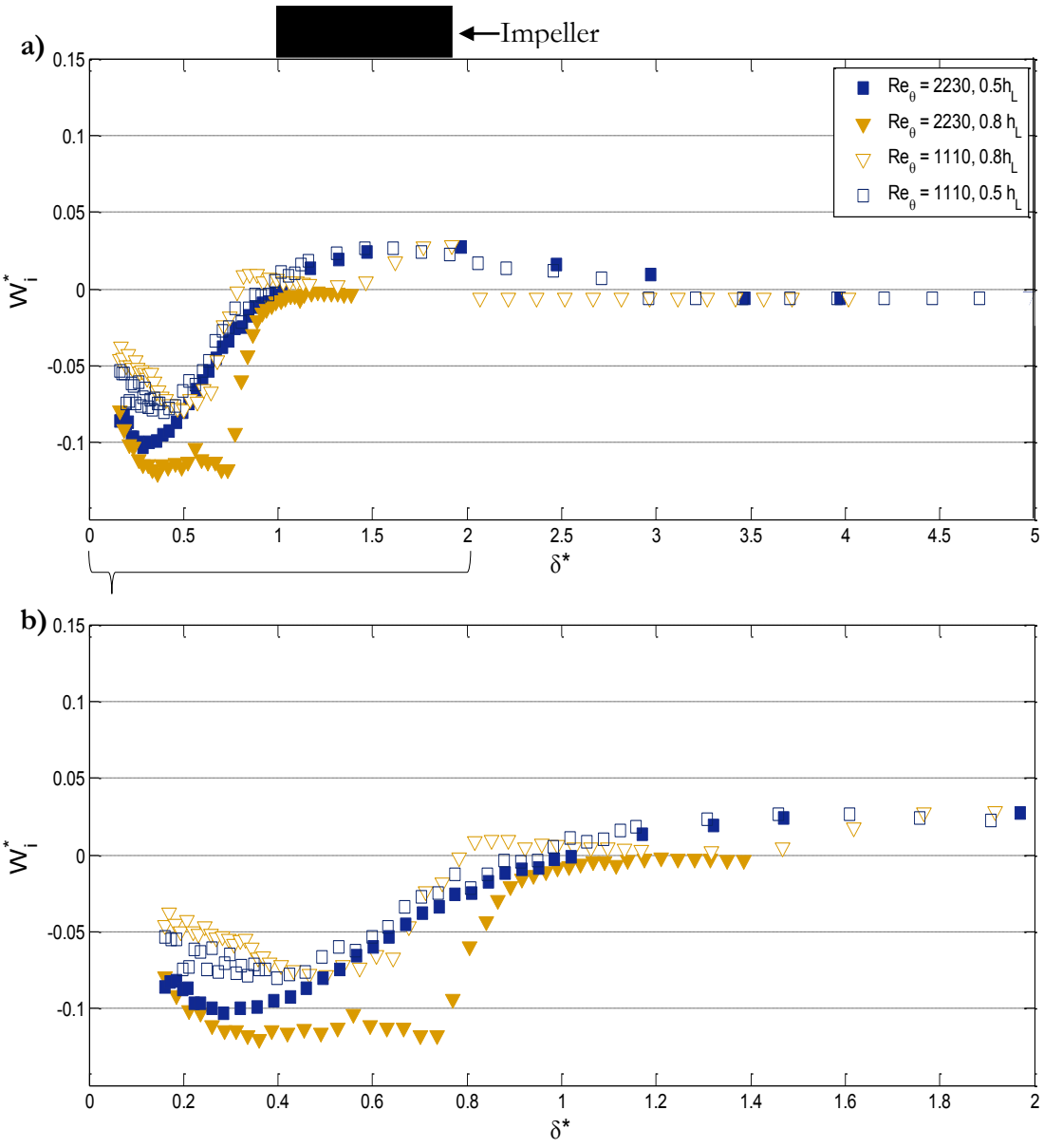

Figure 4.16. Normalized mapping of the mean axial velocity profiles underneath the impeller at various heights. For height for 0.5h$_L$ & Re$_\theta$=2230 (■); for 0.8h$_L$ & Re$_\theta$=2230 (▼); for 0.8h$_L$ Re$_\theta$=1110 (▽); 0.5h$_L$ & Re$_\theta$=1110 (□). a) Shows the complete mapping up to $\delta^* = 5$ from the stationary wall. b) Shows the expanded view from the wall up to $\delta^* = 2$ and U_θ^* between 0.4-0.6 .The SFA was operated in batch W$_g$=0 m/s and 0.42V$_T$.

For both Reynolds numbers at 0.5h$_L$, the normalized axial velocity increased in magnitude after δ^*=0.4 by changing in slope. In the plot, the increase occurs at a constant rate until δ^*=0.7;s coincidentally at this location the magnitude of W_i^* is close zero. Then, the axial

velocity becomes positive with a maximum value of $W_i^* = 0.04$ for both Reynolds numbers. Then at 2δ from the stationary wall, the measured axial velocity starts to decrease until it reaches $W_i^* = 0$.

For height of $0.8h_L$ and radial locations between 0.1δ and 0.9δ, the downward axial velocity for $Re_0 = 1110$ is smaller in magnitude than for $Re_0 = 2230$. Also, the gradient shown by $Re_0 = 1110$; when the velocity begins to increase the point that it reaches $W_i^* = 0$, is weaker than at $Re_0 = 2230$.

In Figure 4.16 the measured axial velocity for heights at $0.5h_L$-$0.8h_L$ increases between $0.2\delta - 1\delta$ to values above zero average axial velocity ($W_i^* = 0.001$) for all Reynolds numbers. This suggests that, on average, a sustained vortex rotating counter clockwise exists underneath the impeller. Yet, the existence of an eddy does not necessarily correlate to the common Ekman type vortex found in the canonical Taylor instability problems at the edges of the cylinders.

4.3. Effects of transversal holes

As shown in Chapter 1, 2 and Appendix A, the inner cylinder in the SFA (also known as the impeller) has 8 holes transversally located between the impeller-inner wall and the locations where the shaft is attached to the impeller. Together, the transversal holes have a larger cross sectional area than the gap. To our knowledge, these holes are present at the SFA as a mechanical design constraint rather than influencing the milling ability of the apparatus.

In batch condition, the liquid fills the SFA before the impeller is inserted (with or without holes). Therefore, for the case with holes on the impeller, the air in the chamber is allowed to equilibrate with the atmosphere. In the case without holes, air is trapped beneath the impeller plate so that an air bubble forms atop of the liquid during the operation.

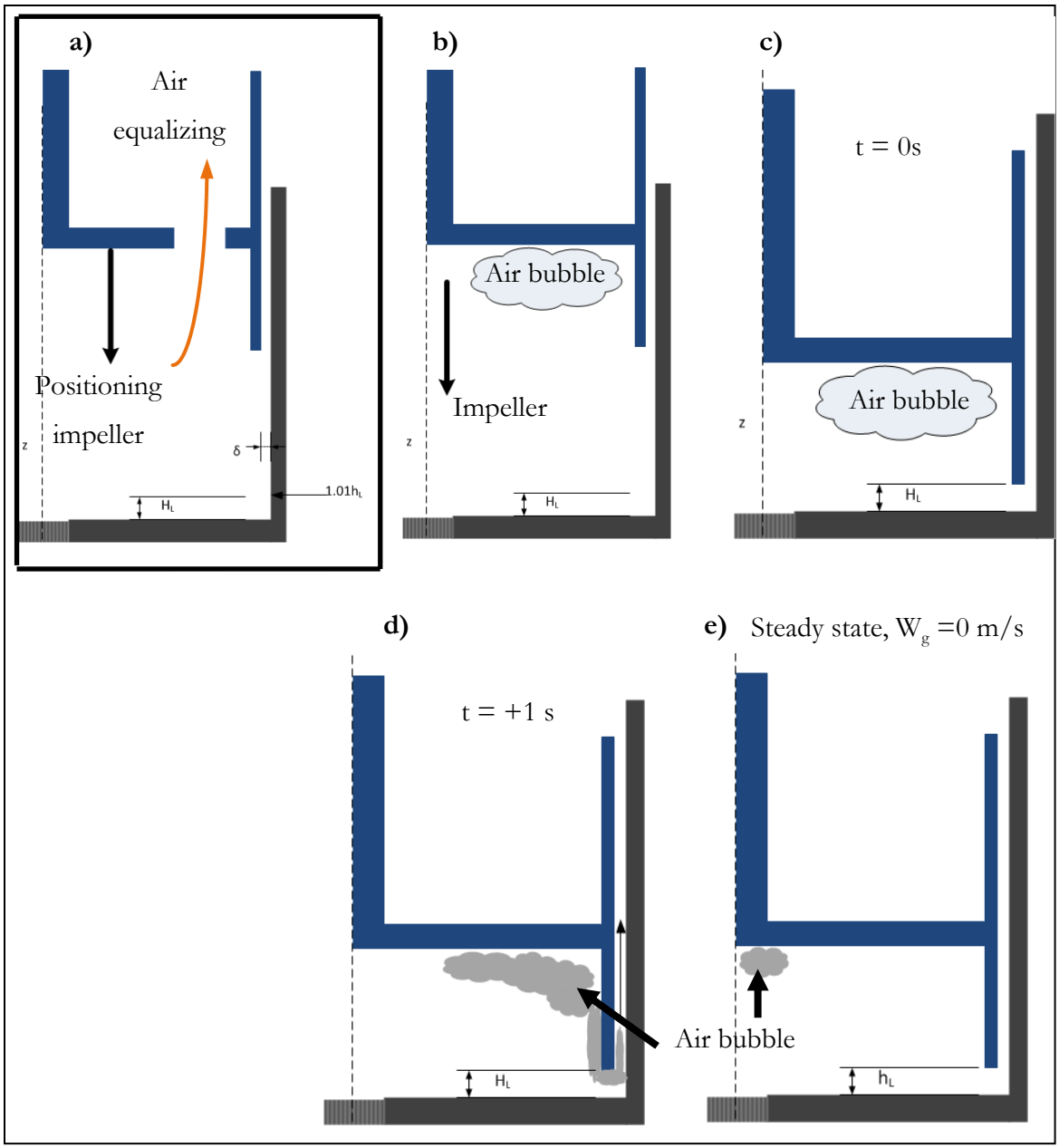

Figure 4.17. The images show a pictorial view of the SFA before achieving steady state with 2 different impeller properties at both Reynolds numbers and 0.42V_T. a) Impeller is being traversed towards the final position; the orange arrow shows air leaving the area underneath the shaft equalizing with atmosphere through the transversal holes. b) SFA with closed holes. c) Moment before initiating rotation of the impeller. d) View of 1 second after staring apparatus. e) Steady state view, remaining air does not leave the SFA.

The cartoons in Figure 4.17 show various views of the scenario that causes the SFA to have entrained air while preparing the apparatus. In Figure 4.17a, the impeller has the transversal holes uncovered and therefore the air is allowed to escape and equalize with the rest of the apparatus. Whereas in plots b) through e) the holes are covered showing the mechanism by which an air-bubble is held in the SFA, upon startup (Figure 4.17d) bubbles were observed to scape. In cartoon e) a small air bubble remains, this means that the free boundary has to accommodate to whatever the size of the bubble is. The presence of this bubble was verified visually, yet no quantitative value of its volume is presented.

4.3.1 Observations in the gap

Figure 4.18 shows the profiles of the normalized azimuthal velocity and the RMS for the same plot in the gap. The plotted data corresponds to Re_0=1110 and Re_0=2230 for an impeller with holes and one in the absence them. The profiles were taken at $6.5h_L$ from the bottom surface of the apparatus. The condition with holes is hereby referred as (WH), the data with no transversal holes the is represented by the acronym (NH).

In Figure 4.18a comparing the plotted data for Re_0=1110 it is observed that near the stationary wall and across the gap, the magnitude of the azimuthal velocity is higher for the no-holes condition. The average magnitude of the normalized azimuthal velocity at this Reynolds number for the WH condition is $0.51U_0$, whereas the other is $0.58U_0$. Beyond 0.2δ at Re_0 =1110, the profile for NH data is flat throughout the gap. At Re_0=2230, the magnitude of the azimuthal velocity between $0.2\,\delta$ -$0.3\,\delta$ is larger for the WH data than for the NH condition. After 0.3δ both profiles have the same registered azimuthal velocity.

In Figure 4.18b for Re_0=1110, the azimuthal RMS velocity between 0.18δ-0.38δ is larger for the NH condition. Then, both plotted profiles collapse at equal RMS values throughout the gap. Yet, for Re_0=1110 both NH and WH profiles overlap at similar azimuthal RMS values with a mean deviation smaller than the experimental uncertainty that being $0.01U_0$.

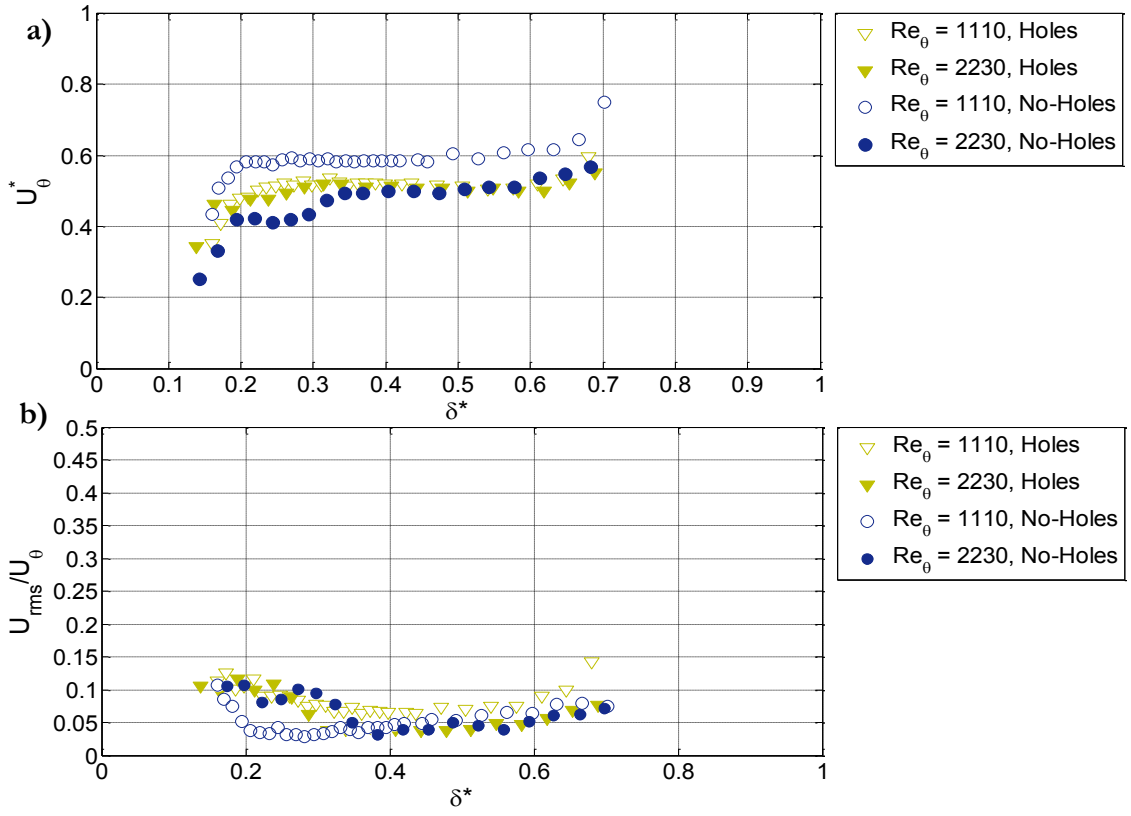

Figure 4.18. Comparative plots for the profiles in the gap for impeller with and without transversal holes at Re_θ=1110 and Re_θ=2230. The data was acquired at W_g=0m/s, 0.42V_T and 6.5h_L. a) Normalized mean azimuthal velocity profile at several Reynolds numbers. b) Corresponding normalized RMS values for the profiles on shown in a).

Figure 4.19 shows the mapping of the axial velocity for conditions WH and NH at the aforementioned Reynolds numbers. The plotted normalized axial velocity for all conditions shows negative values indicating a small down flow within the gap. The variation of axial velocity between data points of similar Reynolds number is $0.03U_0$. The plot shows that for both Reynolds numbers, the data for the inner cylinder without transversal holes overlaps with the one collected when the transversal holes are present.

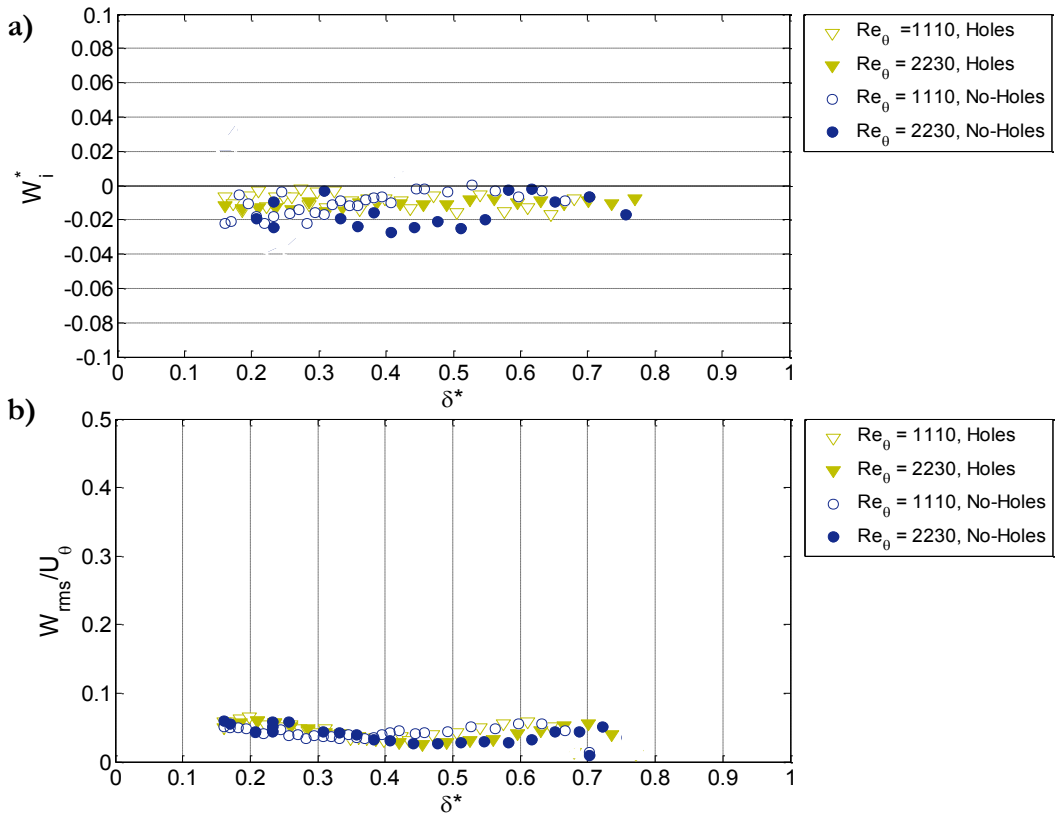

Figure 4.19. Comparative plots for the flow profile in the gap with and without transversal holes for. The data corresponds to W_g=0m/s, 0.42V_T and 6.5h_L in the gap. a) Normalized axial velocity profiles. b) Corresponding normalized RMS values for the profiles on shown in a).

The same is observed for the azimuthal RMS velocity at both Reynolds numbers and transversal holes conditions. The plots in Figure 4.19 indicate that the RMS velocity in the gap is not affected by the presence of the transversal holes, although the liquid column (film) goes beyond the radial location of the holes at both Reynolds numbers.

These results suggest that WH and NH profiles are in agreement and therefore by continuity there is little net flow through the holes in normal operation.

4.3.2 Observations underneath the gap – Spinning film

Figure 4.20 contains the plotted profiles for Re_θ=1110 at 0.5h_L for the recorded axial velocity. Plotted in Figure 4.20 is shown that the mean axial velocity for the impeller without holes has a maximum positive velocity (upward direction) of 0.05U_θ between

0.7δ and 1.3δ, whereas for the impeller WH the measured axial velocity moves from $-0.06U_0$ up to $0.01U_0$ for the same radial distance.

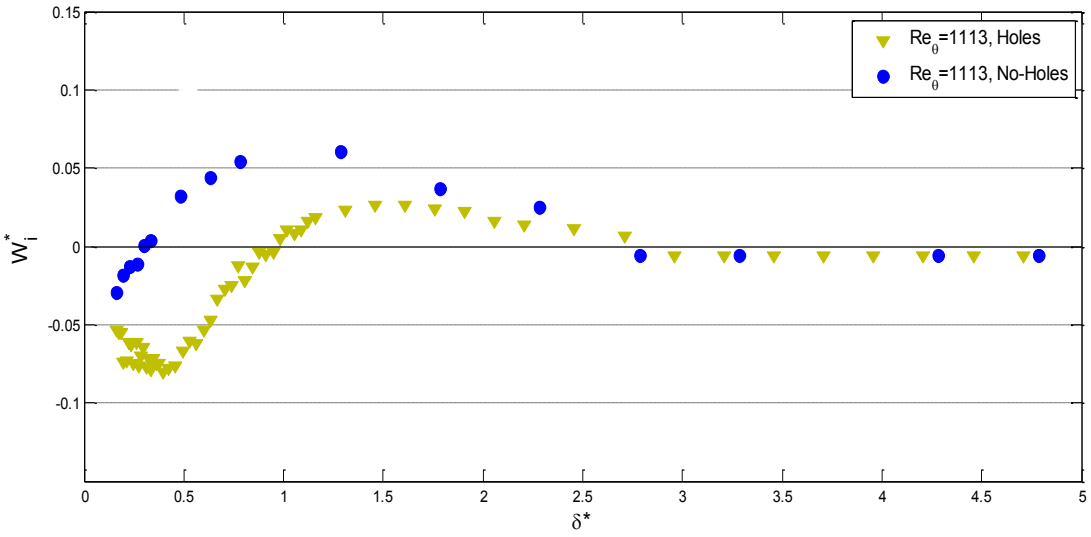

Figure 4.20. Comparative plots for the flow profile at the gap with and without transversal holes. The data was acquired at W_g=0m/s and 0.42V_T. Measurements performed at 0.5h_L underneath the impeller. Marker (▼) is for data obtained with an impeller having transversal holes. Marker (●) is data for impeller without holes.

Figure 4.20 shows that at radial positions beyond the location of the impeller inner wall (2δ) the axial velocities collapse with an axial velocity of W_i^* near zero. The overlap of both conditions occurs precisely at 3δ and continues to the end of the measurement. The acquired data at radial locations beyond 3δ are alongside where the transversal holes would be located axially. Therefore, it indicates that no relevant changes on axial flow direction or magnitude occur as a result of the existence of the transversal holes. This finding indicates that the holes at the impeller play no significant role on the flow through the gap, even though their radial-surface area is 13% of the SFA compared to the area covered by the gap which is 9%.

Chapter 5.

Instantaneous flow patterns and single plane PIV

The principal Reynolds numbers evaluated in this manuscript correspond to Re_θ =1110 and Re_θ=2220. The base case of the SFA set-up corresponds to the batch mode with a holding volume of $0.42V_T$, equivalent to f_s=9mm (in continuous mode).

In batch and continuous modes, flow visualization was performed to obtain the instantaneous structures of Taylor like vortices within the SFA. The method using Kalliroscope particles is described in Section 2.3.2. The acquired images were post-processed using various image processing techniques. The main tool applied in flow visualization was a temporal-spatial transformation of the images.

The transformation consisted of stacking a single line of pixels on the preferential plane for all images within a sequence. The pixel-line must be held at the same location for all images through the operation. To obtain the temporal information, only the acquisition rate is necessary, the final result is a single image containing the spatial and temporal information for the sequence. The transformation applied showed in all experiments that in the axial-time plane (t,z) periodic flow structures appeared to be defined, whereas in the radial-time plane the transformed images contained drift and a high frequency component without defined structure (White, Muller 2002, Babcock, Guenter et al. 1991).

The experimental conditions shown in this chapter for both flow visualization and PIV are presented in Table 5.1, the table contains information about upper plate thickness, Reynolds number, axial flow condition and acquisition rate.

Table 5.1. Individual experimental conditions for PIV and flow visualization.

Acronym	Condition	f_s [mm]	Re_0	Frame rate [kHz]	W_g [m/s]
B9-1-2	Batch	9	1110	2.0	0
B9-2-2	Batch	9	2230	2.0	0
B9-3-3	Batch	9	3190	3.0	0
B9-6-3	Batch	9	6360	3.0	0
B12-1-2	Batch	12	1110	2.0	0
B12-2-2	Batch	12	2230	2.0	0
B12-3-3	Batch	12	3190	3.0	0
C6-1-4-1	Continuous	6	1110	4.0	0.014
C9-1-4-1	Continuous	9	1110	4.0	0.014
C12-1-4-1	Continuous	12	1110	4.0	0.014
C9-1-2-2	Continuous	9	1110	2.0	0.02
C9-2-2-2	Continuous	9	2230	2.0	0.02
C9-3-4-2	Continuous	9	3190	4.0	0.02
C9-6-4-2	Continuous	9	6360	4.0	0.02
C6-1-41	Continuous	6	1110	4.0	0.06
C9-1-2-6	Continuous	9	1110	2.0	0.06
C12-1-4-1	Continuous	12	1110	4.0	0.06
C9-2-2-6	Continuous	9	2230	2.0	0.06
C9-3-3-6	Continuous	9	3190	3.0	0.06
C9-6-6-6	Continuous	9	6360	6.0	0.06

The acronym of a specific run is compounded from the conditions shown in column 2 through column 6 in Table 5.1. The first letter of the acronym indicates the axial flow mode, batch mode (letter **B**) or with axial through flow (letter **C**). The number that follows the letter corresponds to the upper plate thickness (f_s). For batch conditions the upper plate thickness correlates to the holding volume ratio shown in Table 2.5.

Following the initial combination of letters and numbers, the first number following the dash corresponds to the Reynolds number, where 1 and 2 would correspond to conditions at $Re_0 = 1110$ or $Re_0 = 2230$ respectively. After the second dash, the third

number corresponds to acquisition frame rate. For cases in continuous mode, a third dash separates the first significant figure of the axial flow velocity W_g from the rest of the information.

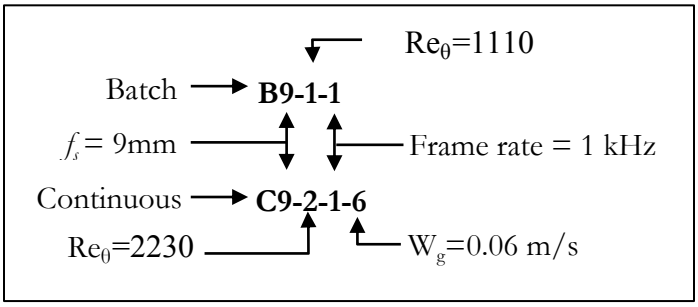

Figure 5.1. Shows a sample of the naming used for experiments. The upper acronym corresponds to a data point obtained in batch condition, with f_s=9 mm, Re_0=1110 and acquired at a 1 kHz frame rate. The second acronym in the bottom, corresponds to a run in continuous mode, Re_0=2230 and equal f_s and frame rate as the one above

5.1. Characteristic wavelengths at various conditions

The transformation performed in flow visualization allows obtaining the axial wavelengths, oscillation frequency and other features of the vortex pairs occurring in the SFA apparatus. The wavelength and other features are obtained from the transformation of images in the axial plane into the time plot shown in Figure 5.2.

Figure 5.2 shows a temporal-spatial transformation applied to both axial and radial directions. The same methodology is used for all visualization images that contained Kalliroscopic particles. The axial plane corresponds to the $\frac{z}{\delta}$ axis and the radial plane to the $\frac{r}{\delta}$. The image was acquired at a frame rate of 2 kHz, with a total acquisition time of 0.35s. The time domain was normalized using the angular velocity of the inner cylinder (ω).

A noticeable change in the intensity of light occurs at a height of 2.5δ in Figure 5.2a. At this height, the lower edge of the impeller is located. Below this point is the bottom corner of the apparatus, where the lower free boundary develops. A similar contrast in light intensity at this location is seen in Figure 5.2b which corresponds to the axial-time

transformation. At the height of 30δ in Figure 5.2a-b lies the edge of the inner cylinder, above this mark is the upper free boundary.

Figure 5.2b shows the temporal-axial transformation of the image sequence. In the plot one can observe defined structures with a wave like pattern. The wavelike structures have a different noise pattern than the background. Moreover, each one of these structures is surrounded by a darker region above and below, which follows their contour through the time domain. These regions of less intensity enhance the contrast between the wavelike structures and the background. Each one of these structures is called a vortex ring ($\lambda_{1/2}$), with a wavelength equal to one half of a vortex pair (λ) with units of length.

In Figure 5.2c (radial transformation), the image does not show information on flow structures through simple observation. The dark spot that appears at a radial location between 15δ -20δ in Figure 5.2c corresponds to the opaque area in Figure 5.2a at the same location.

The variable λ in Figure 5.2b corresponds to the thickness of two counter rotating vortices. The average scale of one vortex ring $\lambda_{1/2}$ (half the thickness of a vortex pair) was found to be ~1.9δ for Re_0=1110 and a holding volume $0.42V_T$. The measured average vortex pair wavelength in Figure 5.3a was found to be 3.7δ. Figure 5.3 shows an expanded view of Figure 5.2b to show the vortex wavelength and frequencies for a larger time record (1 s).

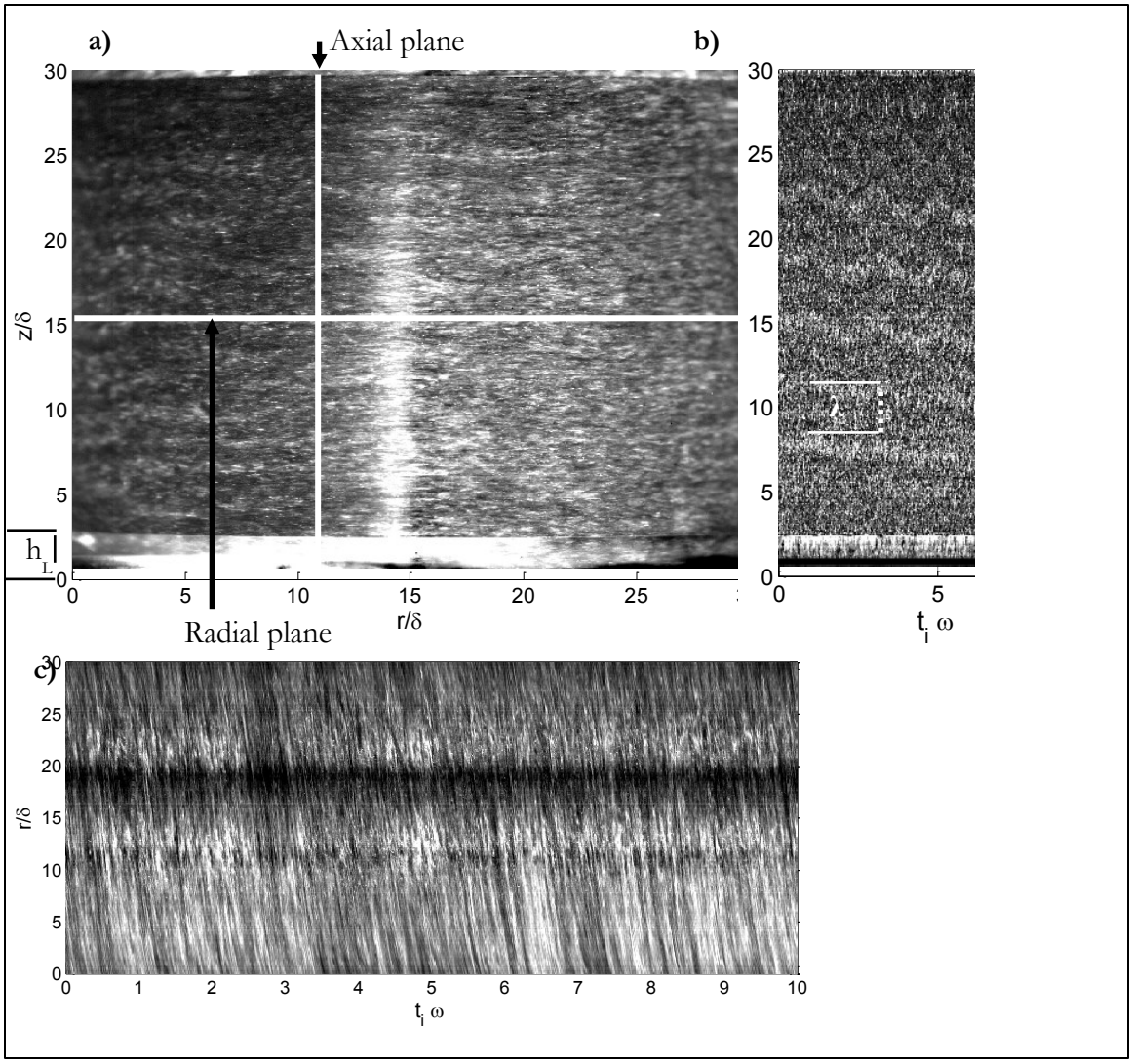

Figure 5.2. Example of transformations of an image sequence for experiment B9-1-2. The experiment was performed with W_g=0 m/s, Re_θ=1110 and total acquisition time of 0.7s. a) Shows a visualization image with 1% Kalliroscope particles. b) Transformed image for the axial-time domain. c) Transformed image for the radial-time domain. λ corresponds to half of the vortex pair wavelength.

In Figure 5.2, t_i corresponds to the time stamp of a pixel line, and ω is the rotational speed of the inner cylinder. The transformed image Figure 5.2b corresponds to a total acquisition time of 0.7s. In the image (Figure 5.2), the average peak to peak time is 0.12 s, corresponding to an oscillation frequency of ~7.8 Hz. Similarly, Figure 5.3a shows a larger time record with an average peak to peak time of 0.12 s.

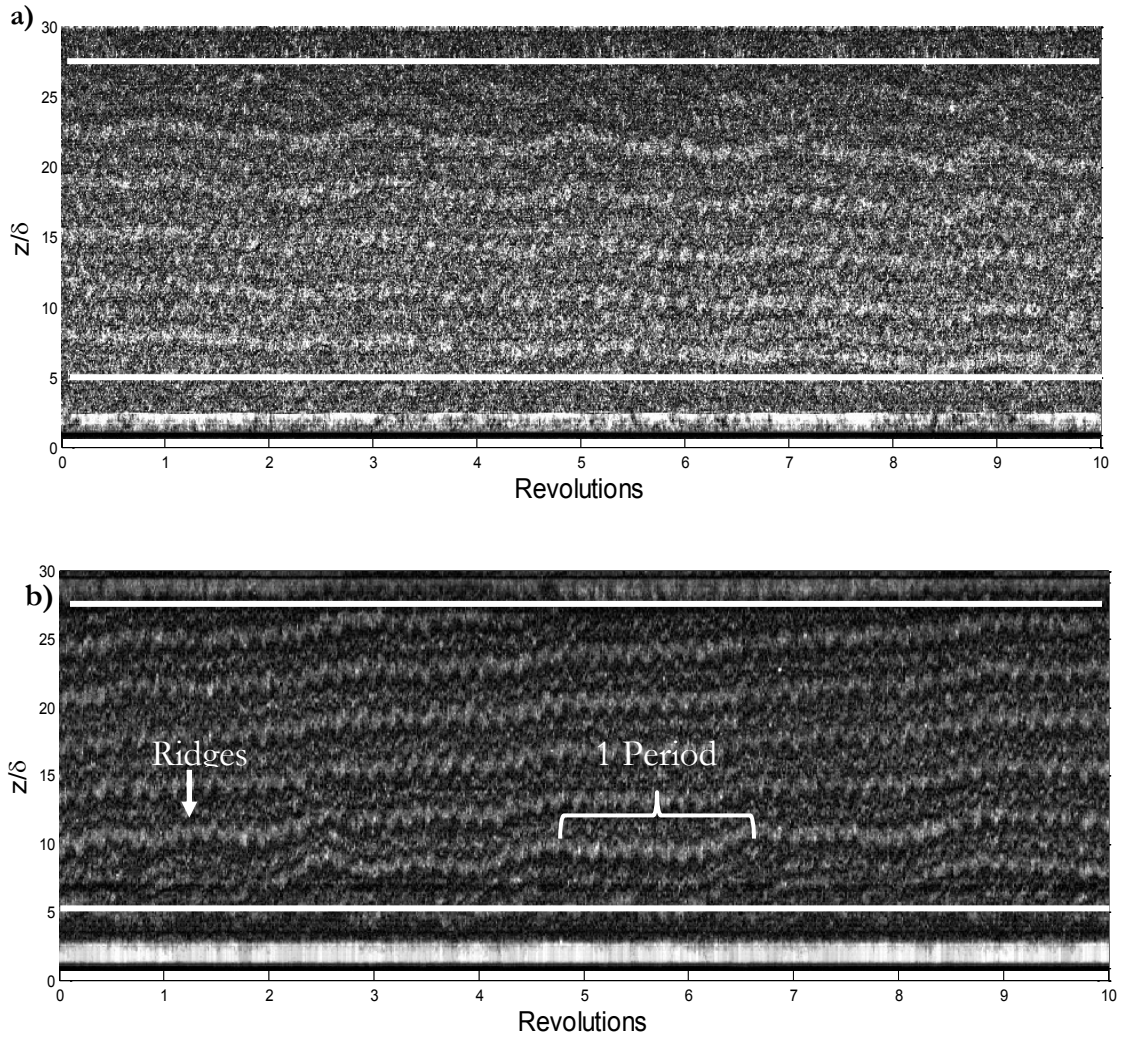

Figure 5.3. Space time plots for the B9-1-2 and B9-2-2 experiments, no through flow W_g=0 m/s and holding volume 0.42V_T. In the ordinate, the value 0δ corresponds to the bottom of the SFA, the abscissa shows markers for each revolution of the inner cylinder. a) Experiment B9-1-2, Re_θ=1110, total displayed record 0.7s. b) Experiment B9-2-2, Re_θ=2230, displayed time 0.34 s.

Figure 5.3a shows the temporal-spatial transformation for experiment B9-1-2. In the image, the various vortex rings move downward in the time domain. The plotted transformation also shows that the frequency oscillation of the vortices is half the rotation rate of the inner cylinder. The measurements of the vortex frequencies for the case Re_0=2230 shown in Figure 5.3, also indicate that on average, the vortex frequency is half of the rotation rate of the inner cylinder, or one oscillation every two revolutions.

The mean axial vortex velocity was calculated by finding the center of a vortex ring and measuring the slope. It was found that the vortex rings have similar slopes within the same Reynolds number for experiments between Re_0=1110 and Re_0=6360.

Table 5.2. Measured vortex axial velocity (W_v) at various Reynolds numbers and holding volume ratios

Re_0	$\left(\frac{Ta}{Ta_{cr}}\right)^{\frac{1}{2}}$	$\frac{W_V}{U_0}\times10^{-3}$	V_T
1113	6.0	-2.6	0.42
2226	12.1	4.8	
3190	17.2	6.5	
6360	34.5	6.2	
1113	6.0	8.9	0.54
2226	12.1	5.3	
3190	17.2	21.7	

It was noted that near the bottom and top edge of the impeller an incoherent region exists with no obvious vortices. These zones are called herein development regions, with variables λ_{Top} and λ_{Bottom} that correspond to the thickness of the top and bottom zones respectively. The white lines that span across the time domain in Figure 5.3a-b correspond to the length of the development regions. Adding these two wavelengths corresponds to the total end-cell length with variable λ_E. In the transformed images, it is shown that the zones have the same thickness throughout the acquisition time, and the Reynolds number has a small impact on the thickness of the cell. The temporal-spatial transformations for visualization images at other Reynolds numbers are shown in Appendix E. A plot with the thicknesses of development regions for various Reynolds numbers is shown in Figure 5.7.

In Figure 5.3b the average oscillation frequency of the vortices is 15.1 Hz ± 0.09 Hz. The plotted transformation also shows that between Re_0=1110 and Re_0=2230 the slope of the axial translation in time of the vortex pairs changes sign, indicating an upward movement. The average vortex pair axial velocity for various Reynolds numbers is shown in Table 5.2.

From the plots in Figure 5.3 it can be inferred that the average vortex pair wavelength and the number of vortex pairs may change with Reynolds number. In Table 5.3 it is shown the average cell wavelength and its response to both Reynolds and Taylor number. The table also shows the approximated finite-column wavelength $\boldsymbol{\lambda_{fi}}$.

$$\lambda_{fi}=\frac{H}{N_{cell}\delta}$$

In experiments, the finite column approximation differs from the theoretical wavelength that originates from stability analysis, since at the onset of instability, the wavelength of the cells must satisfy an integer number (N_{cell}) of vortex-pairs within the column height (H) and gap thickness (δ) (Koschmieder 1979, Burkhalter 1973).

Table 5.3. Experimental data obtained at various Reynolds numbers which corresponds to specific Taylor number ratios. The variable N_{cell}, corresponds to the number of vortex pairs. $\frac{\lambda}{\delta}$, is the measured wavelength over the gap thickness and λ_{fi} is the calculated wavelength for a fluid column of finite length. The data was collected in batch condition, W_g= 0 m/s

Holding volume	Re_0	$\left(\frac{Ta}{Ta_{cr}}\right)^{\frac{1}{2}}$	N_{cell}	$\frac{\lambda}{\delta}$	λ_{fi}
$0.42V_T$	1110	6.0	6.0	3.7	4.6
	2230	12.1	6.0	3.71	4.6
	3190	17.2	5.0	4.0	5.5
	6360	34.5	5.0	4.1	5.5
$0.54V_T$	1110	6.0	6.0	3.4	4.6
	2230	12.1	5.0	3.9	5.5
	3190	17.2	5.0	3.7	5.5

Table 5.3 contains experimental data for two holding volumes; it shows that by increasing Reynolds number the number of Taylor cells decreases slightly within the experiment boundaries, this occurs for both holding volumes. It also shows that after Re_0=3190 and Re_0=2230 for $0.42V_T$ and $0.54V_T$ respectively, the number of vortex pairs appear to stay constant. This is reflected in the finite column approximation for both holding volume

ratios. Figure 5.4 compares the calculated wavelength λ_{fi} for SFA experiments at $0.42V_T$ and $0.54V_T$ with data obtained from experiments by Koschmeider 73, and Burkhalter 79.

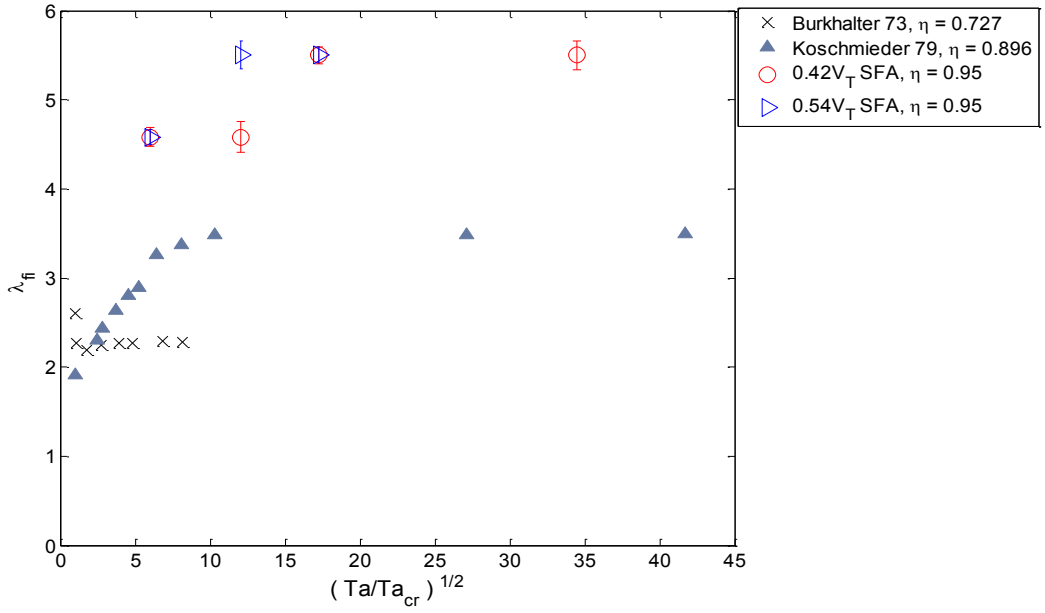

Figure 5.4. The plot compares the calculated wavelength for a finite column apparatus λ_{fi} to data from literature at various Taylor numbers. Ta_{cr} corresponds to the critical Taylor number value, also the experiments were carried out such that the inner cylinder rotates and the outer is held stationary. (x) Data extracted from Burkhalter, 73. The aspect ratio was η=0.727 with an open free boundary on top of the apparatus. (▲) correspond to data extracted from Koschmieder, 79. With aspect ratio of η=0.896. (○)SFA with $0.42V_T$ and W_g =0 m/s, η=0.95. (▷) SFA data for holding volume of $0.54V_T$, W_g =0 m/s and η=0.95.

In Figure 5.4 the plotted data for Burkhalter 73, corresponds to an experiment where the upper boundary is disconnected from the inner cylinder similar to the SFA, which creates a free surface at the top of the apparatus. The length of the space between the inner cylinder and the upper surface of the apparatus is 0.58δ in Burkhalter 73, whereas in comparison this length in the SFA is ~5δ.

The plotted data for Koschmieder 79, corresponds to an apparatus where the upper and lower boundaries (plates) were held stationary. However, the space between the inner cylinder and these boundaries was kept to a minimum such that it did not create a free surface between the upper plate and the inner cylinder.

Figure 5.4 shows that for values of $\left(\frac{Ta}{Ta_{cr}}\right)^{\frac{1}{2}}$ =7 and above, as the radius ratio (η) is increased, so is wavelength λ_{fi}. In the plot, the data from Koschmeider indicates that the finite column wavelength λ_{fi} increases with Taylor number showing an asymptotic behavior at high Taylor numbers. Although it appears that a similar behavior is observed to occur for the SFA data at $0.54V_T$, in which after $\left(\frac{Ta}{Ta_{cr}}\right)^{\frac{1}{2}}$ =10 the value of λ_{fi} is constant. The collected data shows a limited range of Taylor numbers. The plot also indicates that at $\left(\frac{Ta}{Ta_{cr}}\right)^{\frac{1}{2}}$ =7 and $\left(\frac{Ta}{Ta_{cr}}\right)^{\frac{1}{2}}$ =12 the calculated wavelength λ_{fi} is larger at the higher holding volume.

The plot data in Figure 5.4 shows that the calculated wavelength based on the number of vortex pairs is affected by Taylor number. It is seen that λ_{fi} in the SFA increases with Taylor number within a certain range, which is also observed in literature (Koschmieder 1979, Burkhalter 1973, Di Prima, Swinney 1985, Coles 1965).

The wavelength of a vortex pair as defined by λ, is the average thickness of two counter rotating vortices, which differs from λ_{fi} that takes into account the number of vortex pairs in the liquid column. Therefore, λ is the simplest measurement of the wavelength of Taylor vortices available. The effect of the holding volume on the value of λ is analyzed in Figure 5.5. The plot shows the vortex pair wavelength normalized by the gap thickness δ.

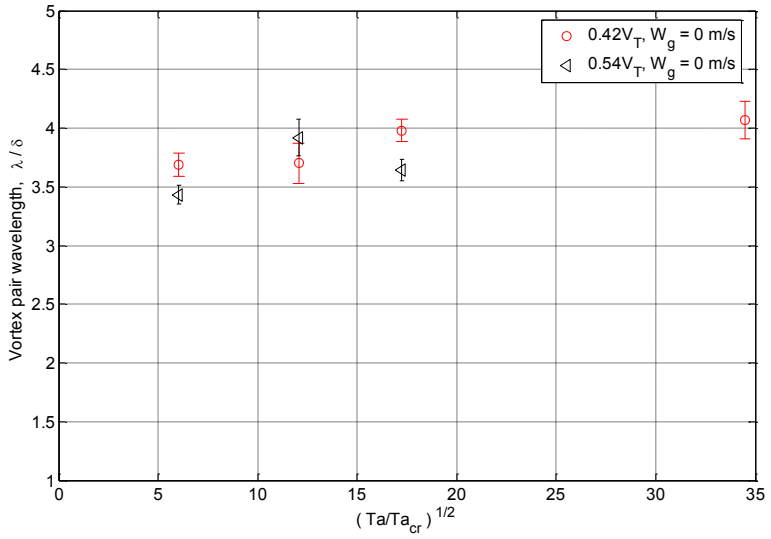

Figure 5.5. Plot of the response of the normalized average vortex pair wavelength to Taylor number in batch condition, W_g=0 m/s. Marker (○) shows points for holding volume of 0.42V_T. Marker (◁) shows points for holding volume 0.54V_T.

For Figure 5.5, the plotted data corresponding to 0.42V_T indicates that by increasing the Taylor number, the wavelength of the vortex may increase slightly for this condition. The collected data points for 0.54V_T do not show an obvious trend. However, to assess the response to Taylor number for the 0.54V_T holding volume case, further points at higher Taylor numbers are required.

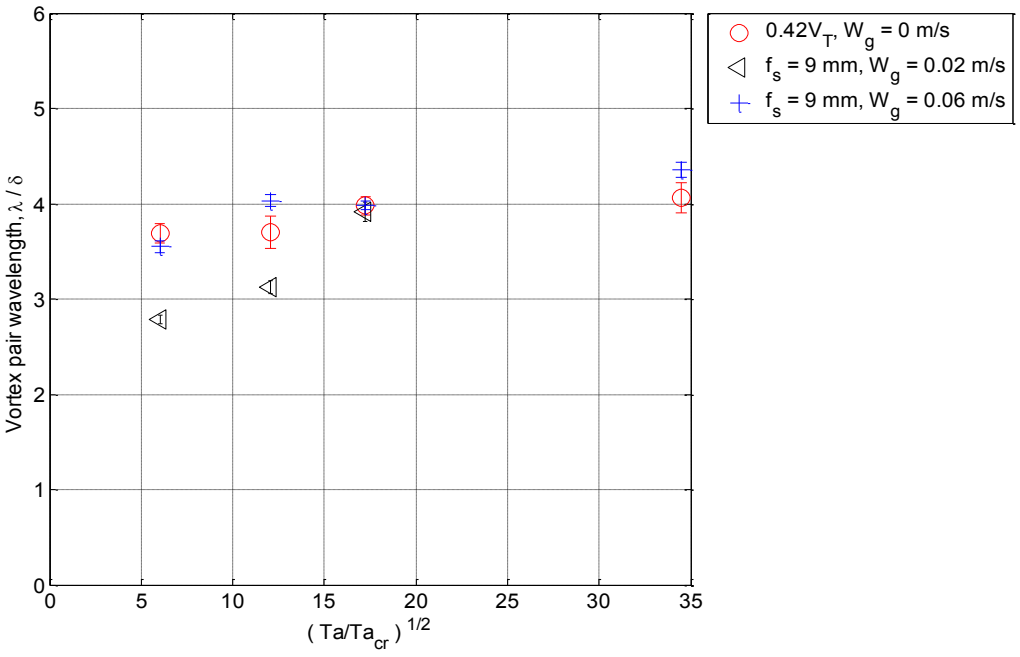

Figure 5.6. The plot compares the vortex pair wavelength at various through flow conditions, and their response to Taylor number. (○) Shows the vortex wavelength for $0.42V_T$, W_g=0 m/s (no axial flow). (◁) is for axial through flow of W_g=0.02 m/s and upper plate of 9 mm. (+) corresponds to the highest axial through flow, W_g = 0.06 m/s and upper plate of 9 mm. The uncertainty bars are shown in red for all markers.

The characterized wavelength in batch condition for $0.42V_T$, where no through flow is present indicates that the vortex wavelength increases slightly with Taylor number. The behavior of said wavelength λ for a condition with axial through flow is shown in Figure 5.6.

The data shows that in throughflow, at Taylor numbers $\left(\frac{Ta}{Ta_{cr}}\right)^{\frac{1}{2}} = 5 - 17$, the wavelength λ is slightly affected by the presence of axial flow. At W_g=0.02 m/s, the wavelength is observed to increase ever so slightly until it reaches a similar length scale as in the batch condition. At the higher axial flow condition it was observed that the vortex pair wavelength is similar as in the batch case.

5.2. Development zones of vortices above, below gap.

It was observed in Figure 5.3 that near the upper and lower edges of the inner cylinder, there is an area of non-structured flow when compared to the Taylor cells. As was described previously in section 5.1, these regions correspond to variables λ_{Top} and λ_{Bottom}. The length of the development zone is measured from the edge of the inner cylinder to the nearest axial point next to a Taylor vortex within the liquid column. The total length of the development region is taken as the sum of the top and bottom zones, corresponding to the variable λ_E; first used by Burkhalter, 73.

In plot a) of Figure 5.7, the end cell wavelength λ_E for $0.42V_T$ and $0.54V_T$ is compared to data obtained by Burkhalter 73 using an apparatus with η=0.727 and a free boundary atop of the inner cylinder.

The plotted data of λ_E for the SFA at both holding volumes, indicate that the thickness of the development zones increases with Taylor number, which is in agreement with literature. The plotted data in a) also shows that the λ_E is slightly larger with smaller holding volume ($0.42V_T$). However, the uncertainties of the measurements for these conditions indicate that the response of λ_E to holding volume is small.

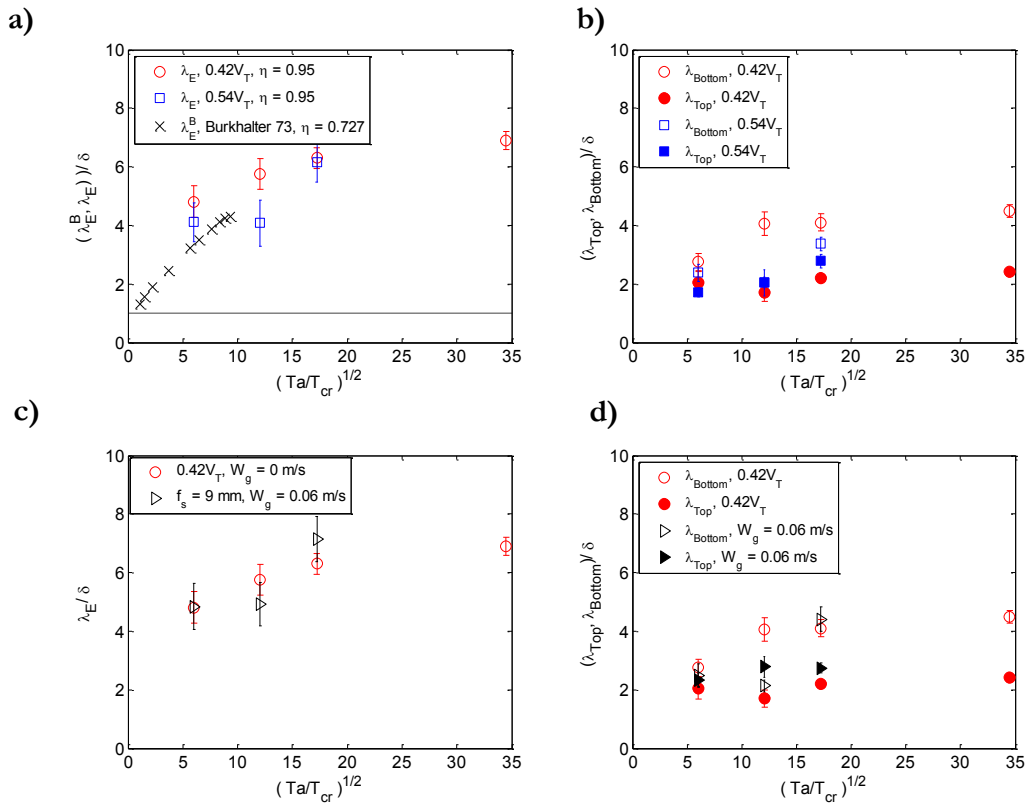

Figure 5.7. Comparative plots for the response of the end cells to Taylor number at various holding volumes and through flow conditions, the end cell wavelength is normalized by the gap thickness δ. In plot a), λ_E and λ_E^B is the end cell for the SFA and for Burkhalter, 73 respectively; and, there is no axial flow W_g=0 m/s. Markers (○)for holding volume 0.42V_T and (□)for holding volume 0.54V_T. (*x*) corresponds to data extracted from Burhkhalter 73, specifically for the case with open free boundary at the top of the apparatus. The dashed line indicates a wavelength equal to the length of the gap. Plot b), shows the length of the bottom and upper development regions λ_{Bottom} and λ_{Top} respectively. Circles (○,●) are for 0.42V_T and λ_{Bottom}, λ_{Top} respectively. Squares (□,■) are for 0.54V_T and λ_{Bottom}, λ_{Top} respectively. Plot c) Shows λ_E for W_g=0 m/s and W_g=0.06 m/s. (○) corresponds to holding volume 0.42V_T, (▷) is for f_s = 9 mm and W_g=0.06 m/s. Plot d), markers (○,●) are for 0.42V_T, and λ_{Bottom}, λ_{Top} respectively. Markers (▷, ▶) are for f_s = 9 mm and W_g=0.06 m/s

Figure 5.7b, shows that on average, the length of the development region at the bottom of the inner cylinder is larger than the one located at the top of the impeller. The plotted data also shows that the values of λ_{Bottom} are longer for the 0.42V_T case. The length of the region of unstructured flow at the top of the impeller λ_{Top} is observed to be about the same magnitude for both holding volumes.

To consider the length of the total development zone in the SFA with an imposed axial through flow, the data was plotted in c). In the plot, the axial flow is 0.06 m/s for the throughflow condition, with an upper plate thickness of 9 mm. The width of the spinning film for this upper plate, corresponds to an equivalent of $0.42V_T$ in the batch condition. The resulting plot indicates that as in the batch mode, the length of the development zones λ_E increases with Taylor number. The plotted data also suggests that the major axial flow does not change λ_E significantly. In plot d), the thickness of the development zones for the case with axial flow shows that λ_{Bottom} and smaller than λ_{Top} are both the same, unlike for the $0.42V_T$ case.

5.3. Oscillation frequency of vortices

At the regimes that the SFA is operated throughout the experiments shown in this manuscript, the Taylor vortices are shown to exhibit some oscillation. The oscillation of the vortices is evident in the spatial-temporal plots in Figure 5.3. The plotted data for both Reynolds numbers show small ridges with a higher frequency than the frequency of the vortices, in the time plots (t-z). The ridges are an artifact of the temporal-spatial transformation and not part of the flow.

In Figure 5.8, the measured average oscillation frequency of the Taylor vortices ($f_{Ta\ vortex}$) is normalized by the inner cylinder rotation frequency. The plotted data in a), contains information on the frequency for the batch conditions of $0.42V_T$ and $0.54V_T$. The measured frequency shows that for $0.42V_T$ the vortex oscillation frequency is maintained at half the frequency of the impeller, whereas for $0.54V_T$ response shows fluctuations at various Taylor numbers. The measured frequency shows that changing the holding volume of the liquid within the SFA is reflected on the characteristic frequency of the vortices.

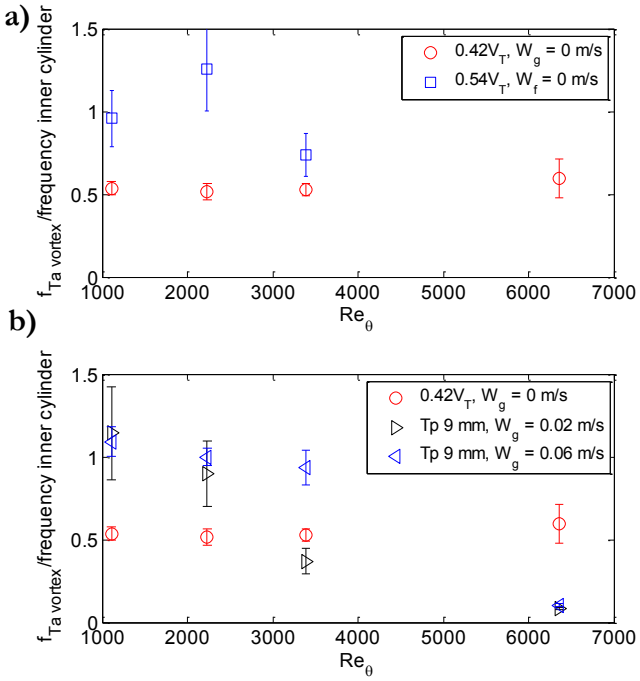

Figure 5.8. Plots of the normalized average Taylor vortex frequency using the frequency of the inner cylinder. The plots show data for the batch and continuous flow conditions (f_s = 9 mm). $f_{Ta\ vortex}$ is the average frequency of the Taylor vortices. a) W_g=0 m/s, shows Taylor vortex frequency for (○) 0.42V_T holding volume and (□) 0.54V_T holding volume. In b), the data compares (○) 0.42V_T, with W_g= 0 m/s, (▷) axial flow W_g = 0.02 m/s, f_s = 9 mm and, (◁) axial flow W_g = 0.06 m/s, f_s = 9 mm.

The measured frequencies when axial flow is present are shown in plot 5.8b. The data is compared to the batch condition with 0.42V_T. The plot shows that the Taylor vortex oscillation frequency with axial flow is inversely proportional to Reynolds number. In Figure 5.8b, for the range of Reynolds number studied the plotted data for both axial flow conditions have similar normalized frequencies at both the smallest and largest Reynolds numbers. The normalized frequency is also matched at Re_0 =2230, before rapidly decreasing for the W_g= 0.02 m/s case, at Re_0=3190 with 0.4 frequency of the inner cylinder.

5.4. PIV: Gap, and secondary flow

Single plane PIV was performed to obtain velocity statistics in the gap, underneath and above the impeller. The data was collected in the (r,z) planes, the particles moving tangential to the **r** axis correspond to the $\mathbf{V_r}$ velocity, and the particles moving relative to the **z** plane correspond to the **W** velocity. The radial velocity V_r, and the **r** axis point toward the central axis of the system, and r=0 is located at the outer wall. The velocity statistics hereby presented were normalized using the azimuthal tip velocity of the inner cylinder U_0, as shown in Figure 5.9.

In Figure 5.9, the instantaneous contour fields in this plot were generated by cross-correlating the particle displacement between two images separated by 333 μs. In plot a, the contours of the axial velocity show a weak signature of Taylor vortices in the gap. The vortices can be seen as alternating downward and upward velocity packets along the axial axis. The plotted contours beneath the impeller, in the region underneath the gap (radial positions between 0δ - 1δ) in the plot, show a downward flow near the outer cylinder wall at the bottom corner of the apparatus. The direction of the axial velocity changes to an upward flow as the radial distance is increased (toward the axial center).

The instantaneous contour fields in Figure 5.9, show the prevalence of edge effects in both velocity components caused by the inner cylinder; the corner of the inner cylinder is located at a distance of 1δ radially and 2.5δ axially. The radial velocity (shown in plot b) shows a stronger magnitude ($-0.11U_0$) at the locations of (1δ, 2.1δ) near the impeller, which pushes the fluid towards the outer cylinder wall.

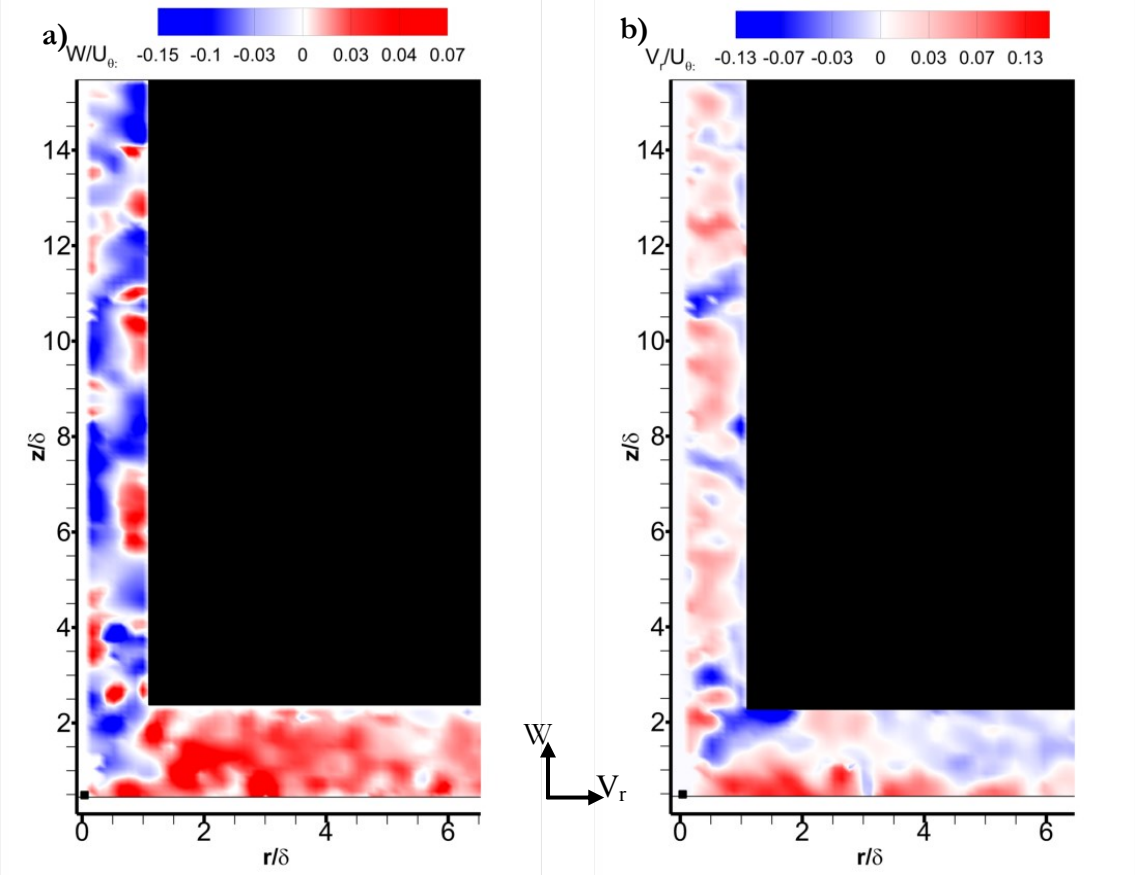

Figure 5.9. Experiment B9-1-3.The plots contains instantaneous contours showing the axial and radial velocities at the bottom corner of the SFA. a) Shows the normalized measured axial velocity W/U_θ. b) Normalized radial measured velocity Vr/U_θ. The black rectangle corresponds to the inner cylinder.

In section 5.4 it was shown that vortex pairs experience an axial translation in the liquid column in the gap. If field averages were to be taken over long times, the translation of the vortices will cause smearing on the contour plots. Therefore, the vortex axial translation velocity W_v was used as a ballpark approximation of the distance traveled of a vortex cell between average fields. The contour and vector fields presented in this section correspond to averages over various instantaneous data sets. This operation was performed in order to resolve the vortex structures that arise in the gap of the SFA.

Table 5.4. Shows the percentage of the thickness of a vortex pair used for averaging PIV fields.

Experiment	Vortex axial velocity, W_v $[1\times10^{-3}]$	Fields used for average	Acquisition frame rate	Percentage displaced of λ	Distance traveled by vortex cell
B9-1-3	9.6	100	3000	8%	0.15δ
B9-2-4	4.8	30	4000	7%	0.12δ

In Table 5.4 the second column shows the normalized vortex pair axial velocity, which was obtained by flow visualization. The fifth column shows the percentage of the thickness of one vortex pair used for averaging the PIV fields. The average fields were obtained using the number of frames N_{frames}, vortex axial velocity W_v and frame rate F as means of approximating the distance traveled by a vortex pair.

$$\text{ratio of } \lambda \text{ displaced} = \frac{NW_v}{F\lambda}$$

The wavelength of the vortex pair δ correspond to length scale of travel. In the case of batch condition at Re_0=1110, 100 fields spaced at 333 μs were used to create the average field.

In the gap in Figure 5.10a, the vortex signatures are observed between the inner and outer cylinders. In the plots, a vortex signature consists on an area of fluid containing a preferred direction as shown by the vectors, next to a neighboring the area (above or underneath) which has an opposite direction of motion. These packets of fluid are observed to be circular as seen in Figure 5.10a. Through PIV on the (r,z) axis, we are now able to resolve a section of the vortex cell positioned closer to the inner cylinder, which was not visible in flow visualization.

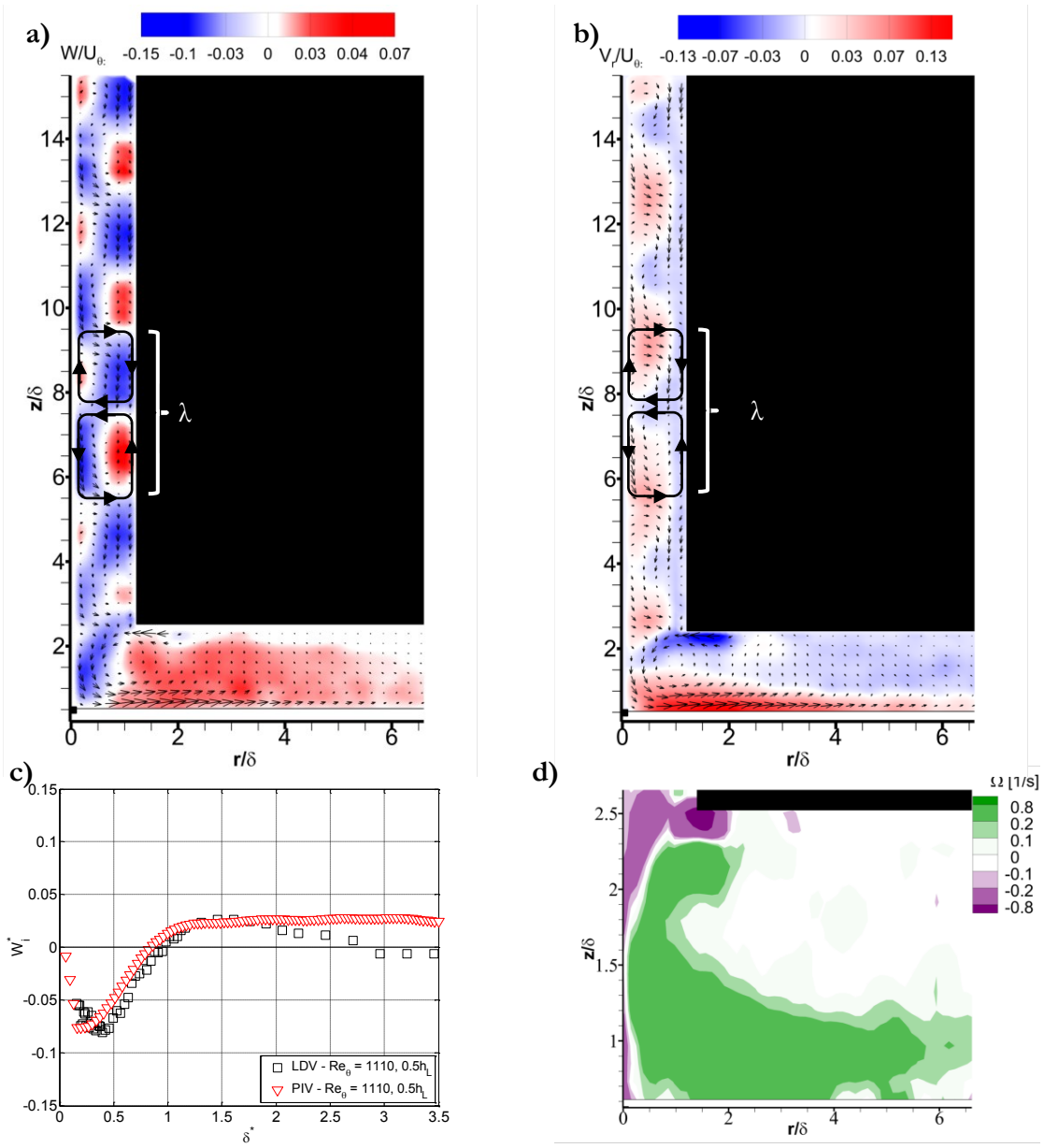

Figure 5.10. Experiment B9-1-3, Re_θ=1110, W_g=0 m/s. Plots a, b and d, show the averaged vector fields at the bottom corner of the apparatus. a) Averaged vector field of the normalized axial velocity. b) Normalized averaged vector field for the radial velocity. c) Comparative plot for data obtained at 0.5h_L both in PIV and LDV at Re_θ=1110. Data for LDV corresponds to (□) in Figure 4.16. d) Expanded view of the bottom corner of the apparatus. Plotted is the (r-z) vorticity is in units of 1/s, positive vorticity goes out of page towards reader.

A flow feature that arises from the data presented in Figure 5.10a corresponds to the average shape of the vortex cells, a vortex cell is one half the wavelength of a vortex pair. The part of a vortex cell with a downward velocity appears to have a beveled rectangular

shape. On the other hand, for the part of the vortices with an upward velocity at the same axial location, the cells shape is close to a circle surrounded by a small axial velocity near W= 0 m/s according to the plotted contours. It was observed that the combined length of the vortex cell with mean upward flow, and the surrounding fluid of zero axial velocity have the same length as the section of the vortex with negative (downward velocity). In plot b of Figure 5.10, near the bottom surface, the radial velocity has a positive direction, with an inward motion towards the center of the apparatus. The measured radial velocity at a height of 0.5δ is observed to decay monotonically towards the axial center.

The vortex cell section that are located at similar axial positions but with two different radial locations (near outer/inner cylinder). Moreover, in plot a, the bracket attempts to show the length scale of a single vortex pair. The change in velocity between vortex cells at the same height is also observed in plot b, in Figure 5.10. The direction of the radial velocity is inverted at a similar axial location, which helped to identify the signal of a Taylor vortex as it is shown in (Akonour, Lueptow 2003, Tokgoz, Elsinga et al. 2012, Wereley, Lueptow 1998, Taylor 1935).

Figure 5.11 shows the contours of the (r,z) vorticity for the same fields. From the direction of rotation of the vorticity we can observe the length of the vortex cells, and therefore estimate the size of a vortex pair. Using this method, the average vortex pair wavelength for Re_{θ}=1110 in the batch condition is 3.3δ, whereas in flow visualization it was found that the mean wavelength was ~3.7δ at this condition.

Underneath the impeller where a secondary flow was first observed in Section 4, we compare the results obtained by LDV with PIV in Figure 5.10c. The plot shows a close match between both data sets, validating the existence and presence of a sustained rotation in the bottom lower corner of the SFA. The flow is observed to circulate with a downward motion near the stationary wall. Near the intersection between the bottom surface and the wall, the boundaries change the flow direction upward and radially towards the center of apparatus. The observed upward flow in plots c, is also implied in plot d, where the contours of the (r,z) vorticity are shown.

Near the edge of the inner cylinder, at a radial location 1δ and height 2.5δ, the magnitude of the calculated vorticity Ω is at its highest, with a negative direction. The value of the measured vorticity at this position is tangential to the direction of rotation of the inner cylinder..

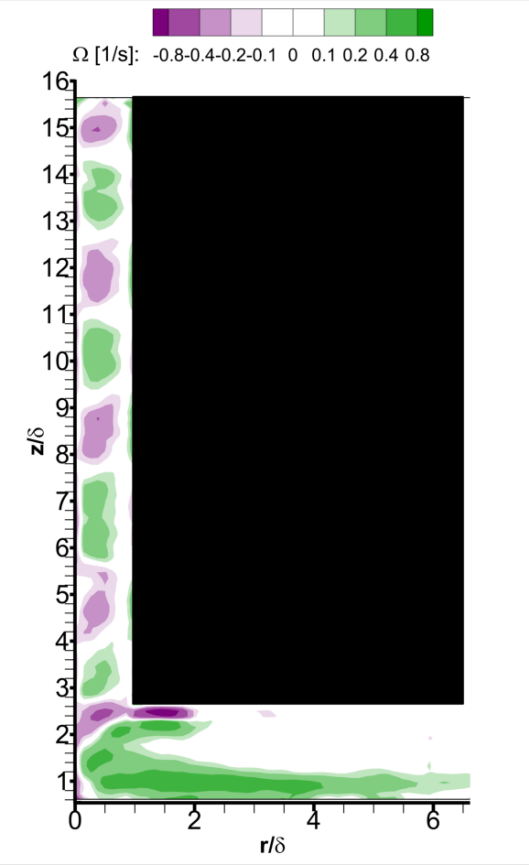

Figure 5.11. Contours of the (r,z) vorticity Ω at the bottom corner of the SFA for experiment B9-1-3, Reθ=1110. The holding volume is 0.42V_T and W_g=0 m/s.

For the dynamic condition where Re_θ=2230 and W_g=0 m/s, the recorded fields near the bottom corner of the apparatus also show the presence of a vortex with counter clockwise rotation. The downward velocity at the corner of the SFA in Figure 5.12a, shows that at 0.4δ radially and at a height of 1.1δ, W= 0.14U_θ. The measured radial velocity is observed to be positive and with high magnitude when near the bottom of the apparatus, similar as in the case of Re_θ=1110.

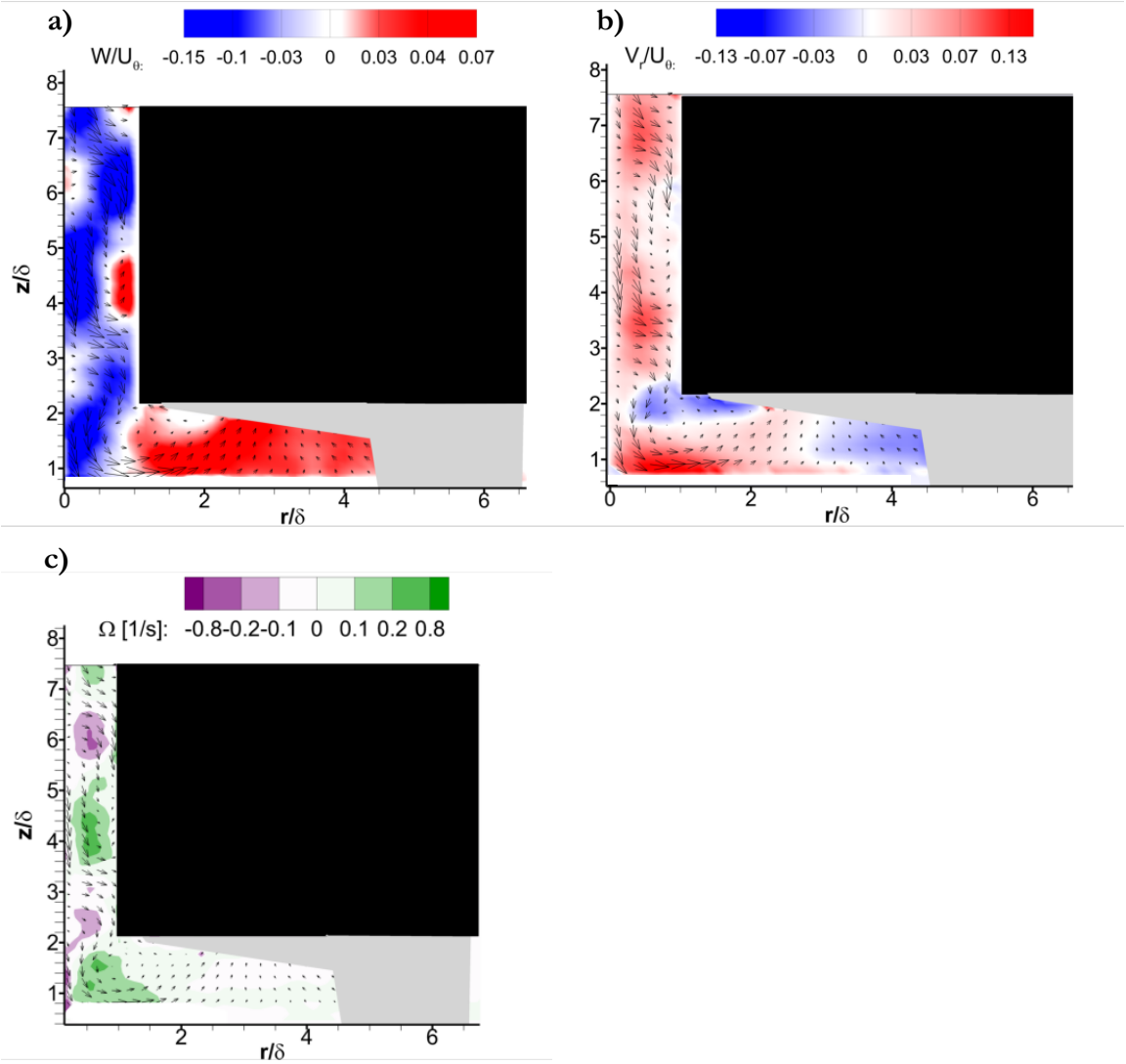

Figure 5.12. Lower section of experiment B9-2-4, for Re_θ=2230 and W_g=0 m/s. The plots show the averaged vector fields for the axial and radial velocity at the bottom corner. a) Normalized average measured axial velocity W within the SFA. b) Normalized radial velocity V_r. The gray sections correspond to locations where data was compromised due to the free boundary and limited illumination. c) contour plot of the (r,z) vorticity Ω (1/s).

Figure 5.12 also shows a faster decay of the positive V_r component towards the center of the apparatus than in the lower Reynolds number case. However, at similar radial positions, the axial velocity has a larger magnitude in the upward direction near the impeller for Re_θ=2230. This location was not accessible through LDV due the inner cylinder acting as a barrier for one of the laser beams, for example at radial location r/δ=2.2 and axial position z/δ=1.8.

In Section 5.2, the development zones were discussed. There, it was suggested that near the upper and lower corners of the inner cylinder, no Taylor vortices were present. However, these regions are not clearly present for the lower edges in Figure 5.10 and Figure 5.12, at Re_θ=1110 and 2230. The plotted data for the vorticity in these regions show circulating vortices with a Taylor vortex signature, whereas in flow visualization these regions seemed featureless.

5.5. PIV: Upper corner

Through visual inspection, the space atop the inner cylinder near the upper plate was observed to generate a spinning film, both in batch and with an imposed axial flow. The thickness of the film is thought to vary according the holding volume (in batch mode), and with respect of the thickness of upper plate in continuous mode (when $W_g \neq 0$ m/s); similar as the one generated at the bottom of the apparatus. Figure 5.13 contains average contours of the axial, and radial velocities, also showing the (r,z) vorticty of the upper corner of the SFA. The data was obtained at W_g=0 m/s, Re_θ=1110 and $0.3V_T$. The data are cut off at the liquid free boundary.

Above the impeller, the plotted data shows a high axial upward component near the outer cylinder wall, as seen in plot a. At the upper corner of the impeller, the flow has a outward radial velocity of about $0.14U_0$ driving the flow from 1.5δ (radially) towards the outer cylinder. Then, an upward flow originated from the gap drives fluid towards the upper corner of the apparatus. Once the flow encounters the upper corner, it changes direction turning into the inward radial direction, which ultimately moves downwards generating a vortex. The free boundary creates a physical barrier that limits the width of the vortex. Moreover, the plotted data shows that at $0.42V_{T,}$ the thickness of the free boundary is 2.5δ at the upper stationary surface (upper plate), which is smaller than the measured bottom free surface for a similar Reynolds number and holding volume fraction. In the gap, the vorticity contours show that the average vortex pair λ is 3.6δ. The wavelength for the data obtained near the upper section shows similar magnitude as in Figure 5.11 as expected.

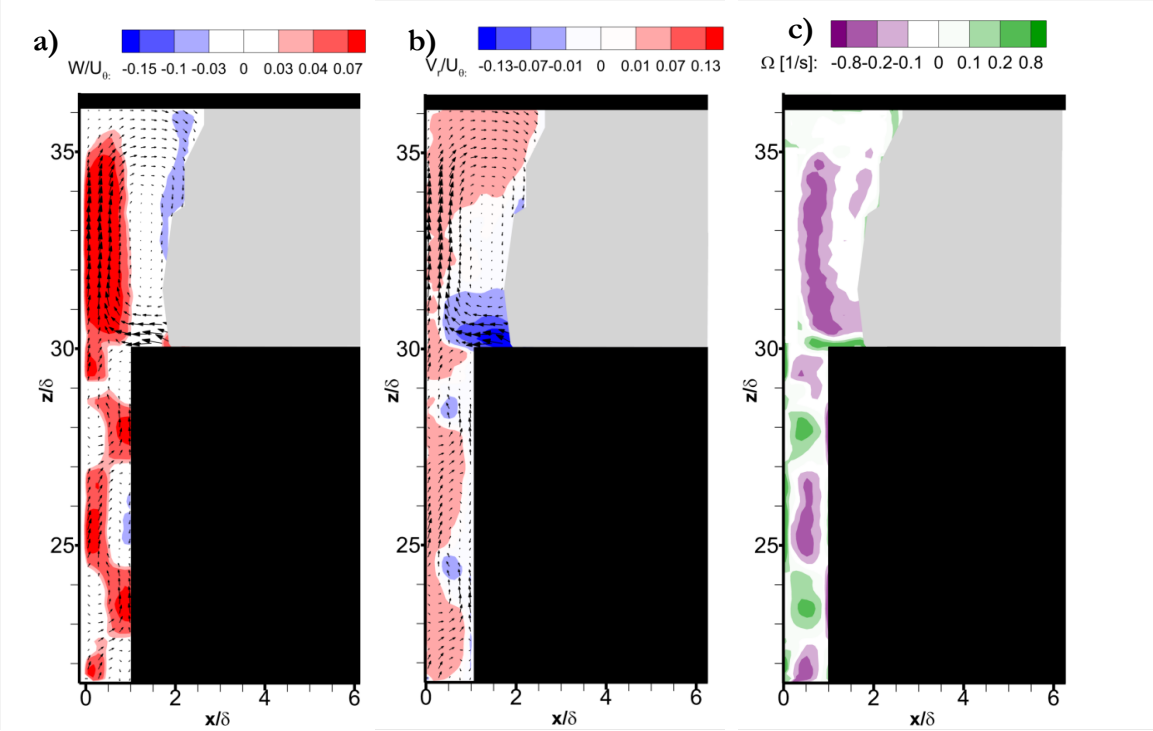

Figure 5.13. Normalized axial and radial velocities for Re_{θ}=1110, Wg=0 m/s, 0.42V_T; run B9-1-3. a) Plotted contours of the average normalized axial velocity $\frac{W}{U_{\theta}}$ in the upper corner of the SFA. b) Plotted contours of the average normalized radial velocity $\frac{V_r}{U_{\theta}}$. c) Contours of the (r,z) vorticity Ω [1/s].

As was described in Chapter 1, to replicate the volume fraction and the free boundary in the continuous mode where W_g>0, the upper plate was reduced in width. This allows the liquid to move around the upper plate, ultimately leaving the SFA through the outlet port as shown in Figure 2.2. The mechanism by which fluid leaves the chamber where the inner cylinder rotates is seen in Figure 5.14. In the plots, a large upward flow can be observed away from the upper plate from the axial velocity contours. The plotted data also shows that the flow moves radially inward (toward the center of the apparatus) near the upper plate.

In the axial velocity plot for Figure 5.14, the contours indicate an upward motion near the outer cylinder wall, neighboring a mean downward flow region radially inward, similar as

in the batch condition. However, in the case with axial flow and W_g = 0.06 m/s, the free boundary is moved inward to a location of 7δ (not plotted). In Figure 5.14 the vortices shown by the vorticity contours indicate that the average vortex pair wavelength λ is ~3.3δ, based on a limited field of view.

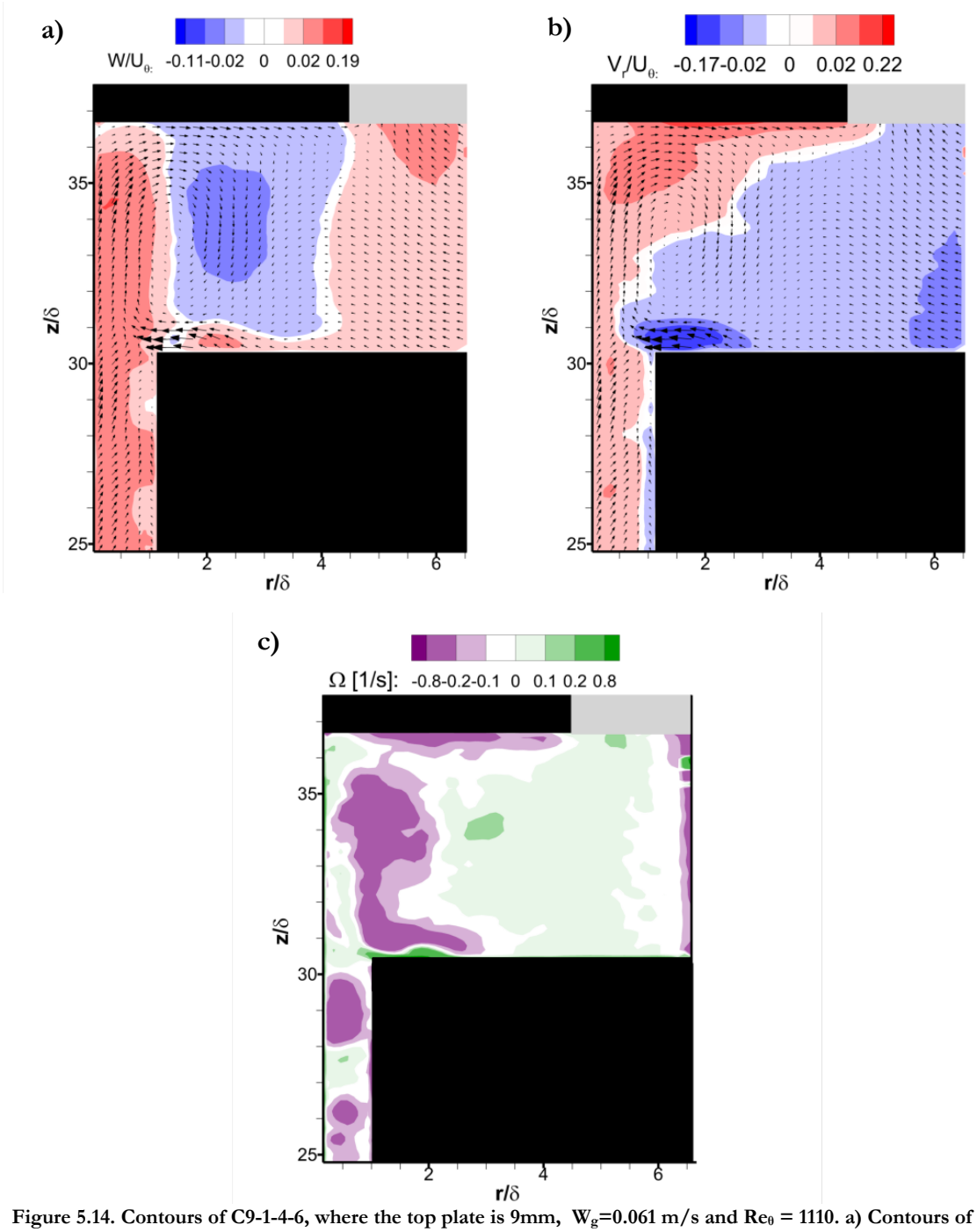

Figure 5.14. Contours of C9-1-4-6, where the top plate is 9mm, W_g=0.061 m/s and Re_θ = 1110. a) Contours of the normalized axial velocity. b) contours of the normalized radial velocity.The grey area at radial position~4.5δ and

height 36.8δ corresponds to flow leaving the chamber into the upper section before being discharged through the outlet port. c) Contours of the (r,z) vorticity in the upper section of the SFA. The upper plate is represented by a black rectangle extending to 4.5δ (9 mm) in the radial direction.

The flow atop the inner cylinder in the batch case shows the existence of a vortex near the upper corner of the apparatus. A similar phenomenon is observed for the case of axial through flow with Top plate of 9mm and W_g = 0.06 m/s. It was also observed that the distance from the air/water interface to the outer cylinder wall increased with the addition of axial flow. The length of the boundary was found substantially larger than the thickness of the upper plate. The response of the free boundary to both upper plate thickness and the average velocity of flow in the gap, is evaluated in Figure 5.15 and Figure 5.16

Similar as in the case with f_s=9 mm, the plotted data for the normalized axial velocity for f_s= 6 mm and 12 mm in Figure 5.15, shows the presence of a vortex between the upper plate and the inner cylinder. The plots also show regions were the flow moves upward, best observed in the W_g=0.06 m/s cases, for both upper plate thicknesses. This upward flow occurs between two regions of downflow. The first region is caused by the stationary vortex previously discussed, which has a clockwise rotation as seen in Figure 5.14c. The second region with nominally downward flow is near the free boundary.

While comparing the results for f_s= 6 mm and 12 mm, the length of the free boundary at the height of the upper plate is observed to increase with axial flow. It was found that the free boundary at this location is ~1.2δ larger at W_g=0.06 m/s than with the lower flow rate.

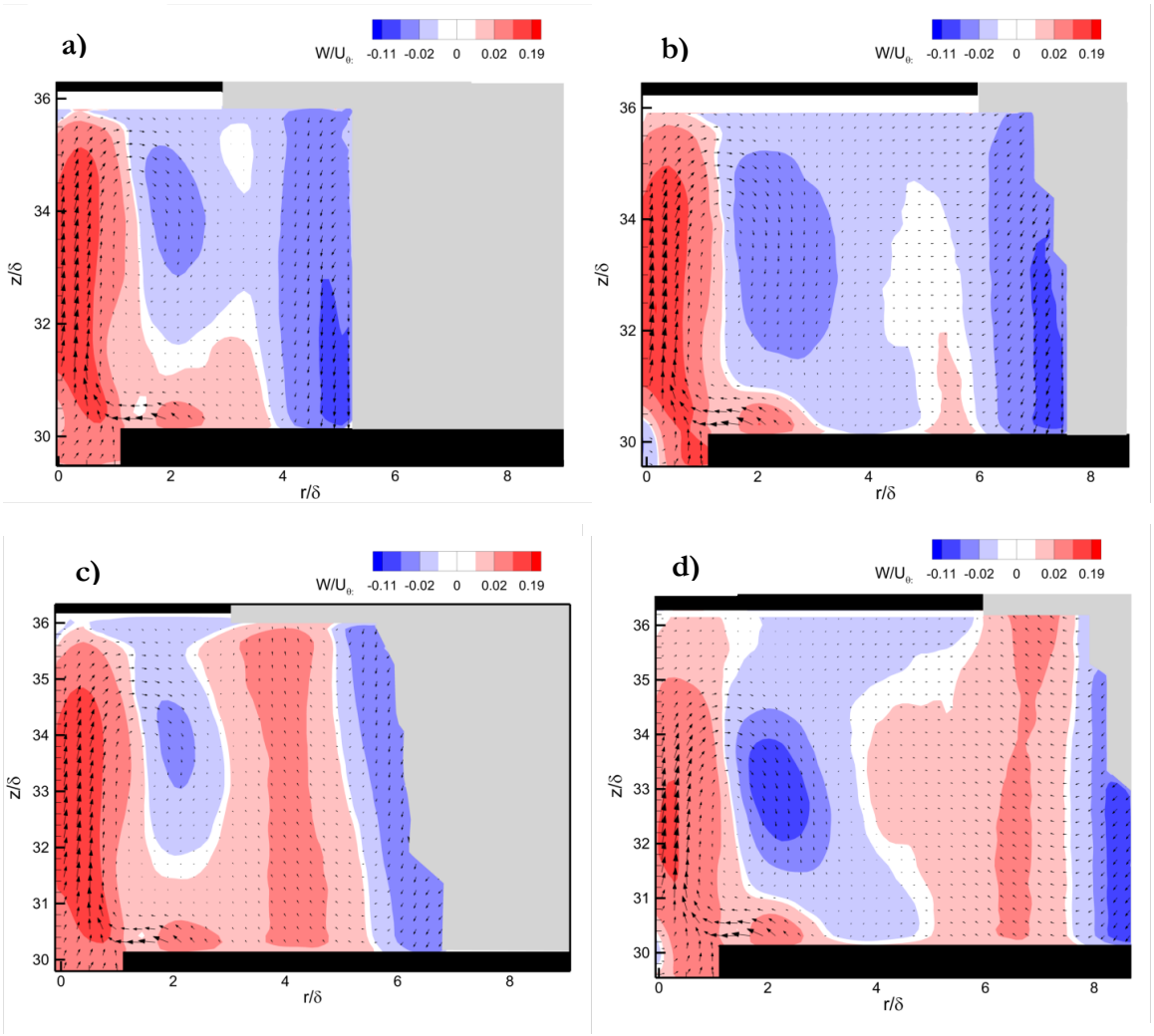

Figure 5.15. Contour plots of the normalized axial velocity for cases with axial through flow and various upper plate widths. a) case C6-1-4-1 with axial through flow W_g=0.014 m/s, Re_θ=1110 and f_s=6 mm. b) case C12-1-4-1 with axial through flow W_g=0.014 m/s, Re_θ=1110 and Tp=12 mm. c) case C6-1-4-6 with axial through flow W_g=0.06 m/s, Re_θ=1110 and f_s =6 mm. d) case C12-1-4-6 with axial through flow W_g=0.06 m/s, Re_θ=1110 and f_s =12 mm.

The radial velocity contours for various through flows and upper plate thicknesses shown in Figure 5.16 indicate similar patterns as in Figure 5.14, where the upper plate thickness was 9 mm. In the plots where f_s=6 mm, the radial velocity near the upper plate is inward up to the edge of the upper plate, clearly observed in Figure 5.17.

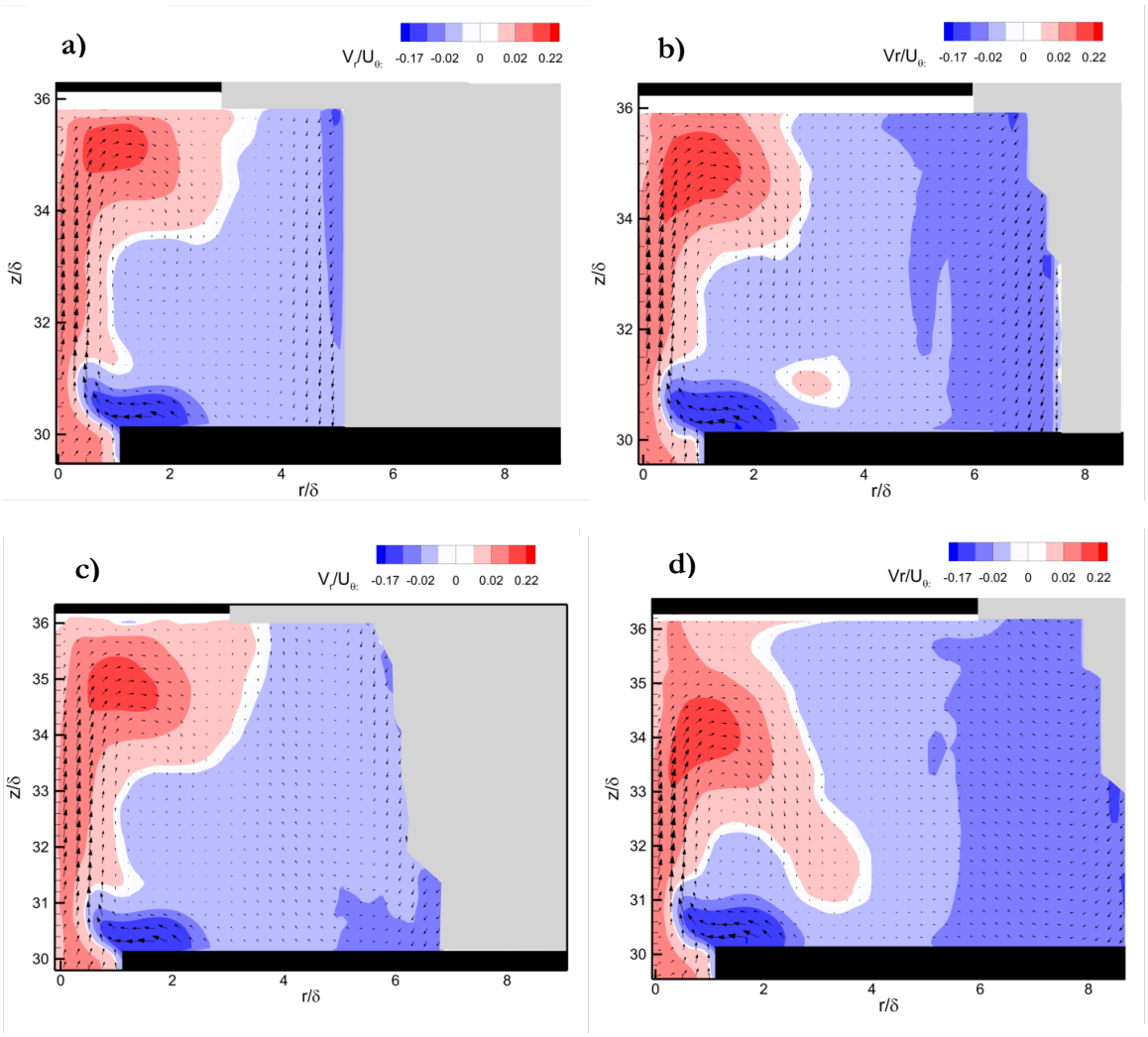

Figure 5.16. Contour plots of the normalized radial velocity for cases with axial through flow and various upper plate widths. a) case C6-1-4-1 with axial through flow W_g=0.014 m/s, Re_θ=1110 and f_s =6 mm. b) case C12-1-4-1 with axial through flow W_g=0.014 m/s, Re_θ=1110 and f_s =12 mm. c) case C6-1-4-6 with axial through flow W_g=0.06 m/s, Re_θ=1110 and f_s =6 mm. d) case C12-1-4-6 with axial through flow W_g=0.06 m/s, Re_θ=1110 and f_s =12 mm.

The flow moves towards the axial center as seen in Figure 5.16 and Figure 5.17. In the latter, the data was obtained by performing single plane PIV using fluorescent particles at the upper corner of the apparatus. The contours show that at the edge of the upper plate, a significant gradient in the radial velocity occurs. The radial velocity decays from $0.18U_0$ to $0.02U_0$ over a length scale of 0.2δ, as the flow moves upward and around the edge.

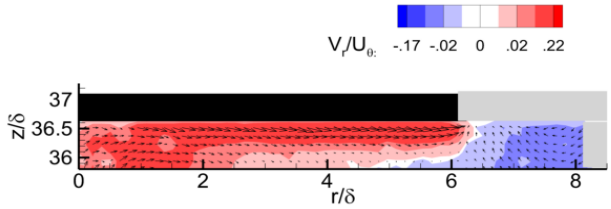

Figure 5.17. Mapping of the upper corner in continuous flow. Contours of the normalized radial at W_g= 0.06 m/s for upper plate f_s =12 mm , Re_θ=1110; case C9-1-4-6.

The flow in the region above the impeller with an imposed axial flow shows similar behavior independent of the length of upper plate. The length scale of the vortex with counter clockwise rotation is about 3δ in the radial direction. The vortex appears to span from 0.5δ atop the impeller up to the corner of the apparatus near the upper plate, see Figure 5.14. Beyond the region bounded by the vortex, at the lowest axial flow rate (W_g=0.014 m/s) for both plate thicknesses, the flow appears to move slowly towards the impeller; yet it shows a small upward flow at 3δ and 6δ for the upper plate of 6 mm and 12 mm respectively; at a height of 30.5δ. These radial locations are at a similar distance from the stationary wall as the upper plate edges.

In the continuous flow cases, a net upward flow above the impeller is shown by the axial contour. However, in the batch condition, it was shown by LDV and PIV measurements that no net upward flow is observed to occur through the transversal holes at similar conditions. It was mentioned in earlier sections that the cross sectional area of the gap δ is 25% smaller than the transversal hole diameter. Although no net upward flow was measured in the batch case, the results obtained for the upper section suggests that while operating with an imposed axial flow, a preferential path through the transversal holes is found.

To this point, it is not known whether the spinning film is affected by the conditions and flow that occur above the upper plate. With the imposed axial flow, the fluid leaves the SFA through the overflow port in the upper chamber. As seen in Chapter 2, the outflow port is the single exit of the SFA and is placed off axis. The overflow port thus causes non-axisymmetric flow above the upper plate. The asymmetry could be transferred from the upper chamber towards the spinning film. The pictorial representation in Figure 5.18

shows the various angles used for mapping the effect of the overflow port on the region above the inner cylinder.

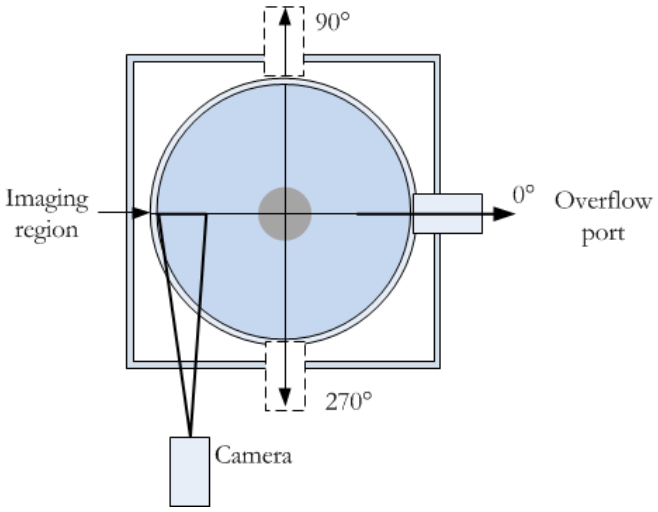

Figure 5.18. Reference cartoon used to show the various position of the overflow port used for mapping of the effect on the upper corner of the SFA.

For the mapping of the effect of overflow port location on the upper section shown in Figure 5.18, the imaging plane is held stationary while the port was rotated to each of four locations. The data shown to this point in the contour plots were axial flow is present, was acquired with the overflow port located at 0° as described in Chapter 2. Now, in Figure 5.19 the contours of the normalized axial velocity show the planes 180° from the location of the overflow port.

From these plots, we observe that the vortex present at upper corner of the apparatus maintains a similar length scale. However, in the region between the upper plate edge and the free boundary, the measured axial velocity at the top of the flow varies depending onthe angular location of the overflow port. In this region, the highest measured axial velocities correspond to the measurements when the overflow port is located at 180° and 270°, as observed in Figure 5.20. Thus, the volumetric flow into the upper section appears to vary with azimuthal location. The axial velocity near the free boundary has a downward direction, which is observed to increase in magnitude proportional to the radial position of the interface. The flow moves downward faster near the interface as the

distance from the inner cylinder tip (rotating) increases, also increasing the thickness of film.

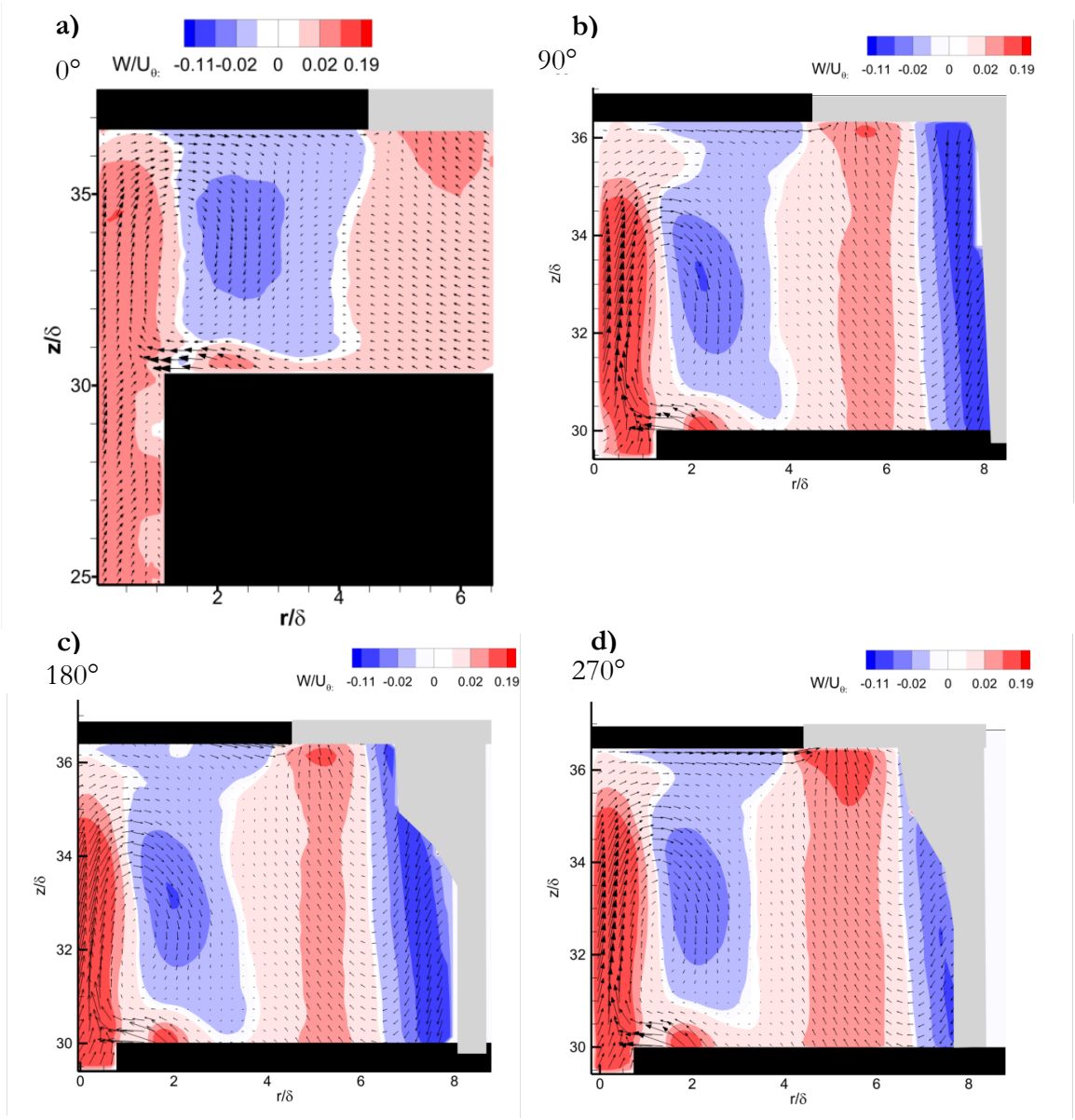

Figure 5.19. Contour plots of the normalized axial velocity in the region above the impeller, W_g= 0.06 m/s, Re_0=1110 and f_s= 9 mm. The angles of the overflow port are in reference to Figure 5.18. a) overflow port located at 0°. b) axial contours for overflow port at 90°. c) overflow port at 180°. d) overflow port at 270°

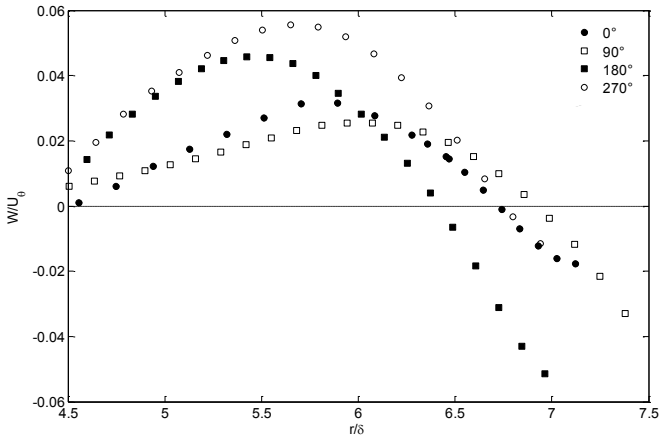

Figure 5.20. Extracted at z/δ= 36.5 normalized axial velocity data from Figure 5.19, at W_g= 0.06 m/s, f_s =9 mm and Re_0=1110. The plotted data starts at the edge of the upper plate and extends to a region near the air/liquid interface. (●) corresponds to the overflow port at 0°. (□)overflow port at 90°. (■)overflow port at 180°. (○)overflow port at 270°.

Chapter 6.

Summary and conclusions

The main objective of this thesis was to unveil the underlying dynamics that occur within the Spinning Film Apparatus at various dynamical conditions. The apparatus was divided in three sections, which are the gap region, lower corner and the upper corner. The mapping of the various flow features were performed at various flow conditions using three flow measurement techniques.

6.1. Mapping of the gap region

Through point measurements in the gap, the velocity profiles of the azimuthal velocity were found to resemble measurements performed in literature for apparatuses with the aspect ratio near to the SFA. The measurements in the gap were taken away from the inner cylinder edges (near the axial center of the apparatus). The azimuthal velocity profile within 0.2δ-0.65δ in the gap showed to have an average magnitude of $0.5U_0$ at Re_0=1110 and 2230. The profile was found to be nominally flat, with a small undulation (twice the experimental uncertainty), which suggests that at both experimental conditions the flow was near the turbulent regime as suggested in literature (Andereck, 1986; Wereley & Lueptow, 1994). However, the presence of vortical structures with Taylor vortex signatures were observed using flow visualization and confirmed by computing the (r,z) vorticity in the gap, obtained using planar PIV. In the condition where W_g=0, at $0.42V_T$ and $0.54V_T$, the average vortex wavelength λ was found to be $3.7\delta \pm 0.06\delta$.

In the gap, the averaged measured axial velocity was found to be constant between radial positions of0.15δ and 0.7δ. The magnitude of the measured axial velocity at $z=6.5h_L$ was negligible for both Re_0=1110 and 2230. This finding indicates that the net amount of fluid passing through the gap while in batch condition is close to zero and that under

batch condition, the nominal flow in the gap is independent of the holding volume in the apparatus.

It was found that with an imposed axial flow of W_g=0.06 m/s, using the upper plate f_s=9 mm, the wavelength of the vortices is essentially unchanged between Re_0=1110-6360, as measured through flow visualization. Using this technique it was noted that at the edges of the inner cylinder regions of unstructured flow were observed. These regions were noted by the work of Burkhalter, 73. While using this visualization technique, when W_g=0 m/s, these regions in the SFA have similar length scales as the ones found by Burkhalter, 73. However, planar PIV on the (r,z) plane showed the presence of what appear to be vortices extending to both edges of the inner cylinder. Moreover, the vorticity contours indicate that the edge vortices had a clockwise rotation (negative vorticity) at both limits of the inner cylinder. For the phase characterized the PIV results suggest that through flow visualization using Kalliroscope particles information is lost. More specifically, the Kallirsoscope particles can be focused into and highlight straining regions between vortices, but probably they cannot mark ends of vortices or weaker vortices.

One of the main objectives of this work was to find the effect of the transversal holes on the flow patterns in the SFA. In batch condition ($0.42V_T$) operating at Re_0= 1110 and 2230, the LDV measurements in the gap showed an axial velocity with a magnitude near $\sim 0U_0$. This finding suggests that in steady state for these Reynolds numbers, there is no flow passing throughout the transversal holes. These findings were validated by measurements in which the transversal holes were covered.

6.2. Lower corner

In the lower corner, a spinning film is formed with an air liquid interface. For the condition with no through flow, the interface is observed to depend both on the rotation rate of the inner cylinder, and the initial holding volume of the liquid in the vessel. It was found that at Reynolds numbers under 2037 for holding volumes of $0.42V_T$ and $0.3\ V_T$, the interface resides behind the inner cylinder. As the Reynolds number is increased, the

interface becomes visible, as the lowest point of the interface moves downward closer to the bottom surface.

It was found that after the free boundary intersects the lower surface of the apparatus at a given Reynolds number and holding volume, the radial location of the intersection point is not affected by increasing the Reynolds number. Therefore, the free boundary achieves a constant thickness after this value. For the aforementioned holding volumes, the interface location at the bottom surface is constant after $Re_0 = 2546$. Similarly, with an imposed axial flow, the interface location requires a minimum Reynolds value to intersect with the lower surface. However, it was found that when through flow is present, for a given Reynolds number compared to the batch condition, the radial location where the bottom surface of the apparatus is in contact with the interface is displaced inward radially. This implies that the formation of the free boundary is delayed when the through flow is imposed.

In the corner region where the bottom surface intersects the stationary cylinder wall ($z = 0\delta$ -2.5δ), which is underneath the impeller, velocity measurements indicate the presence of a stationary vortex. It was found that between the wall and 0.5δ radially, the flow has a net downward direction, which causes the vortex to rotate counter-clockwise, as shown by the vorticity contours. Near the bottom surface at a height of 0.2δ, the flow was observed to move at $0.12U_0$ towards the center of the apparatus for a distance of 3.5δ from the stationary wall. It was observed that the inward moving flow creates a shear layer, which decays in thickness as the flow loses momentum towards the center of the apparatus.

6.3. Upper corner

In the upper section, another stationary vortex was found with similar characteristics as in the lower section. It was found that the rotation of the vortex is clockwise (negative vorticity), both with or without axial flow and for multiple values of upper plate thickness

f_s of 3δ, 4.5δ and 6δ. The width of the vortex in the upper section was ~3δ under all of these conditions.

Under conditions with $W_g>0$, near the upper corner, where the stationary wall meets the upper plate (f_s), the inward radial velocity of the flow increases achieving $0.2U_0$. In the region near the upper plate, the flow is observed to be dragged towards the edge of the plate, where it then passes the corner of the plate and the fluid moves upward leaving the upper corner region. Moreover, with imposed axial flow, the data shows that the location of the free boundary moves inward as the axial flow is increased. It was found that for the throughflow conditions of W_g= 0.01 m/s and 0.06 m/s for a given upper plate, the free boundary moved on average 1δ towards the axial center of the apparatus.

In the batch condition, it was found that the transversal holes have no effect on the velocity statistics in the gap, and at the lower corner of the apparatus. However, with axial flow present in the upper corner of the apparatus, an upward moving flow appears inside of the impeller. The data indicate that this flow region is located normal to the edge of the upper plate, 3δ, 4.5δ and 6δ and could represent flow crossing through the transversal holes without passing through the gap region.

With axial flow imposed, the fluid leaves the SFA through the overflow port, which is located off-axis. From single plane PIV, it was found that the overflow port does cause an asymmetry in the upper section of the apparatus. The free boundary thickness and the uppermost axial velocity profile varied with the position of the overflow port. With f_s=9 mm and W_g= 0.06 m/s, the axial velocity profiles between the upper plate and the free boundary were found to be different throughout the various overflow port angles. However, the true effect of the overflow port on both the free boundary and the gap needs further review.

6.4. Future work

It was shown that the SFA operates nominally as a Taylor vortex apparatus, and that specific structures originate as a consequence of the free boundary underneath and above the inner cylinder. Through these findings, we have brought the first characterization of the flow patterns in this device, which operates as a high speed milling machine.

Similar experiments to the ones performed in this manuscript are recommended with a scaled-up version of the SFA. In those tests, a scaled radius ratio should be used as means of understanding the scaling within the gap region.

Further work on this apparatus should focus on characterizing the gap with higher particle concentration at similar operating conditions as in this manuscript. Moreover, new tests should aim to perform measurements in the turbulent Taylor vortex regime at both low and high particle loading. The latter should aim to record and understand the events of particle breakup, which is the reason for the use of this machine in industrial work. Moreover, we recommend experiments not necessary performed in the SFA, aiming to test the various hypotheses that cause particles to accumulate in specific regions within the SFA, causing them to break.

Bibliography

Adrian, R., & Westerweel, J. (2011). In Shyy W., Rycroft M. (Eds.), *Particle image velocimetry* (1st ed.). New York: Cambridge University Press. doi:978-0-521-44008-0

Akonour, A., & Lueptow, R. M. (2003). Three-dimensional velocity field for wavy Taylor–Couette flow. *Physics of Fluids, 15*, 947. doi:10.1063/1.1556615

Andereck, C. D. (1986). Flow regimes in a circular couette system with independently rotating cylinders. *Journal of Fluid Mechanics, 164*(3), 155. doi:10.1017/S0022112086002513

Babcock, K. L., Guenter, A., & Cannell, D. L. (1991). Noise-sustained structure in taylor-couette flow with through flow. *Physical Review Letters, 67*(24), 3388-3391. doi:10.1103/PhysRevLett.67.3388

Barcilon, A., & Brindley, J. (1984). Organized structures in turbulent taylor-couette flow. *Journal of Fluid Mechanics, 143*(-1), 429. doi:10.1017/S0022112084001427

Barcilon, A., Brindley, J., Lessen, M., & Mobbs, F. R. (1979). Marginal instability in taylor-couette flows at a very high taylor number. *Journal of Fluid Mechanics, 94*(3), 453. doi:10.1017/S0022112079001129

Batchelor, G. K. (1967). *An introduction to fluid dynamics* (I ed.). Great Britain, Cambridge: Cambridge University Press. doi:052104118X, 0521098173

Becker, M. B.,J Schwedes. (1999). Comminution of ceramics in stirred media mills and wear of grinding beads. *Powder Technology, 105*(1), 374-381. doi:10.1016/S0032-5910(99)00161-8

Blecher, L., Kwade, A., & Schwedes, J. (1996). *Powder Technology, 86*(69)

Bunge, F., Pietzsch, M., Müller, R., & Syldatk, C. (1992). Mechanical disruption of arthrobacter sp. DSM 3747 in stirred ball mills for the release of hydantoin-cleaving enzymes. *Chemical Engineering Science, 47*(1), 225-232. doi:10.1016/0009-2509(92)80216-Y

Burin, M. J., Ji, H., Schartman, E., Cutler, R., Heitzenroeder, P., Liu, W., . . . Raftopolous, S. (2006). Reduction of ekman circulation within taylor-couette flow. *Experiments in Fluids, 40*(6), 962-966. doi:10.1007/s00348-006-0132-y

Burin, M. J., Schartman, E., & Ji, H. (2010). Local measurements of turbulent angular momentum transport in circular couette flow. *Experiments in Fluids, 48*, 763-769. doi:10.1007/s00348-009-0756-9

Burkhalter, J. E. (1973). Steady supercritical taylor vortex flow. *Journal of Fluid Mechanics, 58*(part 3), 547. doi:10.1017/S0022112073002326

Calvert, J. G. C. (1990). Glossary of atmospheric chemistry terms (recommendations 1990). *Pure and Applied Chemistry, 62*(11), 2167-2219. doi:10.1351/pac199062112167

Chandrasekhar, S. C.,J Gillis. (1962). Hydrodynamic and hydromagnetic stability. *Physics Today, 15*(3), 58. doi:10.1063/1.3058072

Cleary, P. W. (1998). Predicting charge motion, ower draw, segregation and wear in ball mills using discrete element methods. *Minerals Engineering, 11*(11), 1061-1080. doi:0892-6875(98)00093-4

Clermont, B., De Hass, B., & Hancotte, O. (2008). Real time mill management tools stabilizing your milling process. *The Southern African Institute of Mining and Metallurgy,*

Coles, D. (1965). Transition in circular couette flow. *Journal of Applied Physics, 21*, 385-425.

Couette, M. (1890). Etudes sur le frottement des liquides. *Ann. Chim. Phys., 21*, 433.

Di Prima, R., & Swinney, H. L. (Eds.). (1985). *Instabilities and transition in flow between concentric rotating cylinders* Springer Berlin Heidelberg. doi:10.1007/3-540-13319-4_16

Dong, S. (2007). Direct numerical simulation of turbulent taylor-couette flow. *Journal of Fluid Mechanics, 587*, 373-393. doi:doi:10.1017/S0022112007007367

Donnelly, R. J., & Schwarz, K. W. (1965). Experiments on the stability of viscous flow between rotating cylinders. VI. finite-amplitude experiments. *Proceedings - Royal Society.Mathematical, Physical and Engineering Sciences, 283*(1395), 531-556. doi:10.1098/rspa.1965.0044

Gauthier, G., Gondret, P., & Rabaud, R. (1998). Motions of anisotropic particles: Application to visualization of three-dimensional flows. *Physics of Fluids, 10*(9), 2147. doi:10.1063/1.869736

Hook, M., & Kjell, A. (2009). Historical trends in american coal production and a possible future outlook. *International Journal of Coal Geology, 78*(3), 201-216. doi:10.1016/j.coal.2009.03.002

Jankovic, A. (2001). MEDIA STRESS INTENSITY ANALYSIS FOR VERTICAL STIRRED MILLS. *Materials Engineering, 14*(10), 1177-1186. doi:0892-6875(01)00135-2

Kievsky, Y. Y., Carey, B., Naik, S., Mangan, N., ben Avraham, D., & Sokolov, I. (2008). Dynamics of molecular diffusion of rhodamine 6G in silica nanochannels. *The Journal of Chemical Physics, 128*(15), 151102. doi:10.1063/1.2908875

King, G., Lee, Y. L., Swinney, H., & Marcus, P. (1984). Wave speeds in wavy taylor-vortex flow. *Journal of Fluid Mechanics, 141*(-1), 365. doi:10.1017/S0022112084000896

Koga, J. K., & E L Koschmieder. (1989). Taylor vortices in short fluid columns. *Physics of Fluids.A, Fluid Dynamics, 1*(9), 1475. doi:10.1063/1.857325

Koschmieder, E. (1979). Turbulent taylor vortex flow. *Journal of Fluid Mechanics, 93*(03), 515. doi:10.1017/S0022112079002639

Kubin, R. F., & Fletcher, A. N. (1982). Fluorescence quantum yields of some rhodamine dyes. *Journal of Luminescence, 27*(4), 455-462. doi:10.1016/0022-2313(82)90045-X

Kwade, A. K.,Joerg Schwedes. (2002). Breaking characteristics of different materials and their effect on stress intensity and stress number in stirred media mills. *Powder Technology, 122*(2), 109-121. doi:10.1016/S0032-5910(01)00406-5

Kwade, A. K. (1999). Wet comminution in stirred media mills — research and its practical application. *Powder Technology, 105*(1), 14-20. doi:10.1016/S0032-5910(99)00113-8

Levy, A. D., & Reisfeld, R. (1984). The nature of the silica cage as reflected by spectral changes and enhanced photostability of trapped rhodamine 6G. *Journal of Physical Chemistry, 88*(24), 5956-5959. doi:10.1021/j150668a042

Magde, D., Wong, R., & Seybold, P. (2002). Fluorescence quantum yields and their relation to lifetimes of rhodamine 6G and fluorescein in nine solvents: Improved absolute standards for quantum yields¶. *Photochemistry and Photobiology, 75*(4), 327-334. doi:10.1562/0031-8655(2002)0750327FQYATR2.0.CO2

Mallock, A. (1888). Determination of the viscosity of water. *Proceedings of the Royal Society of London, 45*(273-279), 126-132. doi:10.1098/rspl.1888.0081

Mallock, A. (1896). Experiments on fluid viscosity. *Philosophical Transactions - Royal Society.Biological Sciences, 187*, 41.

Matisse, P., & Gorman, M. (1984). Neutrally buoyant anisotropic particles for flow visualization. *The Physics of Fluids, 27*(4), 759. doi:10.1063/1.864702

Mende, S., F, S., W, P., & J, S. (2004). Production of sub-micron particles by wet comminution in stirred media mills. *Journal of Materials Science, 39*(16-17), 5223-5226. doi:10.1023/B:JMSC.0000039214.12131.58

Min, K., & Lueptow, R. M. (1994). Circular couette flow with pressure-driven axial flow and a porous inner cylinder. *Experiments in Fluids, 17*(3), 190. doi:10.1007/BF00190916

Ohmura, N. (1997). Effective mass diffusion over cell boundaries in a taylor-couette flow system. *Chemical Engineering Science, 52*(11), 1757-1765.

Pai, S. I. (1943). *Technical note* (892nd ed.) N.A.C.A.

Pedocchi, F., Martin, J. E., & García, M. (2008). Inexpensive fluorescent particles for large-scale experiments using particle image velocimetry. *Experiments in Fluids, 45*(1), 183-186. doi:10.1007/s00348-008-0516-2

Prigent, A., & Dauchot, O. (2000). Visualization of a Taylor–Couette flow avoiding parasitic reflections. *Physics of Fluids, 12*(10), 2688. doi:10.1063/1.1287654

Raffel, M., Willert, C., Wereley, S. T., & Kompenhans, J. (2007). *Particle image velocimetry- A practical guide* (Second Edition ed.). New York: Springer=Verlag Berlin Heidelberg. doi:978-3-540-72307-3

Savas, Ö. (1985). On flow visualization using reflective flakes. *Journal of Fluid Mechanics, 152*(-1), 235. doi:10.1017/S0022112085000672

Schlichting, H., & Gersten, K. (2000). *Grenzschicht-theorie* (8th rev. and enl. ed. ed.). New York: Springer. doi:ISBN3540662707

She, Z. S. (2001). Scalings and structures in turbulent couette-taylor flow. *Physical Review.E, Statistical Physics, Plasmas, Fluids, and Related Interdisciplinary Topics, 64*(1), 016308. doi:10.1103/PhysRevE.64.016308

Someya, S., Kuwabara, J., Yan Rong, L., & Okamoto, K. (2010). Experimental investigation of a flow-induced oscillating cylinder with two degrees-of-freedom. *Nuclear Engineering and Design, 240*(12), 4001-4007. doi:10.1016/j.nucengdes.2010.03.033

Takeshi, A. (1996). In Tokushu Kika Kogyo Kabushiki Kaisha (Ed.), *METHOD OF, AND APPARATUS FOR, AGITATING TREATMENT LIQUID* (366/149; 366/279 ed.). United States Patent: B01F 15/06; B01F 9/10. doi:5,582,484

Taylor, G. I. T. (1935). Distribution of velocity and temperature between concentric rotating cylinders. *Proceedings - Royal Society.Mathematical, Physical and Engineering Sciences, 151*(874), 494-512. doi:10.1098/rspa.1935.0163

Taylor, G. I. (1923). Stability of a viscous liquid contained between two rotating cylinders. *Philosophical Transactions - Royal Society.Biological Sciences, 223*, 289.

Tokgoz, S., Elsinga, G. E., Delfos, R., & Westerweel, J. (2012). Spatial resolution and dissipation rate estimation in taylor--couette flow for tomographic PIV. *Experiments in Fluids,* doi:10.1007/s00348-012-1311-7

Vargo, J. V. (1982). In Koppers Company I. (Ed.), *Hammer mill rotor* (241/ 192; 241/195 ed.). United States: B02C 13/02. doi:4,315,605

Weit, H. W.,Jörg Schwedes. (1987). Scale-up of power consumption in agitated ball mills. *Chemical Engineering & Technology, 10*(1), 398-404. doi:10.1002/ceat.270100149

Wereley, S. T. (1992). *A laser doppler velocimetry investigation of the taylor vortex problem.* (Unpublished Masters Dissertation). Dept. Mechanical Engineering. Northwestern University, Evanston, IL 60208.

Wereley, S. T., & Lueptow, R. M. (1994). Azimuthal velocity in supercritical circular couette flow. *Experiments in Fluids, 18*

Wereley, S. T., & Lueptow, R., M. (1998). Spatio-temporal character of non-wavy and wavy Taylor–Couette flow. *Journal of Fluid Mechanics, 364*(-1), 59-80.

Wereley, S. T., & Lueptow, R. M. (1999). Velocity field for taylor-couette flow with an axial flow. *Physics of Fluids, 11*(12), 3637-3649. doi:10.1063/1.870228

White, J., & Muller, S. (2002). Experimental studies on the stability of newtonian Taylor–Couette flow in the presence of viscous heating. *Journal of Fluid Mechanics, 462*, 133. doi:10.1017/S0022112002008443

Appendix A.

LDV - Calculation of the optical error on the azimuthal component caused by curved interfaces

The light beams originating at the LDV probe used to measure the axial component pass through the radial center of the curved interfaces, thus reducing errors caused by the curvature. However, the light beams used to measure the azimuthal component are prone to optical errors as a result of the curved interfaces as shown in Figure A.1.

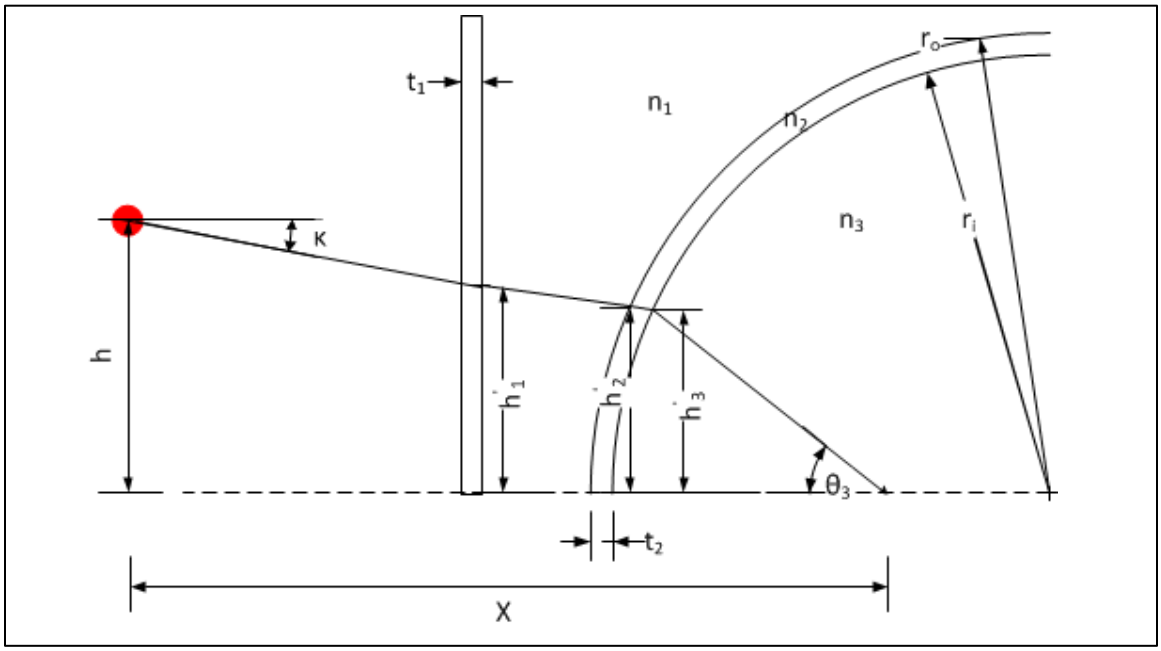

Figure A.1. Ray optics diagram for the light beam used to measure the azimuthal velocity component by LDV. The red circle is used as reference for the location of a light beam.

In Figure A.1 the angle shown for the ray with angle θ_3 leaving surface with radius r_i is exaggerated to ease understanding. The variables h_1', h_2' and h_3' correspond to the relative height of the beam leaving an interface (surface); and n_1, n_2, n_3 are the various index of refraction for the surfaces or fluid. The variable t_1 represents the thickness of the glass box and t_2 the thickness of the outer cylinder in the SFA. Finally, the distance X

references the length between the origin at the probe lens and the final position of the measuring volume. Table A.1 shows dimensions for the aforementioned variables.

Table A.1. Reference values for variables shown in Figure A.1

Variable	Description	Units
f_L	Lens focal length in air	135 mm
h	Beam separation = ½ D_b	25mm
n_a	Refractive index of air	1
$n_1 = n_3$	Refractive index of water	1.333
n_2	Refractive index of glass	1.46
t_1	Thickness of flat interface	3 mm
t_2	Thickness of curved interface	2 mm
$\boldsymbol{\kappa}$	Beam half angle = $\frac{\theta}{2}$ in air	10.75°

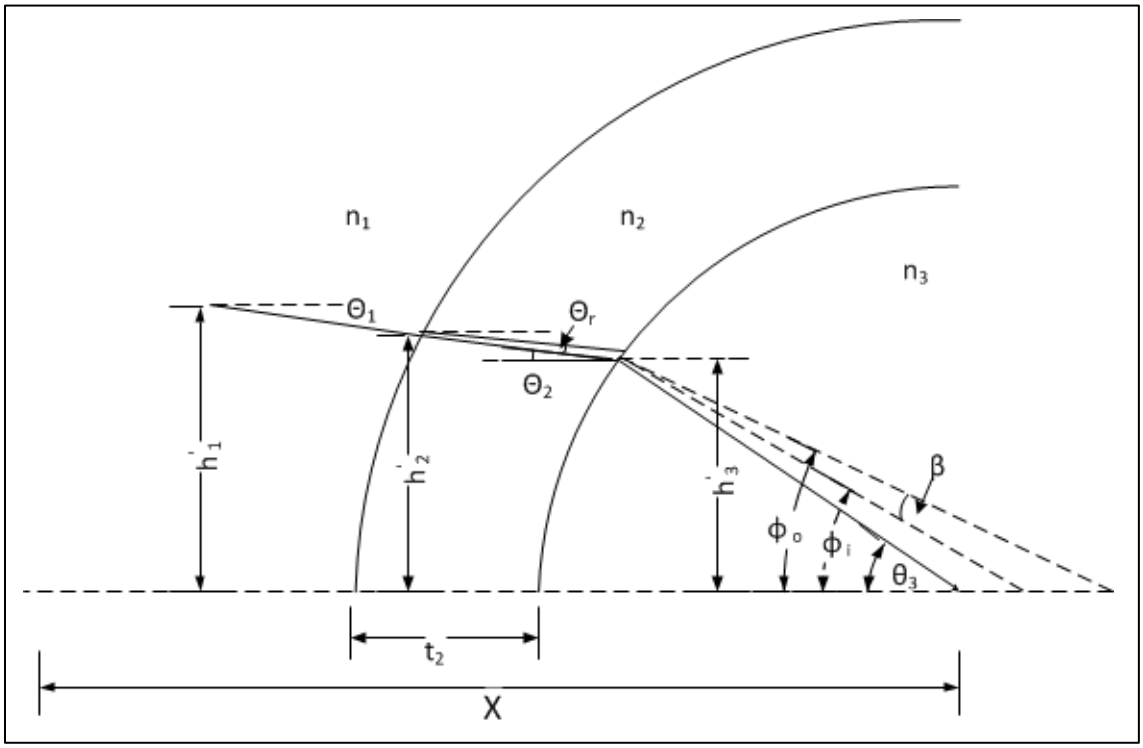

Figure A.2. Diagram of the ray optics for the exploded view of Figure A.1Table A.1.

Figure A.2 shows an expanded view of the diagram shown in Figure A.1. It shows the refracted angles by which the light beam is subjected to. The angle θ_1 refers to the angle

leaving the flat surface with thickness n_1, angles θ_2 and θ_3 correspond to the refracted angle at the curved surfaces. Moreover, the variables θ_r, θ_i and θ_o refer to angles displaced by the radius of curvature of the curved surface, which causes the fringes on the measurement volume to have a different spacing from the calculations performed in air. The change in size of the measurement volume generates an error on the measurement of the azimuthal velocity. Detailed quantification of this error is show next:

$$\theta_1 = \theta_i + \phi_o$$
$$\theta_2 = \theta_r + \phi_i$$

Applying Snell's law and knowing that $n_1 > n_2$,

$$n_1 \sin(\theta_1 - \phi_0) = n_2 \sin(\theta_2 - \phi_o)$$
$$\theta_2 - \phi_o = \frac{n_1}{n_2}\theta_1 - \frac{n_1}{n_2}\theta_2$$
$$\therefore \theta_2 = \frac{n_1}{n_2}\theta_1 + \left(1 - \frac{n_1}{n_2}\right)\phi_o$$

In a similar way we know that $n_1=n_3$

$$\theta_3 = \frac{n_2}{n_2}\left(\frac{n_2}{n_1} - 1\right)(\phi_o - \phi_1)$$

The definition, $\beta = \phi_o - \phi_i$ can be simplified by applying a small-angle approximation.

$$\frac{\sin\beta}{B} = \frac{\sin\theta_r}{r_i}$$

Where the length B is defined as follows: $B = \frac{t_2}{\cos\theta_r}$, then β becomes: $\beta \approx \frac{t_2}{r_i}\tan\theta_r$

Quantification of the error of displacement is obtained by the ratio of the incident angle θ_1 and displaced angle θ_r.

$$\frac{\theta_2}{\theta_1} = 1 + \left(\frac{n_2}{n_1} - 1\right)\frac{\beta}{\theta_1}$$

The error is then characterized by: $\left(\frac{n_2}{n_1} - 1\right)\frac{t_2}{r_i}\frac{\theta_r}{\theta_1}$,

The value for the error caused by the curved interfaces is therefore:

$$RE = 0.0063\frac{\theta_r}{\theta_1};$$

This implies that $\theta_r < \theta_1$, with an error value of 0.6% from the incident beam originated after the flat surface.

Appendix B.

LDV Calibration plate

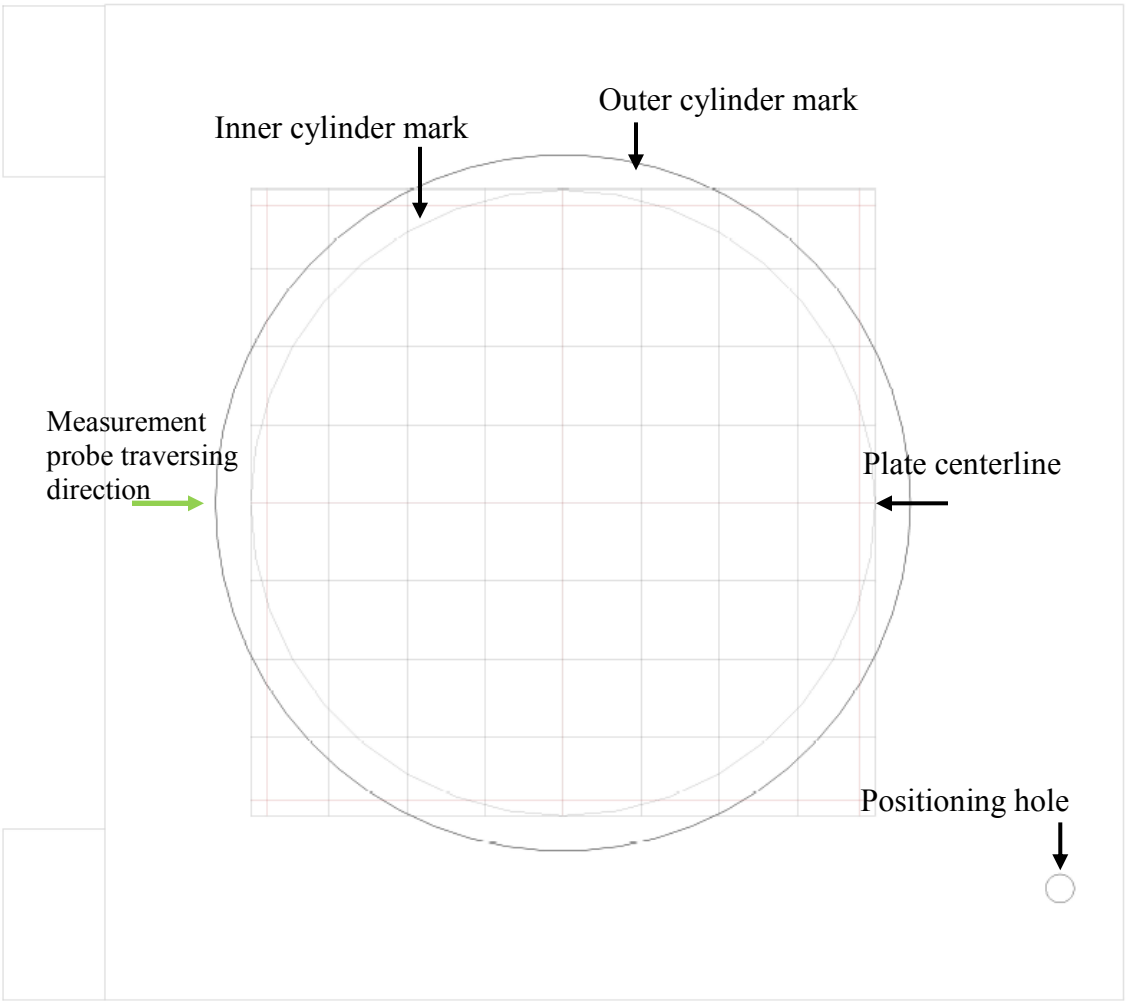

Figure B.1. Diagram of the calibration plate used to align the azimuthal measurement volume of the LDV system

The inner and outer cylinder marks are used as references to know the position of the measurement volume. Through the positioning hole the calibration plate is inserted into one of the iron beams that are used to anchor the SFA glass box to the steel frame.

Appendix C.

Mie Scattering of tracer particles

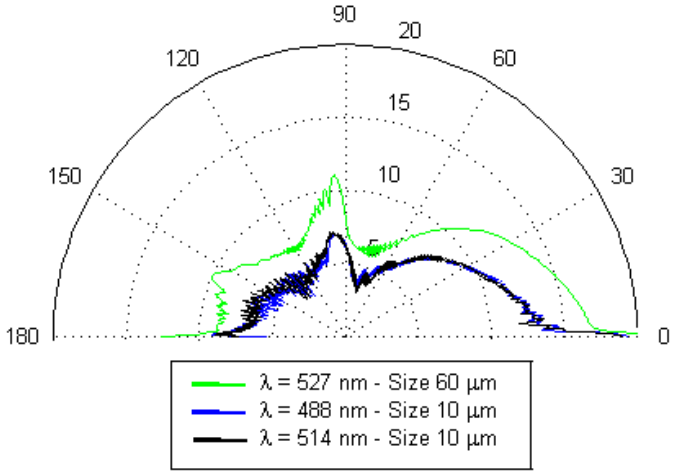

Figure C.1. Shows the calculated polar diagram for the normalized scattering of polarized light. The direction of incident light (θ=180°); using flow tracking particles. The continuum media is water with a refractive index of about n =1.34 at 20°C and the particles consist of Polyamide resin. Calculations were performed using software solving the Bohren and Huffmann algorithm for scattering of a small sphere by Philip, 2014.

Figure C.1shows the polar diagram for the light intensity of the scattered light of the tracer particles. The particles shown are made of Polyamide with a refractive index of 1.34. The various light sources correspond to the beam wavelengths used to illuminate the particles.

Appendix D.

Example temporal-Spatial images in the axial plane for flow visualization.

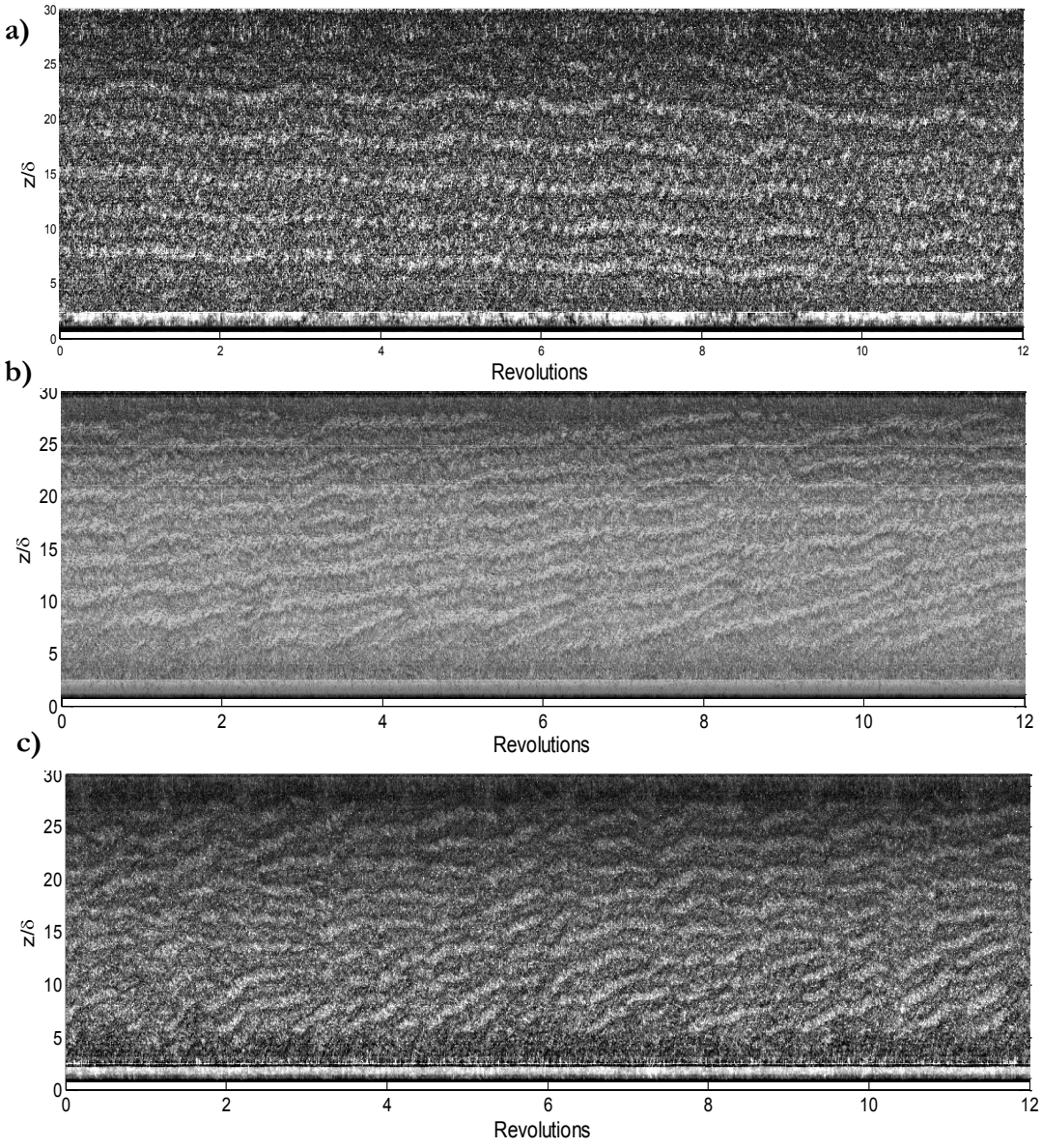

Figure D.1. Spatial, temporal transformations for Re_θ=1110 at various conditions. a) Experiment B9-1-2, 0.42V_T, W_g=0 m/s. b) Experiment B12-1-2, holding volume 0.42V_T, W_g=0 m/s. c) C9-1-2-6, Upper plate ℓ_s=9 mm, W_g=0.06 m/s.